Modeling and Analysis of Interactions in Grid-Forming Inverter Systems

Theja T. Muthukumarana Hewa Thondilege

A Thesis submitted to the Faculty of Graduate Studies of

The University of Manitoba

in partial fulfillment of the requirements of the degree of

Doctor of Philosophy

Electrical and Computer Engineering Department

University of Manitoba

Manitoba, Canada

Feb. 2025

Abstract

The grid-forming (GFM) concept is an inverter control method that deploys the inverter's power modulations to regulate the system voltage and frequency. A variety of GFM controller topologies can be found in the literature. Mainly a GFM controller consists of a layer that mimics synchronous machine characteristics and a current-limiting loop. Depending on the controller topology and parameters, a GFM inverter's dynamics can spread over a wide bandwidth leading to a wide range of interactions. The full disclosure of the root causes of interactions that can be excited by a GFM inverter is still lacking in the literature. Therefore, in this research small-signal, model-based eigenvalue analysis is conducted on commonly-used GFM controller topologies with different ac- and dc-side system configurations to reveal the full causes of interactions that can happen in a GFM inverter system. The virtual electromechanical interaction between GFM inverters and other GFM inverters and synchronous machines, high-frequency network interactions, and interactions between the dc-side circuitry and GFM controller, LC filter components, and the governor-turbine of synchronous machines are revealed and verified by PSCAD/EMTDC simulations. This comprehensive analysis unfolds the main driving factors behind the critical interactions in GFM inverter systems and proposes effective mitigation methods.

Copyright Forms

The author would like to acknowledge using the following papers in preparation of this thesis:

Chapter 2 includes the content from "T. Thilekha, S. Filizadeh, U. Annakkage, C. Karawita, and D. Muthumuni, "Analysis of interactions among parallel grid forming inverters," *Electric Power Syst. Res.*, vol. 223, p. 109652, Oct. 2023."

As the author of Elsevier's article, the right to include it in the thesis is permitted. The copyright information of Elsevier is in `https://www.elsevier.com/about/our-business/policies/copyright#Author-rights`.

Chapter 3 includes the content from "T. Thilekha, S. Filizadeh, U. Annakkage, C. Karawita, and D. Muthumuni, "Grid-Forming Inverter Interaction Studies Using Small-Signal Stability Assessment," in *Proc. CIGRE Canada Conf. and Expo.*, (Manitoba, Canada), Oct 2024."

The authors are entitled to reuse all or portions on the paper in other works according to the CIGRE Copyright provision in `https://cigre-usnc.org/wp-content/uploads/2017/03/CIGRE-COPYRIGHT-PROVISIONS.pdf`

Chapter 5 ©2024 IEEE. Reprinted "T. Thilekha, S. Filizadeh, U. Annakkage, C. Karawita, and D. Muthumuni, "Effect of DC-Side Dynamics on Interactions in Grid-Fromin Inverter Systems," *IEEE Trans. Energy Convers.*," to appear.with permission from T. Thilekha, S. Filizadeh, U. Annakkage, C. Karawita, and D. Muthumuni. According to IEEE copyrighted materials, internal and personal usage is permitted. IEEE does not endorse any of the University of Manitoba's products and services.

Acknowledgements

I would like to express my deepest gratitude to all who have supported me throughout my Ph.D. studies journey.

First and foremost, I am profoundly grateful to my advisor, Prof. Shaahin Filizadeh, for his expert guidance, unwavering support, and invaluable encouragement throughout my research. I would like to extend my heartfelt gratitude to my co-advisor, Prof. Udaya Annakkage, for his insightful feedback on my research.

I am grateful to Dr. Chandana Karawita from Transgrid Solutions for guiding me with his expert knowledge and industrial experience from the beginning of my research. I also extend my sincere gratitude to Dr. Dharshana Muthumuni from Manitoba Hydro International (MHI) for the constructive comments and suggestions to enhance the quality of this research.

I would also like to acknowledge the support of my fellow researchers and the technical staff in the Price Faculty of Engineering, University of Manitoba, for making my research experience smooth and productive.

I am deeply grateful to my family for their endless encouragement and understanding. I am grateful for the financial support I received from the University of Manitoba, the Natural Sciences and Engineering Research Council (NSERC), MITACS, and MHI.

With all due respect, I also acknowledge the 17 years of free education I received in Sri Lanka.

Dedication

To my husband and parents.

Contents

List of Figures

List of Tables

Nomenclature

Major Subscripts

CC	matrices corresponding to decoupled current controller
cv	measurements at the converter terminal
d,q	dq components of measurements
DC	matrices corresponding to DC-side of GFM inverter
E	matrices corresponding to AC4A exciter
f	measurements and parameters of the LC filter and the low-pass filtered other measurements
gfm	parameters corresponding to grid-forming inverter
GT	matrices corresponding to governor-turbine model
hp	variables and parameters corresponding to high-pass filtering of current components in transient virtual impedance path
LCL	matrices corresponding to LC filter and transformer block
L	parameters, variables and matrices corresponding to load component
m	matrices corresponding to synchronous machine
N	matrices corresponding to network component
pcc	measurements at the LC filter terminal
pi	measurements and parameters of the shunt impedance of the π section

$_{\mathrm{P}}$ matrices corresponding to power controller

$_{\mathrm{ref}}$ reference signals

$_{\mathrm{sm}}$ parameters, variables and matrices corresponding to the synchronous machine including governor-turbine and exciter

$_{\mathrm{tx}}$ measurements and parameters of the series impedance of the π-section

$_{\mathrm{t}}$ measurements and parameters of the transformer

$_{\mathrm{VC}}$ matrices corresponding to decoupled voltage controller

$_{\mathrm{virt}}$ parameters of virtual impedance used in virtual admittance-based inner current controller

$_{\mathrm{vi}}$ variables and parameters of virtual impedance used in virtual impedance-based current controller

Common Symbols

δ the angle difference between the reference frames

$\omega, \omega_{\mathrm{b}}$ rotational speed, base rotational speed

H, D_{p} inertia time constant, P-f droop co-efficient

R, L, C resistance, inductance, capacitance

Power Controller

D_{q} Q-v droop co-efficient

$K_{\mathrm{p}}, T_{\mathrm{i}}$ proportional gain and integral time constant of PI controller for Q-v controller

$T_{\mathrm{p}}, T_{\mathrm{q}}, T_{\mathrm{v}}$ time constant of low-pass filter for active power, reactive power, and voltage

x_1 state to represent the dynamics of PI controller for Q-v controller

Virtual Impedance-Based Controller

i_{cvpk} converter peak current

$i_{\text{threshold}}$ the current threshold to calculate current dependent virtual impedance

$K_{\text{pRVI}}, K_{\text{pLVI}}$ current dependent virtual resistance, inductance gains

$R_{\text{vi0}}, L_{\text{vi0}}$ virtual resistance, inductance of transient virtual impedance path

Virtual Admittance-Based Inner Current Controller

$K_{\text{pi}}, T_{\text{ii}}$ proportional gain and integral time constant of PI controller for current controller

x_4, x_5 states to represent the dynamics of PI controller for i_{cvd}, i_{cvq} controllers

Cascaded Voltage Current Controller

K_{av} anti-wind-up gain for decoupled voltage controller

$K_{\text{pv}}, T_{\text{iv}}$ proportional gain and integral time constant of PI controller for voltage controller

x_6, x_7 states to represent the dynamics of PI controller for v_{fd}, v_{fq} controllers

Synchronous Machine

ψ flux linkages

K_{D} mechanical friction and windage loss co-efficient

R_{a} stator winding resistance

Governor-Turbine

$T_{\text{G}}, T_{\text{CH}}$ governor and turbine time constants

T_{m} mechanical torque

x_2 a state to represent governor dynamics

Exciter

$K_{\text{A}}, T_{\text{A}}$ exciter gain and low-pass filter time constant

$T_{\text{C}}, T_{\text{B}}$ lead, lag time constants

T_{r} time constant of low-pass filter for the terminal voltage of synchronous machine

x_3 a state to represent exciter dynamics

DC-Side Quantities

$\mathrm{V}_{\mathrm{bat}}, i_{\mathrm{bat}}$ measurements at the dc-source

C_{dc} dc-link capacitance

d duty ratio for the bi-directional dc-dc converter

$K_{\mathrm{pibat}}, T_{\mathrm{iibat}}$ proportional gain and integral time constant of PI controller for dc-source current controller

$K_{\mathrm{pvdc}}, T_{\mathrm{ivdc}}$ proportional gain and integral time constant of PI controller for dc-link voltage controller

L_{bat} smoothing filter inductance

$T_{\mathrm{vdc}}, T_{\mathrm{idc}}, T_{\mathrm{ibat}}$ time constants of low-pass filter for dc-link voltage, dc current injection to GFM inverter, and dc-source current

$v_{\mathrm{dc}}, i_{\mathrm{dc}}$ measurements at the dc-link capacitor

x_8, x_9 state to represent the dynamics of PI controller for dc-link voltage, and dc-source current controllers

Chapter 1

Introduction

1.1 Background

Technological advances in power electronics and control methods have led to the large-scale adoption of grid-tied inverters to connect renewable generation resources and energy storage devices. Replacing conventional synchronous generation units with inverter-based resources deteriorates the inertia and the strength of the grid that would, otherwise, have been provided by synchronous machines.

System inertia is a measure of system's resiliency to frequency changes. Synchronous machines consist of heavy rotating elements that provide inherent resistance to rapid changes in machine's speed following mismatches of power supply and demand. The rotors of synchronous machines gradually release or absorb the energy imbalance as kinetic energy and help to avoid large frequency excursions. The ability to maintain the system stability during and following disturbances is determined by the system strength. The impedance of the grid plays a major role in determining the strength of the gird at an interconnection point [1]. A strong system has a low source-impedance, which indicates that electrically the ability of the system to impede fast changes of bus voltage and frequency.

Conventionally a grid-tied inverter is controlled as a grid-following inverter, which injects

the power generated from the primary energy source while following the grid's voltage [2]. Furthermore, grid-following inverters require a phase-locked-loop (PLL) whose proper operation demands a strong ac network.

With inevitable weak grid conditions in modern power systems, the active participation of grid-tied inverters to assist in, or even take charge of, maintaining the system's frequency and voltage through power modulations without relying on a PLL has attracted much attention, and has led to the concept of grid-forming (GFM) controls. There are many GFM control concepts suggested in the literature [2–4]; they can be broadly categorized as droop-based and other types.

The droop-based controller is the simplest and the most widespread GFM controller topology, which enables parallel operation between the units under droop control, even in the absence of a communication system [2–4]. The active power-frequency (P-f) and reactive power-voltage (Q-v) droop relationships used in the governor and the automatic voltage regulation of conventional synchronous machines, respectively, are viewed under this category. The coupling between these two relationships is minimized in inductance-dominant networks. With significant resistive characteristics seen in low-voltage networks, either a modified droop relationship or virtual inductance as in [5] has to be introduced. In [6] integral and derivative control actions are introduced to conventional droop scheme to improve the transient response.

While P-f droop emulates the primary frequency response of a synchronous machine, to explicitly emulate the inertial characteristics, the swing equation is commonly embedded with the P-f droop relationship. This GFM control topology is identified as the virtual synchronous machine (VSM) [2].

The other GFM control topologies that do not explicitly emulate the synchronous machine's dynamics are of different forms. Virtual Oscillator Control (VOC) in [7] is a nonlinear controller based on the Van der Pol oscillator. The inductance and capacitance of the oscillator are selected to achieve the resonant frequency at the nominal frequency. In [8], a

phase-locked loop (PLL) has been used as a part of the power controller of the GFM scheme. The phase detector of the PLL generates a signal proportional to the active power generated from a voltage source, which is then processed to obtain the current reference for the inner current controlling layer. The matching control concept is based on the duality between the rotational kinetic energy stored in the rotor of a synchronous machine and the electrostatic energy stored in the dc link capacitor and the other energy sources on the dc-side. This method explicitly looks at the physical realization of inertial and damping characteristics through physical quantities of the inverter [9].

A widely-used GFM control topology for grid-tied inverters is the VSM. Thus it is important to do an in-depth study and understand VSM. VSM controls the converter as a voltage source. However, due to the limited over-loading capability of power electronic switches, an explicit current-limiting method is required. An overview of existing current-limiting methods are discussed in Chapter 4 in detail.

Depending on the controller topology and its parameters, GFM inverters' bandwidths may lie over a broad frequency range, which evokes a much wider range of interactions than those in systems comprising conventional synchronous machines.

Poorly selected controller parameters and network conditions may easily lead to sustained or growing oscillations. Frequency-domain models have been developed for single GFM inverters for parameter selection [10]; however, extending their conclusions is impractical for parallel-connected GFM inverters as such systems are prone to interactions. In a few references, active power oscillations have been observed in parallel-connected GFM inverters [11–13]. These oscillations have been reduced by introducing more damping to the system via controller modifications without clear explanations of the root causes of the interactions.

There have been other attempts, e.g., by neglecting the dynamics of current-limiting loops [11–14] and use of constant-admittance network models [11], to simplify stability analysis of GFM inverter systems. These simplifications, however, have detrimental impacts on the discovery of critical interactions that may occur with high-bandwidth controllers [15]

and also overlook high-frequency interactions that can only be captured with proper representation of the network's dynamics [16]. Furthermore, most of the GFM inverter stability assessments have considered an ideal dc-side. However, ac-side dynamics are coupled with dc-side dynamics via the dc-bus voltage controller and dc-link capacitor dynamics. A detailed review of considering dc-side dynamics in the GFM inverter system's stability analysis is given in Chapter 5.

To analyze the stability of inverter-tied systems, impedance-based [17] and eigenvalue-based [13] methods are commonly used. Impedance-based analysis provides design-oriented insight into the effects of the controllers on the converter terminal quantities [18]. However, compared to impedance-based analyses, eigenvalue-based methods have the superior capability to identify the key parameters that significantly participate in oscillatory mode(s) [19], allowing the discovery of the root causes of interactions. An overview of the small-signal stability assessment is given in Appendix A. Furthermore, small-signal modeling and eigenvalue-based analysis have been heavily used in stability assessment [20] and controller design [21] of GFM inverter-based systems, and are used in this study as well.

1.2 Research Objectives

The main objective of the research is to reveal the full causes of interactions that can happen in GFM inverter systems. To achieve this main objective the following tasks are identified.

- Develop EMT models in PSCAD/EMTDC with different GFM controller topologies and test system configurations, considering both ac and dc sides.
- Develop small-signal models of different GFM inverter systems and validate against detailed models in PSCAD/EMTDC. Include full dynamics of the GFM controller, ac and dc network components.
- Conduct eigenvalue analysis on the developed small signal models to identify critical interactions under different GFM controller topologies and test system configurations.

Identify the root causes of those interactions and develop mitigation methods for such interactions.

1.3 Research Contributions

A summary of key contributions are listed below.

- Development and validation of small-signal models that include the full dynamics introduce by the GFM controller, ac network, and dc-side circuitry of the GFM inverter.
- Identification of the wide range of interactions that can be excited by different GFM controllers.
- Revealing the root causes of critical interactions that can be observed in GFM inverter systems.

1.4 Thesis Outline

This thesis consists of six chapters, as described below:

Chapter 1: Includes background information of the research and the research objectives.

Chapter 2: Identifies the interactions that can happen in a parallel-connected GFM inverter system in islanded mode.

Chapter 3: Analyzes the interactions that can happen between a GFM inverter and a synchronous machine.

Chapter 4: Includes an analysis of the effect of current-limiting algorithms in causing interactions in GFM inverter systems and a comparative analysis of the fault-ride-through capability of the selected current-limiting methods.

Chapter 5: Analyzes the effect of GFM inverter's dc-side dynamic on the interactions in GFM inverter systems.

Chapter 6: Presents the conclusions drawn from the studies conducted, contributions made, and suggestions for future research work.

Chapter 2

Modeling and Analysis of Interactions between Parallel-Connected Grid-Forming Inverters

This chapter presents small-signal modeling and eigenvalue-based analysis to identify the root causes of interactions that may happen in a system with multiple grid-forming inverters. For this purpose, an exemplar two-inverter system is considered. This basic test system replicates aggregate models of GFM-controlled inverter systems in islanded operation and provides detailed insight about the key parameters affecting critical oscillatory modes in such systems. Network dynamics are included through dynamic phasor modeling of its elements, and controller dynamics are fully included. The dc-side dynamics are excluded by adopting an ideal dc-side. In Chapter 5, this model is extended by including dc-side dynamics.

Section 2.1 discusses the study system and the adopted GFM controller. The small-signal model development is discussed in section 2.2 followed by eigenvalue analysis in section 2.3. A summary of the chapter and its key contributions are given in section 2.4.

2.1 Test System

In the test system considered, two-level voltage source converters with GFM control loops are connected to a common point-of-interconnection (POI) via LC filters, step-up-transformers, and short transmission lines as shown in Fig. 2.1. The parameters of the test system are given in Table 2.1. Although nominally-identical GFM inverters are considered, sensitivity studies are conducted to identify the effect of non-identical GFM inverter systems on critical oscillatory modes of the systems. The adopted GFM controller topology and its parameters are given in section 2.1.1.

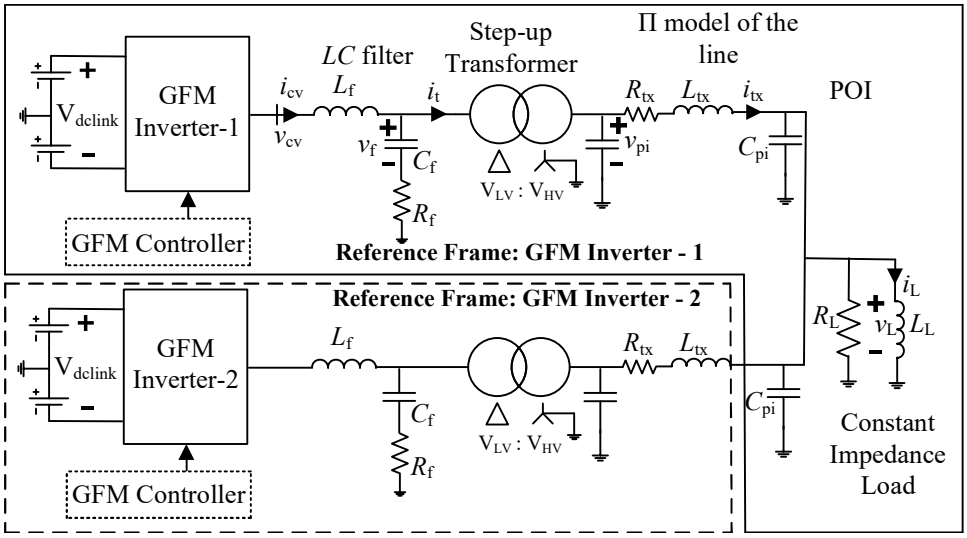

Fig. 2.1: Test system to study interactions between parallel connected GFM inverters.

Table 2.1: Parameters of the Test System Consisting of Paralleled GFM Inverters

Source rating:	**Switching frequency**:	**Load**:	**dc-link:**
25 MVA	4 kHz	$R_{\mathrm{L}} = 55.3\ \Omega$, $L_{\mathrm{L}} = 0.3$ H	$V_{\mathrm{dclink}} = 26$ kV
***LC* filter:** $L_{\mathrm{f}} = 2.0$ mH, $C_{\mathrm{f}} = 34.8\ \mu$F, $R_{\mathrm{f}} = 1.8\ \Omega$			
Transformer: $\mathrm{V_{LV}}$:$\mathrm{V_{HV}}$ = 13.8: 44 kV, $L_{\mathrm{tf}} = 0.1$ pu, $R_{\mathrm{tf}} = 0.01$ pu			
π-section: Line length = 10 km, $L_{\mathrm{tx}} = 10.74$ mH, $R_{\mathrm{tx}} = 1.03\ \Omega$, $C_{\mathrm{pi}} = 5.46\ \mu$F			

2.1.1 Grid-forming controller

The high-level block diagram of the GFM controller is given in Fig. 2.2. The GFM controller consists of an active power-frequency (P-f) controller, a reactive power-voltage (Q-v) controller, and a current controller based upon a virtual impedance (VI). Each of these control blocks is described next.

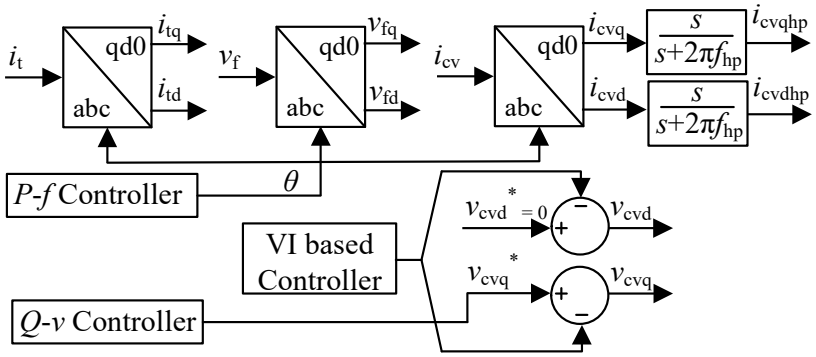

Fig. 2.2: Block diagram representation of the GFM controller.

In the P-f controller (Fig. 2.3(a)), the P-f droop relationship generates a power command that passes through a block that emulates the swing equation of a synchronous machine to obtain the virtual rotational speed of the GFM inverter. The damping coefficient corresponding to mechanical friction and windage losses of a conventional synchronous machine is not included in the GFM controller. The reactive power-voltage regulation is carried out through the Q-v droop relationship as shown in Fig. 2.3(b). The GFM inverter terminal's reference voltage (v^*_{cvq}) is generated by the Q-v controller. The P-f and Q-v controllers emulate a low-order synchronous machine model, and hence the controller scheme is termed a virtual synchronous machine (VSM).

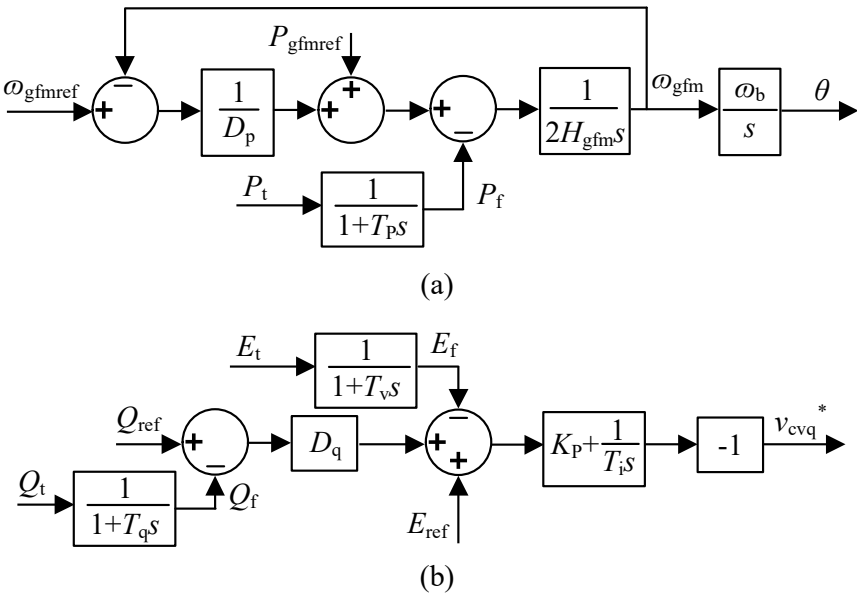

Fig. 2.3: Block diagrams of (a) *P-f* and (b) *Q-v* controllers.

The output commands of the *P-f* and *Q-v* controllers operate the GFM inverter as a voltage source. However, during overloads and faults, an explicit current-limiting method is required to prevent over-current conditions for the converter's sensitive semiconductor devices. Fig. 2.4 shows the VI-based current controller adopted from [22]. The VI-based controller consists of a current-dependent virtual impedance path and a transient virtual impedance path.

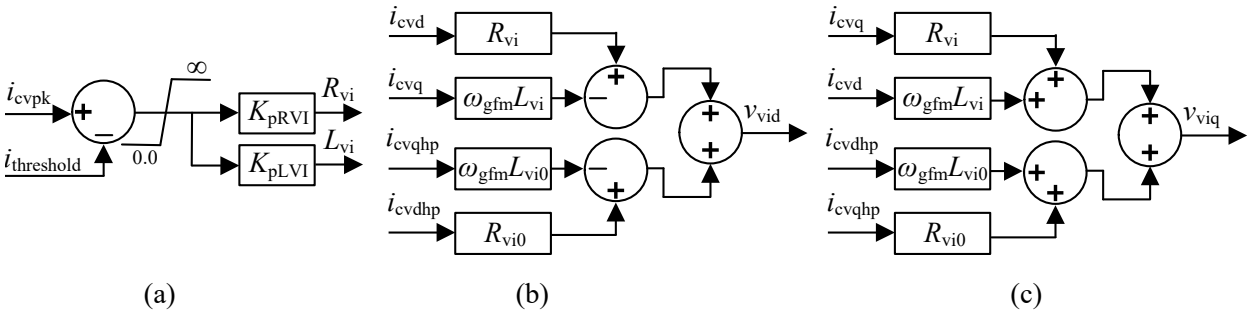

Fig. 2.4: VI-based controller block diagram: (a) current-dependent virtual resistance and inductance calculation, (b) d-axis virtual voltage drop calculation, and (c) q-axis virtual voltage drop calculation.

Fig. 2.4(a) shows the current-dependent virtual impedance calculation. If the con-

verter current's peak value, $i_{\text{cvpk}} = ({i_{\text{cvd}}}^2 + {i_{\text{cvq}}}^2)^{1/2}$, exceeds the specified current threshold, $i_{\text{threshold}}$, the difference between the two is multiplied by the gains K_{pRVI} and K_{pLVI} to obtain the magnitudes of virtual resistance (R_{vi}) and virtual inductance (L_{vi}), respectively. As shown in Figs. 2.4(b) and 2.4(c) the virtual voltage drop between the converter terminal and the filter inductance (L_{f}) is calculated by multiplying R_{vi} and L_{vi} by the corresponding dq components of the converter current. This virtual voltage drop is subtracted from the voltage reference generated from the Q-v controller (Fig. 2.2) to reduce the terminal voltage during over-currents, leading to a lower current injection from the converter. In the transient VI path, the constant virtual resistance value (R_{vi0}) and the constant virtual inductance value (L_{vi0}) are multiplied by the high-frequency components of the converter current's dq components (Figs. 2.4(b) and 2.4(c)). This path also emulates a voltage drop between the converter terminal and the filter inductance. Those high-frequency current components will appear following the transients in the converter current and, therefore, this path acts as an active damping path on the converter currents. The parameters of GFM controller are given in Table 2.2. Development of the test system's small-signal model is discussed in detail in the next section.

Table 2.2: Parameters of the GFM Controller

***P*-*f* controller parameters**
$\omega_{\text{gfmref}} = 1.0$ pu, $P_{\text{gfmref}} = 0.7$ pu, $H_{\text{gfm}} = 2$ s, $D_{\text{pgfm}} = 0.03$ pu, $T_{\text{p}} = 0.01$ s, $\omega_{\text{b}} = 377$ rad/s
***Q*-*v* controller parameters**
$Q_{\text{ref}} = 0.35$ pu, $E_{\text{ref}} = 1.05$ pu, $D_{\text{q}} = 0.03$ pu, $T_{\text{q}} = T_{\text{v}} = 0.01$ s, K_{p}= 0.1, $T_{\text{i}} = 0.25$ s
VI-based current controller parameters
$i_{\text{threshold}} = 1.1$ pu, $K_{\text{pRVI}} = 5$, $K_{\text{pLVI}} = 0.0$, $R_{\text{vi0}} = 0.25$, $L_{\text{vi0}} = 0.0$, $f_{\text{hp}} = 0.5$ Hz

2.2 Small-Signal Model Development

Firstly, the regions to be modeled in each source's reference frame are assigned as depicted in Fig. 2.1. The selection of the reference frame for the passive network components is arbitrary. Regions included in the GFM inverter-1's reference frame are denoted within a

set of solid lines, whereas those in the other GFM inverter's reference frame are denoted within a dashed box.

The boundary state variables (i.e., bus voltages and line currents) that interconnect the two reference frames require transformation from one frame to another. In [16] a common reference frame is used; however, this requires all the individual dynamic devices to have a boundary with a single machine, identified to be the common reference frame generator. This is generalized in this work with the aim of enhancing the flexibility in selecting the regions to be modeled even if the number of reference frames (i.e., regions corresponding to dynamic devices) is more than two. Transformation of variables from reference frame i to reference frame j (rotating with speeds of ω_i and ω_j, respectively) as shown in Fig. 2.5 may be done as follows.

$$[x_{\mathrm{d}j} \quad x_{\mathrm{q}j}]^{\mathrm{T}} = \boldsymbol{T_{ij}}[x_{\mathrm{d}i} \quad x_{\mathrm{q}i}]^{\mathrm{T}} \tag{2.1}$$

The transformation matrix, $\boldsymbol{T_{ij}}$, is given in (2.2).

$$\boldsymbol{T_{ij}} = \begin{bmatrix} \cos(\delta_{ij}) & -\sin(\delta_{ij}) \\ \sin(\delta_{ij}) & \cos(\delta_{ij}) \end{bmatrix} \tag{2.2}$$

where

$$\dot{\delta}_{ij} = \omega_i - \omega_j \tag{2.3}$$

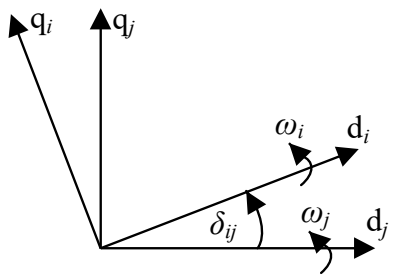

Fig. 2.5: Rotating reference frames.

The component connection method [18] is used to develop the small-signal model. In this method, the power system is decomposed into its sub-components (e.g., grid-forming and grid-following inverters, synchronous machines, filters, π-sections, etc.) and each sub-component is linearized locally to obtain its linear, time-invariant model. These models are then interconnected using linear algebraic relationships defined by their input-output variables. Compared with a generic state-space model [18], this method greatly reduces the computational effort of constructing a small-signal model and preserves modularity.

The small-signal model of each sub-component is described next, where all measurements and system parameters are considered in per-unit. The base rotational speed for all reference frames is denoted as ω_{b}.

2.2.1 Reference frame transformation

The state equation of the angle for reference frame transformation between GFM inverter-1 and GFM Inverter-2 is given by (2.4).

$$\dot{\delta} = \omega_{\mathrm{b}}(\omega_{\mathrm{gfm}_2} - \omega_{\mathrm{gfm}_1}) \tag{2.4}$$

The linearized version of (2.4) is given by (2.5).

$$\dot{\Delta\delta} = \omega_{\mathrm{b}}(\Delta\omega_{\mathrm{gfm}_2} - \Delta\omega_{\mathrm{gfm}_1}) \tag{2.5}$$

Alternatively, (2.5) may be written in the form shown in (2.6).

$$\dot{\Delta\delta} = A_{\delta}\Delta\delta + \boldsymbol{A_{\delta\mathbf{gfm_1}}\Delta X_{\mathbf{gfm_1}}} + \boldsymbol{A_{\delta\mathbf{gfm_2}}\Delta X_{\mathbf{gfm_2}}} \tag{2.6}$$

The expanded form of the matrices in (2.6) are given in Appendix B.1. The components of $\boldsymbol{\Delta X_{\mathbf{gfm}_i}}$ are explained in subsequent sections.

2.2.2 Power controller

The power controller consists of P-f and Q-v paths. The inverter's output active power, P_{t}, and reactive power, Q_{t}, are calculated at the terminals of the LC filter of the inverter. The dynamics of the proportional-integral (PI) controller in the Q-v control loop is modeled by the state variable x_1. The resulting set of non-linear equations that describes the power controller is given by (2.7)-(2.11).

$$\mathrm{d}\omega_{\mathrm{gfm}}/\mathrm{d}t = (1/2H_{\mathrm{gfm}})\,(P_{\mathrm{gfmref}} - P_{\mathrm{f}} + (\omega_{\mathrm{gfmref}} - \omega_{\mathrm{gfm}})/D_{\mathrm{pgfm}}) \tag{2.7}$$

$$\mathrm{d}P_{\mathrm{f}}/\mathrm{d}t = -\,(1/T_{\mathrm{p}})\,(P_{\mathrm{f}} - P_{\mathrm{t}}) \tag{2.8}$$

$$\mathrm{d}Q_{\mathrm{f}}/\mathrm{d}t = -\,(1/T_{\mathrm{q}})\,(Q_{\mathrm{f}} - Q_{\mathrm{t}}) \tag{2.9}$$

$$\mathrm{d}E_{\mathrm{f}}/\mathrm{d}t = -\,(1/T_{\mathrm{v}})\,(E_{\mathrm{f}} - E_{\mathrm{t}}) \tag{2.10}$$

$$\mathrm{d}x_1/\mathrm{d}t = D_{\mathrm{q}}\,(Q_{\mathrm{ref}} - Q_{\mathrm{f}}) + E_{\mathrm{ref}} - E_{\mathrm{f}} \tag{2.11}$$

where

$$P_{\mathrm{t}} = (v_{\mathrm{fd}} + (i_{\mathrm{cvd}} - i_{\mathrm{td}})R_{\mathrm{f}})i_{\mathrm{td}} + (v_{\mathrm{fq}} + (i_{\mathrm{cvq}} - i_{\mathrm{tq}})R_{\mathrm{f}})i_{\mathrm{tq}}$$

$$Q_{\mathrm{t}} = (v_{\mathrm{fq}} + (i_{\mathrm{cvq}} - i_{\mathrm{tq}})R_{\mathrm{f}})i_{\mathrm{td}} - (v_{\mathrm{fd}} + (i_{\mathrm{cvd}} - i_{\mathrm{td}})R_{\mathrm{f}})i_{\mathrm{tq}}$$

$$E_{\mathrm{t}} = ((v_{\mathrm{fd}} + (i_{\mathrm{cvd}} - i_{\mathrm{td}})R_{\mathrm{f}})^2 + (v_{\mathrm{fq}} + (i_{\mathrm{cvq}} - i_{\mathrm{tq}})R_{\mathrm{f}})^2)^{1/2}$$

After linearizing (2.7)-(2.11) the following equation is obtained.

$$\boldsymbol{\Delta \dot{X}_{P}} = \boldsymbol{A_{P}}\boldsymbol{\Delta X_{P}} + \boldsymbol{A_{PLCL}}\boldsymbol{\Delta X_{LCL}} + \boldsymbol{A_{PN}}\boldsymbol{\Delta X_{N}} + \boldsymbol{A_{PL}}\boldsymbol{\Delta X_{L}} + \boldsymbol{B_{P}}\boldsymbol{\Delta U_{gfm}} \tag{2.12}$$

The Q-v controller's output, v^*_{cvq}, is given by (2.13) and is linearized as in (2.14).

$$v_{\mathrm{cvq}}{}^{*} = -K_{\mathrm{p}}(D_{\mathrm{q}}(Q_{\mathrm{ref}} - Q_{\mathrm{f}}) + E_{\mathrm{ref}} - E_{\mathrm{f}}) - x_1/T_{\mathrm{i}} \tag{2.13}$$

$$\Delta {v_{\mathrm{cvq}}}^{*} = \boldsymbol{C_{\mathbf{E}}} \boldsymbol{\Delta X_{\mathbf{P}}} + \boldsymbol{D_{\mathbf{E}}} \boldsymbol{\Delta U_{\mathbf{gfm}}} \tag{2.14}$$

where

$$\boldsymbol{\Delta X_{\mathbf{P}}} = \begin{bmatrix} \Delta\omega_{\mathrm{gfm}} & \Delta P_{\mathrm{f}} & \Delta Q_{\mathrm{f}} & \Delta E_{\mathrm{f}} & \Delta x_1 \end{bmatrix}^{\mathrm{T}}$$

$$\boldsymbol{\Delta X_{\mathbf{LCL}}} = \begin{bmatrix} \Delta i_{\mathrm{cvd}} & \Delta i_{\mathrm{cvq}} & \Delta v_{\mathrm{fd}} & \Delta v_{\mathrm{fq}} & \Delta i_{\mathrm{td}} & \Delta i_{\mathrm{tq}} & \Delta i_{\mathrm{cvdhp}} & \Delta i_{\mathrm{cvqhp}} \end{bmatrix}^{\mathrm{T}}$$

$$\boldsymbol{\Delta X_{\mathbf{N}}} = \begin{bmatrix} \Delta v_{\mathrm{pid}} & \Delta v_{\mathrm{piq}} & \Delta i_{\mathrm{txd}} & \Delta i_{\mathrm{txq}} \end{bmatrix}^{\mathrm{T}} \quad \boldsymbol{\Delta X_{\mathbf{L}}} = \begin{bmatrix} \Delta v_{\mathrm{Ld}} & \Delta v_{\mathrm{Lq}} & \Delta i_{\mathrm{Ld}} & \Delta i_{\mathrm{Lq}} \end{bmatrix}^{\mathrm{T}}$$

$$\boldsymbol{\Delta U_{\mathbf{gfm}}} = \begin{bmatrix} \Delta\omega_{\mathrm{gfmref}} & \Delta P_{\mathrm{gfmref}} & \Delta Q_{\mathrm{ref}} & \Delta E_{\mathrm{ref}} \end{bmatrix}^{\mathrm{T}}$$

The expanded forms of the matrices in (2.12) and (2.14) are given in Appendix B.2.

2.2.3 *LC* filter and transformer

The dynamics of the LC filter and the transformer are included as explained in this section. High-frequency converter current components, which are introduced by the transient VI-based current controller, are included in this section for convenience. In this study the converter is operated below $i_{\mathrm{threshold}}$; therefore, the dynamics of the current-dependent VI path are excluded. The dq domain non-linear equations that govern the dynamics of the considered subgroup are given in (2.15) - (2.22).

$$\mathrm{d}i_{\mathrm{cvd}}/\mathrm{d}t = (\omega_{\mathrm{b}}/L_{\mathrm{f}})\left(R_{\mathrm{f}}(i_{\mathrm{td}} - i_{\mathrm{cvd}}) + \omega_{\mathrm{gfm}} L_{\mathrm{f}} i_{\mathrm{cvq}} + v_{\mathrm{cvd}} - v_{\mathrm{fd}}\right) \tag{2.15}$$

$$\mathrm{d}i_{\mathrm{cvq}}/\mathrm{d}t = (\omega_{\mathrm{b}}/L_{\mathrm{f}})\left(R_{\mathrm{f}}(i_{\mathrm{tq}} - i_{\mathrm{cvq}}) - \omega_{\mathrm{gfm}} L_{\mathrm{f}} i_{\mathrm{cvd}} + v_{\mathrm{cvq}} - v_{\mathrm{fq}}\right) \tag{2.16}$$

$$\mathrm{d}v_{\mathrm{fd}}/\mathrm{d}t = (\omega_{\mathrm{b}}/C_{\mathrm{f}})\left(\ \omega_{\mathrm{gfm}} C_{\mathrm{f}} v_{\mathrm{fq}} - i_{\mathrm{td}} + i_{\mathrm{cvd}}\right) \tag{2.17}$$

$$\mathrm{d}v_{\mathrm{fq}}/\mathrm{d}t = (\omega_{\mathrm{b}}/C_{\mathrm{f}})\left(-\omega_{\mathrm{gfm}} C_{\mathrm{f}} v_{\mathrm{fd}} - i_{\mathrm{tq}} + i_{\mathrm{cvq}}\right) \tag{2.18}$$

$$\mathrm{d}i_{\mathrm{td}}/\mathrm{d}t = (\omega_{\mathrm{b}}/L_{\mathrm{t}})\left(-(R_{\mathrm{f}}+R_{\mathrm{t}})i_{\mathrm{td}} + R_{\mathrm{f}}i_{\mathrm{cvd}} + \omega_{\mathrm{gfm}}L_{\mathrm{t}}i_{\mathrm{tq}} + v_{\mathrm{fd}} - v_{\mathrm{pid}}\right) \tag{2.19}$$

$$\mathrm{d}i_{\mathrm{tq}}/\mathrm{d}t = (\omega_{\mathrm{b}}/L_{\mathrm{t}})\left(-(R_{\mathrm{f}}+R_{\mathrm{t}})i_{\mathrm{tq}} + R_{\mathrm{f}}i_{\mathrm{cvq}} - \omega_{\mathrm{gfm}}L_{\mathrm{t}}i_{\mathrm{td}} + v_{\mathrm{fq}} - v_{\mathrm{piq}}\right) \tag{2.20}$$

$$\mathrm{d}i_{\mathrm{cvdhp}}/\mathrm{d}t = (-1/T_{\mathrm{hp}})i_{\mathrm{cvdhp}} + \mathrm{d}i_{\mathrm{cvd}}/\mathrm{d}t \tag{2.21}$$

$$\mathrm{d}i_{\mathrm{cvqhp}}/\mathrm{d}t = (-1/T_{\mathrm{hp}})i_{\mathrm{cvqhp}} + \mathrm{d}i_{\mathrm{cvq}}/\mathrm{d}t \tag{2.22}$$

where $T_{\mathrm{hp}} = 1/2\pi f_{\mathrm{hp}}$ (Refer to Fig. 2.2). Linearization of (2.15) - (2.22) results in (2.23).

$$\boldsymbol{\Delta \dot{X}_{LCL}} = \boldsymbol{A_{LCLd}}\boldsymbol{\Delta X_{LCL}} + \boldsymbol{B_{LCLd1}}\Delta\omega_{\mathrm{gfm}} + \boldsymbol{B_{LCLd2}}\begin{bmatrix}\Delta v_{\mathrm{cvd}}\\ \Delta v_{\mathrm{cvq}}\end{bmatrix} + \boldsymbol{B_{LCLd3}}\begin{bmatrix}\Delta v_{\mathrm{pid}}\\ \Delta v_{\mathrm{piq}}\end{bmatrix} \tag{2.23}$$

After accounting for the output of the Q-v controller and the transient VI path the relationships given in (2.24) - (2.25) are obtained for the expected dq components of the converter terminal voltage. Note that the transformer's winding configuration introduces a 30° phase shift, which is considered in these equations to refer all the low-voltage side quantities to the high-voltage side.

$$v_{\mathrm{cvd}} = ({v_{\mathrm{cvq}}}^{*})\sin(-30^{\circ}) - R_{\mathrm{vi0}}i_{\mathrm{cvdhp}} + \omega_{\mathrm{gfm}}L_{\mathrm{vi0}}i_{\mathrm{cvqhp}} \tag{2.24}$$

$$v_{\mathrm{cvq}} = ({v_{\mathrm{cvq}}}^{*})\cos(-30^{\circ}) - R_{\mathrm{vi0}}i_{\mathrm{cvqhp}} - \omega_{\mathrm{gfm}}L_{\mathrm{vi0}}i_{\mathrm{cvdhp}} \tag{2.25}$$

Linearizing (2.24) - (2.25) yields the following.

$$\begin{bmatrix}\Delta v_{\mathrm{cvd}}\\ \Delta v_{\mathrm{cvq}}\end{bmatrix} = \boldsymbol{A_{vcdqP}}\boldsymbol{\Delta X_{P}} + \boldsymbol{A_{vcvdqLCL}}\boldsymbol{\Delta X_{LCL}} + \boldsymbol{B_{vcvdq}}\boldsymbol{\Delta U_{gfm}} \tag{2.26}$$

Substituting (2.26) in (2.23) yields (2.27).

$$\boldsymbol{\Delta \dot{X}_{LCL}} = \boldsymbol{A_{LCLP}\Delta X_P} + \boldsymbol{A_{LCL}\Delta X_{LCL}} + \boldsymbol{A_{LCLN}\Delta X_N} + \boldsymbol{A_{LCLL}\Delta X_L} + \boldsymbol{B_{LCL}\Delta U_{gfm}} \tag{2.27}$$

The expanded forms of the matrices in (2.23), (2.26) and (2.27) are shown in Appendix B.3.

2.2.4 Network

The inverter-side capacitor and the inductance of the π-section are considered in developing the dynamic equations in (2.28) - (2.31).

$$\mathrm{d}v_{\mathrm{pid}}/\mathrm{d}t = (\omega_{\mathrm{b}}/C_{\mathrm{pi}})(\omega_{\mathrm{gfm}}C_{\mathrm{pi}}v_{\mathrm{piq}} + (i_{\mathrm{td}} - i_{\mathrm{txd}})) \tag{2.28}$$

$$\mathrm{d}v_{\mathrm{piq}}/\mathrm{d}t = (\omega_{\mathrm{b}}/C_{\mathrm{pi}})(-\omega_{\mathrm{gfm}}C_{\mathrm{pi}}v_{\mathrm{pid}} + (i_{\mathrm{tq}} - i_{\mathrm{txq}})) \tag{2.29}$$

$$\mathrm{d}i_{\mathrm{txd}}/\mathrm{d}t = (\omega_{\mathrm{b}}/L_{\mathrm{tx}})(\ \ \omega_{\mathrm{gfm}}L_{\mathrm{tx}}i_{\mathrm{txq}} - R_{\mathrm{tx}}i_{\mathrm{txd}} + v_{\mathrm{pid}} - v_{\mathrm{Ld}}) \tag{2.30}$$

$$\mathrm{d}i_{\mathrm{txq}}/\mathrm{d}t = (\omega_{\mathrm{b}}/L_{\mathrm{tx}})(-\omega_{\mathrm{gfm}}L_{\mathrm{tx}}i_{\mathrm{txd}} - R_{\mathrm{tx}}i_{\mathrm{txq}} + v_{\mathrm{piq}} - v_{\mathrm{Lq}}) \tag{2.31}$$

The expression in (2.32) are obtained after linearizing (2.28) - (2.31).

$$\boldsymbol{\Delta \dot{X}_N} = \boldsymbol{A_{Nd}\Delta X_N} + \boldsymbol{B_{Nd1}}\Delta\omega_{\mathrm{gfm}} + \boldsymbol{B_{Nd2}}\begin{bmatrix}\Delta i_{\mathrm{td}}\\ \Delta i_{\mathrm{tq}}\end{bmatrix} + \boldsymbol{B_{Nd3}}(\boldsymbol{B_{Nd4}}\Delta\delta + \boldsymbol{B_{Nd5}}\begin{bmatrix}\Delta v_{\mathrm{Ld}}\\ \Delta v_{\mathrm{Lq}}\end{bmatrix}) \tag{2.32}$$

Since the load is modeled in the GFM inverter-1's reference frame, the network component in GFM inverter-1's reference frame will have $\boldsymbol{B_{Nd3}B_{Nd4}}\Delta\delta = \boldsymbol{0}_{4\times1}$ and $\boldsymbol{B_{Nd5}} = \boldsymbol{I}_{2\times2}$. The equation (2.32) can be represented as in (2.33).

$$\boldsymbol{\Delta \dot{X}_N} = \boldsymbol{A_{N\delta}}\Delta\delta + \boldsymbol{A_{NP}\Delta X_P} + \boldsymbol{A_{NLCL}\Delta X_{LCL}} + \boldsymbol{A_N\Delta X_N} + \boldsymbol{A_{NL}\Delta X_L} + \boldsymbol{B_N\Delta U_{gfm}} \tag{2.33}$$

The expanded forms of the matrices in (2.32) - (2.33) are shown in Appendix B.4.

The above state equations are developed in individual inverter reference frames. Therefore, the overall state equations for the i^{th} inverter are obtained as follows.

$$\boldsymbol{\Delta \dot{X}_{\mathbf{gfm}_i}} = \boldsymbol{A_{\mathbf{gfm}\delta_i}}\Delta\delta + \boldsymbol{A_{\mathbf{gfm}_i}}\boldsymbol{\Delta X_{\mathbf{gfm}_i}} + \boldsymbol{A_{\mathbf{gfmLoad}_i}}\boldsymbol{\Delta X_{\mathbf{L}}} + \boldsymbol{B_{\mathbf{gfm}_i}}\boldsymbol{\Delta U_{\mathbf{gfm}_i}} \tag{2.34}$$

where,

$$\boldsymbol{\Delta X_{\mathbf{gfm}_i}} = \begin{bmatrix} \boldsymbol{\Delta X_{\mathbf{P}}} & \boldsymbol{\Delta X_{\mathbf{LCL}}} & \boldsymbol{\Delta X_{\mathbf{N}}} \end{bmatrix}^{\mathrm{T}}$$

$$\boldsymbol{A_{\mathbf{gfm}\delta_i}} = \begin{bmatrix} \boldsymbol{0}_{5\times1} & \boldsymbol{0}_{8\times1} & \boldsymbol{A_{\mathbf{N}\delta}} \end{bmatrix}^{\mathrm{T}}$$

$$\boldsymbol{A_{\mathbf{gfm}_i}} = \begin{bmatrix} \boldsymbol{A_{\mathbf{P}}} & \boldsymbol{A_{\mathbf{PLCL}}} & \boldsymbol{A_{\mathbf{PN}}} \\ \boldsymbol{A_{\mathbf{LCLP}}} & \boldsymbol{A_{\mathbf{LCL}}} & \boldsymbol{A_{\mathbf{LCLN}}} \\ \boldsymbol{A_{\mathbf{NP}}} & \boldsymbol{A_{\mathbf{NLCL}}} & \boldsymbol{A_{\mathbf{N}}} \end{bmatrix}$$

$$\boldsymbol{A_{\mathbf{gfmLoad}_i}} = \begin{bmatrix} \boldsymbol{A_{\mathbf{PL}}} & \boldsymbol{A_{\mathbf{LCLL}}} & \boldsymbol{A_{\mathbf{NL}}} \end{bmatrix}^{\mathrm{T}} \qquad \boldsymbol{B_{\mathbf{gfm}_i}} = \begin{bmatrix} \boldsymbol{B_{\mathbf{P}}} & \boldsymbol{B_{\mathbf{LCL}}} & \boldsymbol{B_{\mathbf{N}}} \end{bmatrix}^{\mathrm{T}}$$

2.2.5 Load

The dynamics of the load-side capacitances of each transmission line and the load inductance are modeled in GFM inverter-1's reference frame. The non-linear dynamic equations of this sub-group are given in (2.35)-(2.38). C_{L} is the total shunt capacitance and N is the number of parallel active devices that inject current to the load via π-section components. Current flows in the transmission lines are the inputs to this section. The current flow in the line that connects the GFM inverter-2 must be transformed to GFM inverter-1's reference frame using the transformation matrix given in (2.2).

$$\mathrm{d}v_{\mathrm{Ld}}/\mathrm{d}t = (\omega_{\mathrm{b}}/C_{\mathrm{L}})(\ \omega_{\mathrm{gfm}_1}C_{\mathrm{L}}v_{\mathrm{Lq}} - v_{\mathrm{Ld}}/R_{\mathrm{L}} - i_{\mathrm{Ld}} + \sum_{i=1}^{N} i_{\mathrm{txd}i}) \tag{2.35}$$

$$\mathrm{d}v_{\mathrm{Lq}}/\mathrm{d}t = (\omega_{\mathrm{b}}/C_{\mathrm{L}})(-\omega_{\mathrm{gfm}_1} C_{\mathrm{L}} v_{\mathrm{Ld}} - v_{\mathrm{Lq}}/R_{\mathrm{L}} - i_{\mathrm{Lq}} + \sum_{i=1}^{N} i_{\mathrm{txq}i}) \tag{2.36}$$

$$\mathrm{d}i_{\mathrm{Ld}}/\mathrm{d}t = (\omega_{\mathrm{b}}/L_{\mathrm{L}})(\ \ \omega_{\mathrm{gfm}_1} L_{\mathrm{L}} i_{\mathrm{Lq}} + v_{\mathrm{Ld}}) \tag{2.37}$$

$$\mathrm{d}i_{\mathrm{Lq}}/\mathrm{d}t = (\omega_{\mathrm{b}}/L_{\mathrm{L}})(-\omega_{\mathrm{gfm}_1} L_{\mathrm{L}} i_{\mathrm{Ld}} + v_{\mathrm{Lq}}) \tag{2.38}$$

After linearization of (2.35) - (2.38) the state equation given in (2.39) is obtained. The expanded form of matrices in (2.39) are given in Appendix B.5.

$$\boldsymbol{\Delta \dot{X}_{\mathbf{L}}} = \boldsymbol{A_{\mathbf{Ld}}} \boldsymbol{\Delta X_{\mathbf{L}}} + \boldsymbol{B_{\mathbf{Ld1}}} \Delta\omega_{\mathrm{gfm}_1} + \boldsymbol{B_{\mathbf{Ld2}}} \Delta R_{\mathrm{L}} + \boldsymbol{B_{\mathbf{Ld3}}} \sum_{i=1}^{N} (\boldsymbol{B_{\mathbf{Ld4}_i}} \Delta\delta + \boldsymbol{B_{\mathbf{Ld5}_i}} \begin{bmatrix} \Delta i_{\mathrm{txd}_i} \\ \Delta i_{\mathrm{txq}_i} \end{bmatrix}) \tag{2.39}$$

Since load is modeled in GFM inverter-1's reference frame $\boldsymbol{B_{\mathbf{Ld3}}} \boldsymbol{B_{\mathbf{Ld4_1}}} \Delta\delta = \boldsymbol{0}_{4\times 1}$ and $\boldsymbol{B_{\mathbf{Ld5_1}}} = \boldsymbol{I}_{2\times 2}$. Eq. (2.39) can be rearranged as shown in (2.40). The expanded form of matrices is given in Appendix B.5.

$$\boldsymbol{\Delta \dot{X}_{\mathbf{L}}} = \boldsymbol{A_{\mathbf{Load\delta}}} \Delta\delta + \sum_{i=1}^{N} (\boldsymbol{A_{\mathbf{Loadgfm}_i}} \boldsymbol{\Delta X_{\mathbf{gfm}_i}}) + \boldsymbol{A_{\mathbf{Load}}} \boldsymbol{\Delta X_{\mathbf{L}}} + \boldsymbol{B_{\mathbf{Load}}} \boldsymbol{\Delta U_{\mathbf{L}}} \tag{2.40}$$

2.2.6 Overall system

The small-signal model of the entire system can be obtained by combining the linearized equations of the sub-components as shown in (2.41).

$$\boldsymbol{\dot{\Delta X}} = \boldsymbol{A} \boldsymbol{\Delta X} + \boldsymbol{B} \boldsymbol{\Delta U} \tag{2.41}$$

where

$$\boldsymbol{\Delta X} = \begin{bmatrix} \boldsymbol{\Delta\delta} & \boldsymbol{\Delta X_{\mathbf{gfm_1}}} & \boldsymbol{\Delta X_{\mathbf{gfm_2}}} & \boldsymbol{\Delta X_{\mathbf{L}}} \end{bmatrix}^{\mathrm{T}}$$

$$\boldsymbol{\Delta U} = \begin{bmatrix} \boldsymbol{\Delta U_{\mathbf{gfm_1}}} & \boldsymbol{\Delta U_{\mathbf{gfm_2}}} & \boldsymbol{\Delta R_{\mathbf{L}}} \end{bmatrix}^{\mathrm{T}}$$

$$\boldsymbol{A} = \begin{bmatrix} A_\delta & \boldsymbol{A_{\delta gfm_1}} & \boldsymbol{A_{\delta gfm_2}} & \boldsymbol{0}_{1\times4} \\ \boldsymbol{A_{gfm\delta_1}} & \boldsymbol{A_{gfm_1}} & \boldsymbol{0}_{17\times17} & \boldsymbol{A_{gfmLoad_1}} \\ \boldsymbol{A_{gfm\delta_2}} & \boldsymbol{0}_{17\times17} & \boldsymbol{A_{gfm_2}} & \boldsymbol{A_{gfmLoad_2}} \\ \boldsymbol{A_{Load\delta}} & \boldsymbol{A_{Loadgfm_1}} & \boldsymbol{A_{Loadgfm_2}} & \boldsymbol{A_{Load}} \end{bmatrix} \quad \boldsymbol{B} = \begin{bmatrix} \boldsymbol{0}_{1\times4} & \boldsymbol{0}_{1\times4} & \boldsymbol{0}_{1\times1} \\ \boldsymbol{B_{gfm1}} & \boldsymbol{0}_{17\times4} & \boldsymbol{0}_{1\times1} \\ \boldsymbol{0}_{17\times4} & \boldsymbol{B_{gfm2}} & \boldsymbol{0}_{1\times1} \\ \boldsymbol{0}_{4\times4} & \boldsymbol{0}_{4\times4} & \boldsymbol{B_{Load}} \end{bmatrix}$$

2.2.7 Small-signal model validation

The developed small-signal model is validated against a detailed electromagnetic transient (EMT) model in PSCAD/EMTDC. The time-domain responses obtained from the linearized model and the detailed EMT model to a 10% decrement of load resistance at $t = 5$ s and a 2.5% increment of load resistance at $t = 7.5$ s, a 1% increment of voltage reference of GFM inverter-1 at $t = 5$ s and 1% increment of GFM inverter-1's active power reference at $t = 5$ s are given in Figs. 2.6(a), 2.6(b), and 2.6(c), respectively. These tests and others (not shown for brevity) verify the developed small-signal model's ability to track the EMT model's low-frequency content for adequately small disturbances around an operating point.

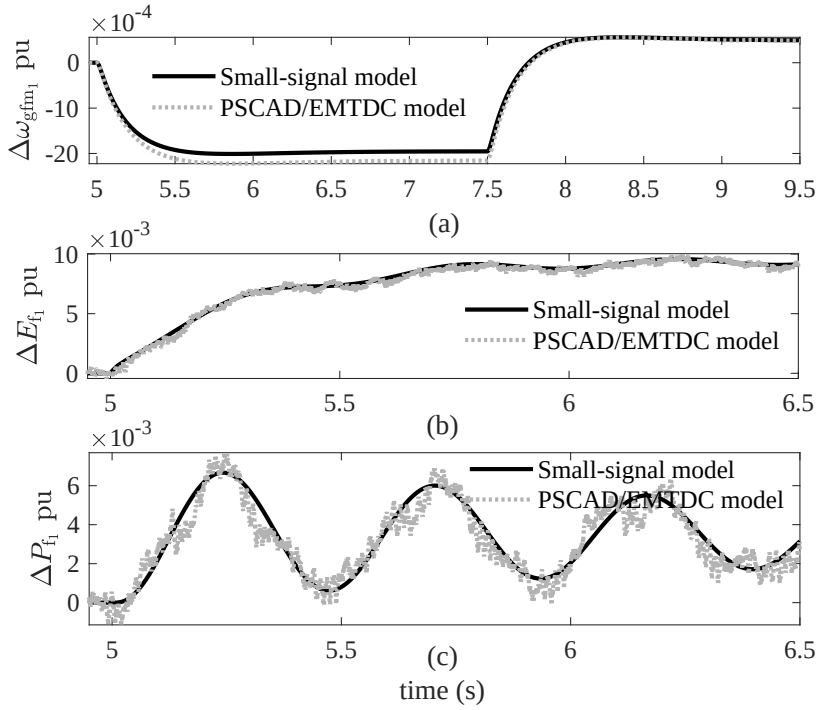

Fig. 2.6: Small-signal vs EMT response for (a) $\Delta R_{\mathrm{L}} = -10\%$ at t = 5 s and $\Delta R_{\mathrm{L}} = 2.5\%$ at t = 7.5 s, (b) $\Delta E_{\mathrm{ref}_1} = 1\%$ at t = 5 s and (c) $\Delta P_{\mathrm{gfmref}_1} = 1\%$ at t = 5 s.

2.3 Eigenvalue Analysis

The eigenvalues of $\boldsymbol{A}$ in (2.41) reveal a critical mode in the system as described in Table 2.3. The virtual electromechanical parameters significantly participate in this mode. Therefore, this mode is identified as a virtual electromechanical mode. Multi-synchronous machine systems show inter-machine oscillations around the same oscillation frequency range [19] when low damping is present. Since the considered GFM controller emulates a low-order model of the synchronous machine, a similar inter-machine oscillation appears. The ability of the GFM inverter to introduce a wide range of interactions depending on the controller and circuit topologies will be revealed in the next chapters.

Table 2.3: Major Participants in the Critical Mode

Mode	**Freq.** (Hz)	$\boldsymbol{\zeta}$ (%)	**Major participants**
1	2.2	3.7	δ[100%], ω_{gfm_1}[43%], ω_{gfm_2}[43%], i_{cvd_1} [36%], i_{cvd_2} [36%], i_{cvdhp_1} [35%], i_{cvdhp_2} [35%]

According to participation factor analysis, the dominant states are chiefly associated with the *P-f* controller and the transient VI paths. The inertia time constant (H_{gfm}) and droop coefficient (D_{pgfm}) mainly govern the dynamics of the *P-f* controller, while the dynamics of the transient VI are determined by the gains (R_{vi0}, L_{vi0}) and the cut-off frequency (f_{hp}). Other than the controller states, converter currents' d-components have significant participation. Therefore, the *LC* filter's inductance is changed to evaluate its impact. The list of control and network parameters that are selected to identify their effect on the critical mode is given below.

- The parameters related to virtual electromechanical characteristics (H_{gfm}, D_{pgfm}).
- The control parameters of transient virtual impedance path (R_{vi0}, L_{vi0}, f_{hp}).
- The *LC* filter inductance (L_{f}).

The results obtained for the above parameter changes are presented in the following sections.

2.3.1 The effect of virtual electromechanical characteristics

The virtual electromechanical characteristics are chiefly governed by the virtual inertia time constant (H_{gfm}) and the virtual *P-f* droop co-efficient (D_{pgfm}). Therefore, this section analyzes the effect of those parameters.

Effect of H_{gfm}

To analyze the effect of H_{gfm}, its value is changed from 0.1 s to 5 s in one of the GFM inverters (e.g. GFM-inverter-1) and equally in both the GFM inverters. The movement of eigenvalue corresponding to these changes is depicted in Fig. 2.7a. This shows that either one of the GFM inverters or both the GFM inverters with large inertia time constants tend to interact more. The GFM inverters that emulate large inertia time constants prone to disturbances with low-frequency excursions and oscillatory frequencies. However, due to the sluggish controller action with a high inertia time constant, the oscillations will take a longer time to decay. With low-inertia time constants, the GFM controller can fast act to changes. Though relatively a high-frequency oscillation is observed than GFM inverters that emulate large inertia time constants, those oscillations can decay faster.This explains the reason behind the effect on the virtual electromechanical mode from the virtual inertia time constant.

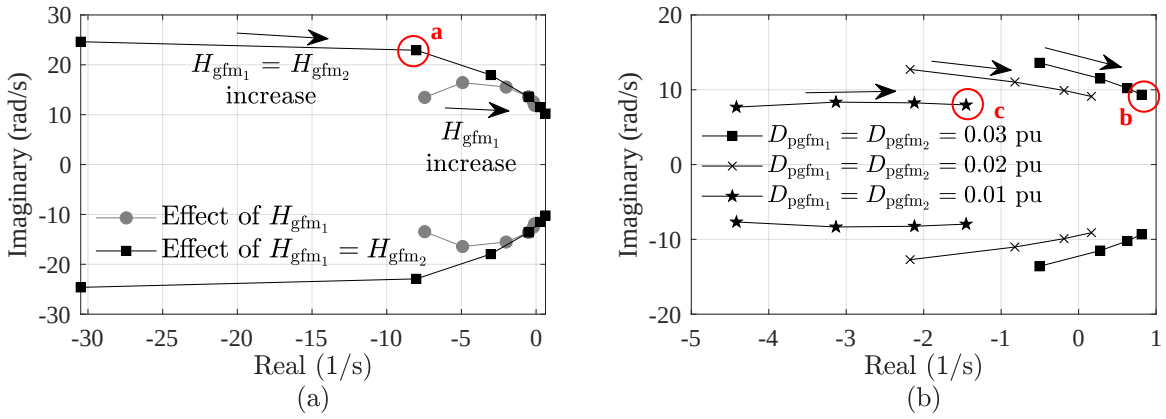

Fig. 2.7: Locus of eigenvalue for changes in (a) H_{gfm} of one of the GFM inverters and both the GFM inverters (b) D_{pgfm} and H_{gfm} of both the GFM inverters.

For some large inertia time constant values, the system can even reach instability. The stability of parallel connected GFM inverters with large inertia time constants can be improved by introducing more damping. The blocks of *P-f* controller (in Fig. 2.3a) that generate ω_{gfm} can be represented from (2.42).

$$2H_{\text{gfm}}\text{d}\Delta\omega_{\text{gfm}}/\text{d}t = P_{\text{gfmref}} - P_{\text{f}} - (1/D_{\text{pgfm}})\Delta\omega_{\text{gfm}} \tag{2.42}$$

As shown in (2.42), $(1/D_{\text{pgfm}})\Delta\omega_{\text{gfm}}$ introduces a damping power. Therefore, by reducing D_{pgfm}, more damping can be introduced. To test this, as shown in Fig. 2.7b, H_{gfm} of both the GFM inverters are changed between 2 s and 5 s, with D_{pgfm} of 0.01 pu, 0.02 pu and 0.03 pu in both the GFM inverters. The arrow by each graph shows the direction of the eigenvalue movement with increments of H_{gfm}. This shows that GFM inverters with large inertia time constants can achieve improved stability by decreasing *P-f* droop co-efficient.

To validate the results of the eigenvalue analysis, PSCAD/EMTDC responses are obtained for the operating points marked using red circles in Fig.2.7 by applying a 5% P_{gfmref_1} impulse a t = 5 s for 0.1 s. The improper selection of the disturbance can not excite the mode as explained in [23]. Therefore, following the controllability matrix analysis the aforementioned disturbance is selected for this study. As shown in Fig.2.8 the low-inertia time constant of GFM inverters gives improved damping for inter GFM inverter interactions at electromechanical oscillation range. Further, negatively damped interaction among GFM inverters with large inertia time constants (Fig.2.8b) can be improved by introducing additional damping via *P-f* droop co-efficient (Fig.2.8c).

Effect of D_{pgfm}

The effect of D_{pgfm} on the critical mode is analyzed by changing its value from 0.01 pu to 0.05 pu in one of the GFM inverters and equally in both the GFM inverters. Fig.2.9 depicts the movement of eigenvalue with these changes. Large D_{pgfm} values of either one of the GFM

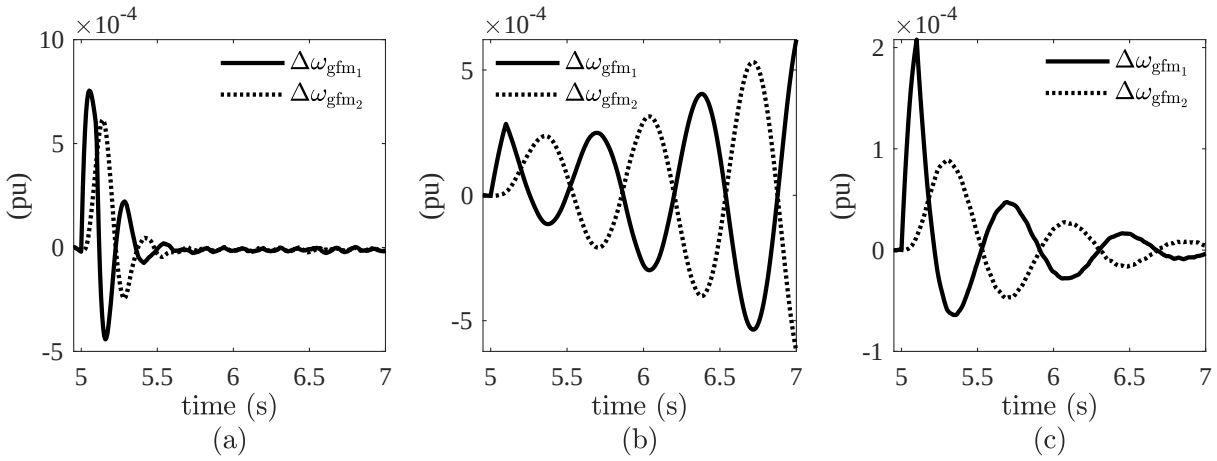

Fig. 2.8: The rotational speed variation for a 5% P_{gfmref_1} impulse at t = 5 s for 0.1 s with (a) H_{gfm} = 0.5 s with D_{pgfm} =0.03 pu (b) H_{gfm} = 5 s with D_{pgfm} =0.03 pu and (c) H_{gfm} = 5 s with D_{pgfm} =0.01 pu.

inverters or both the GFM inverters reduce the stability of the system, as the increment of *P-f* droop co-efficient reduces the amount of power exchange for a given frequency deviation. To validate this argument, PSCAD/EMTDC responses for a 5% P_{gfmref_1} impulse at t= 5 s for 0.1 s with D_{pgfm} of both the machines at 0.01 pu and 0.04 pu (marked in red circles in Fig.2.9) are obtained and given in Fig.2.10. As shown in Fig.2.10a, D_{pgfm} = 0.01 pu value has given an improved damping to the system, while D_{pgfm} = 0.04 pu has brought the system to instability (Fig.2.10b). This verifies the results obtained from the eigenvalue analysis.

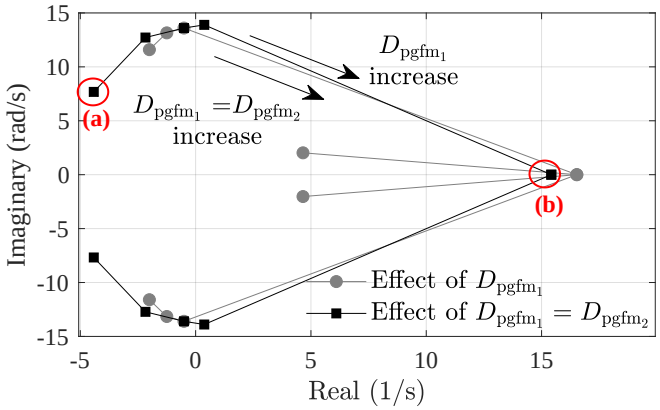

Fig. 2.9: Locus of eigenvalue for changes in D_{pgfm} of one of the GFM inverters and both the GFM inverters.

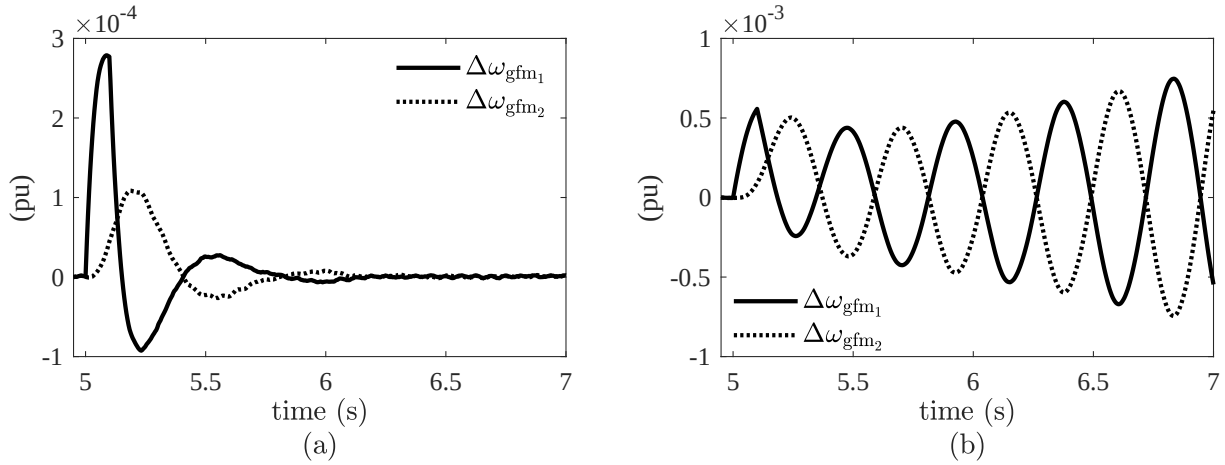

Fig. 2.10: The rotational speed variation for a 5% P_{gfmref_1} impulse at t = 5 s for 0.1 s with (a) $D_{\text{pgfm}} = 0.01$ pu and (b)$D_{\text{pgfm}} = 0.04$ pu.

As mentioned under the effect of H_{gfm} and D_{pgfm}, the effect of changing either one of the GFM inverter's parameters or both the GFM inverter's parameters preserves the same trend in impacting the critical mode. However, the mode is significantly sensitive to the change in both the GFM inverters. Therefore, the rest of the sensitivity studies are conducted by changing the corresponding parameters in both the GFM inverters.

2.3.2 Effect of transient VI path

The effect of the transient VI path is mainly analyzed by changing R_{vi0}, L_{vi0} and f_{hp}, while some extended studies are conducted to analyze the effect of X/R ratio and the magnitude of the transient VI (Z_{vi0}). The traces of eigenvalue corresponding to these changes are depicted in Fig.2.11. The arrows by each curve show the direction of eigenvalue movement with the increment of the corresponding parameter.

The traces in Fig.2.11a are obtained with $f_{\text{hp}} = 0.5$ Hz. To analyze the effect of R_{vi0} its value is changed from 0 to 1 pu while keeping $L_{\text{vi0}} = 0$. Similarly, the effect of L_{vi0} is analyzed. As shown in Fig.2.11a, the increment of transient virtual resistance value reduces the damping of the mode, while the increment of transient virtual inductance improves the damping of the mode. To analyze the effect of the X/R ratio of the virtual impedance on

the critical mode, its value is changed from 0.1 to 5, while keeping the magnitude of the transient virtual impedance at 1.0 pu. Fig.2.11a shows that a large X/R ratio gives improved damping. This is because of the improved decoupling offered by the increased X/R ratio for P-f and Q-v droop paths. Further, the effect of the transient virtual impedance's magnitude, Z_{vi0}, is analyzed by changing its value from 0 to 1.0 pu, while keeping the X/R ratio at 2 (as this shows improved damping). Fig.2.11a shows that large Z_{vi0} values give improved damping.

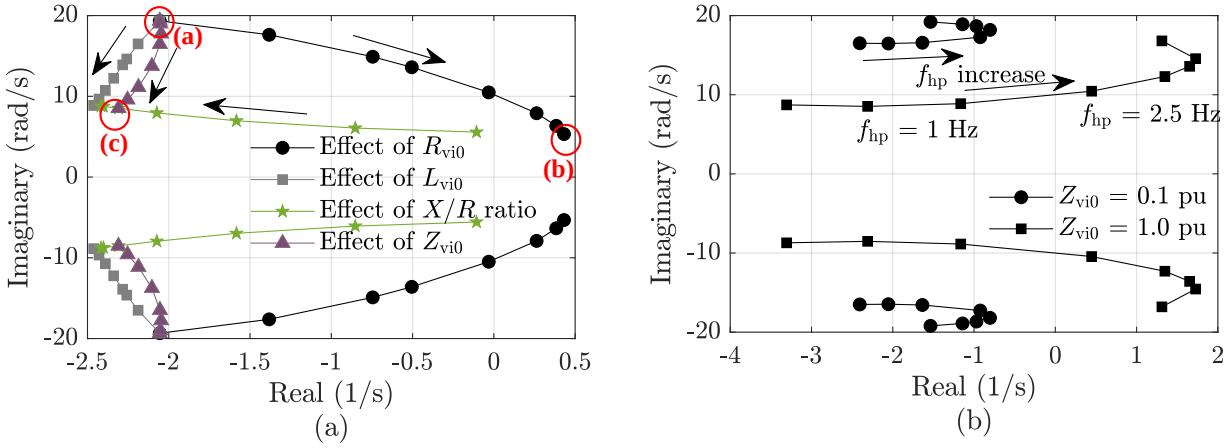

Fig. 2.11: Locus of eigenvalue for changes in (a) R_{vi0}, L_{vi0}, X/R ratio and Z_{vi0} and (b) f_{hp} with two Z_{vi0} values.

The effect of the high-pass filter cut-off frequency, f_{hp}, is analyzed by changing its value from 0.1 Hz to 20 Hz. As shown in Fig.2.11b the selection of the cut-off frequency to pass the critical mode's oscillatory frequency has improved the damping of the mode. The sensitivity of the mode to f_{hp} is significant with large Z_{vi0} values as it increases the contribution of the transient VI path in the GFM controller. To validate the eigenvalue analysis, PSCAD/EMTDC responses for a 5% P_{gfmref_1} impulse at t = 5 s for 0.1 s are obtained for the operating conditions marked in red circles in Fig.2.11a. As shown in Fig.2.12a without transient VI path, the system experiences a low-damped oscillatory mode as predicted by the eigenvalue analysis. This can be worsened with a high R_{vi0} value and improved with a high X/R ratio as shown in Figs.2.12b and 2.12c, respectively. Therefore, careful selection of transient VI path parameters can improve the damping of this critical mode.

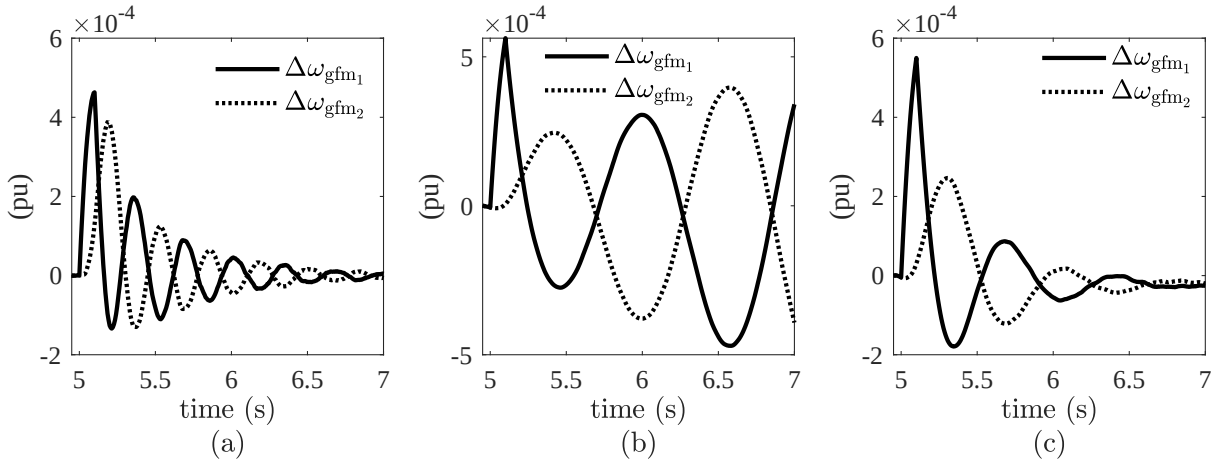

Fig. 2.12: The rotational speed variation for a 5% P_{gfmref_1} impulse at t = 5 s for 0.1 s with (a) R_{vi0}=L_{vi0}=0, (b) R_{vi0}=1 and L_{vi0}=0 and (c) R_{vi0}=0.44 pu and L_{vi0}=0.88 pu.

2.3.3 Effect of filter inductance

Due to the substantial participation of d-components of the converter current in the critical mode, the LC filter inductance of both the GFM inverters is changed from 0.03 pu to 0.30 pu. This will change the tuned frequency of the filter and it is recommended to change the filter capacitor value along with it. However, due to the low-frequency interaction of interest, this change will not affect the following results. The tendency to reach instability with low filter inductance values is shown in Fig.2.13. The decrement of the X/R ratio of the network and the reduction of the electrical distance between two GFM inverters have evoked the tendency to interact between these two inverters. The benefit of having an inductance dominant system is observed with the transient VI path in section 2.3.2 as well. However, the selection of the upper limit of the filter inductance value is subjected to the voltage drop across it. PSCAD/EMTDC responses for a 5% P_{gfmref_1} impulse at t = 8 s for 0.1 s are obtained for the operating points marked in red circles in Fig.2.13. As shown in Fig.2.14, low values of filter inductance can lead to system instability and properly sized filter inductances provide damping to interactions between GFM inverters. This validates the results obtained from eigenvalue analysis.

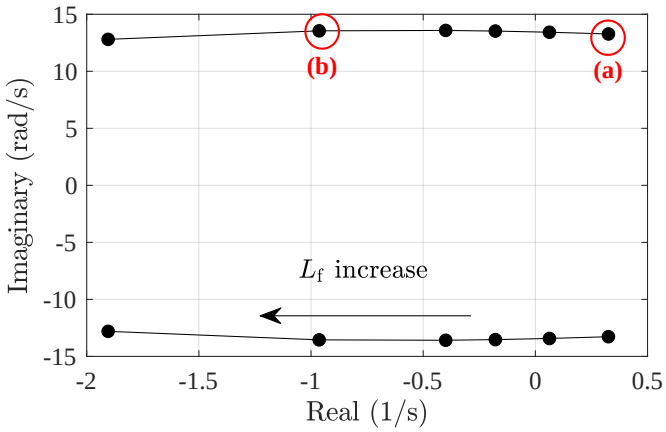

Fig. 2.13: Locus of eigenvalue for changes of L_f in both the GFM inverters.

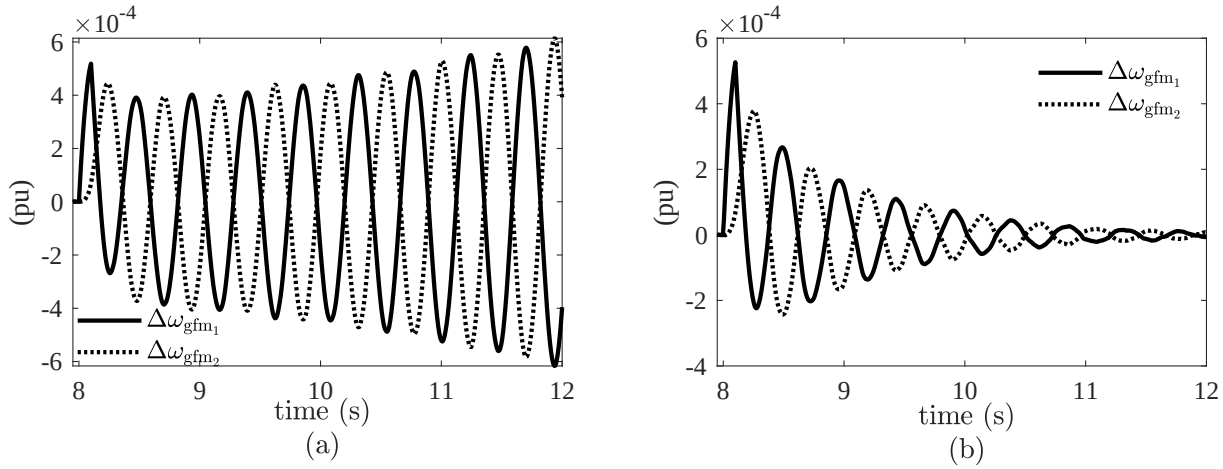

Fig. 2.14: The rotational speed variation for a 5% P_{gfmref_1} impulse at t = 8 s for 0.1 s with (a) $L_f = 0.03$ pu and (b) $L_f = 0.15$ pu.

2.4 Summary

This chapter analyzed the interactions that may occur in a parallel-connected GFM inverter system in the islanded mode. The key contributions of the chapter are:

- Development and validation of a small-signal mode for the exemplar system of parallel-connected GFM inverters in the islanded mode by including the full dynamics of the VSM layer, transient virtual impedance path, and network.

- Identification of root causes for the virtual electromechanical interaction between paralleled GFM inverters as high virtual inertia time constant, high $\Delta f/\Delta P$ coefficient,

i.e., D_{p}, and low X/R ratio in the impedance (i.e., both virtual and actual).

Chapter 3

Modeling and Analysis of Interactions between Grid-Forming Inverters and Synchronous Machines

3.1 Introduction

The interaction analysis of a multi-GFM inverter system in the islanded mode was discussed in Chapter 2. This chapter extends the analysis by identifying the interactions that can happen in the grid-connected mode of the GFM inverters. To represent a more general scenario a local load is added to the point of interconnection. A system consisting of a GFM inverter in parallel with a synchronous machine that utilizes an exciter and a governor-turbine system is studied. This represents a common configuration in modern applications, where the synchronous machine and the GFM inverter represent aggregate models of synchronous machines and GFM inverters in the system, respectively. Furthermore, utilizing a synchronous machine for external ac system representation allows capturing system dynamics that would otherwise have been overlooked by an ideal Thevenin equivalent.

The test system and its parameters are discussed in section 3.2. The small-signal model

development of the GFM inverter and the network components are similar to Chapter 2. Therefore, the small-signal model development is limited to the synchronous machine as shown in section 3.3. The eigenvalue analysis in section 3.4 is followed by the chapter summary and its key contributions in section 3.5.

3.2 Test System

Fig. 3.1 gives the considered test system for interaction analysis in the grid-connected mode of the GFM inverter. The GFM controller topology, the parameters of the controller and the network are the same as in Chapter 2. A round rotor synchronous machine model is considered in the study.

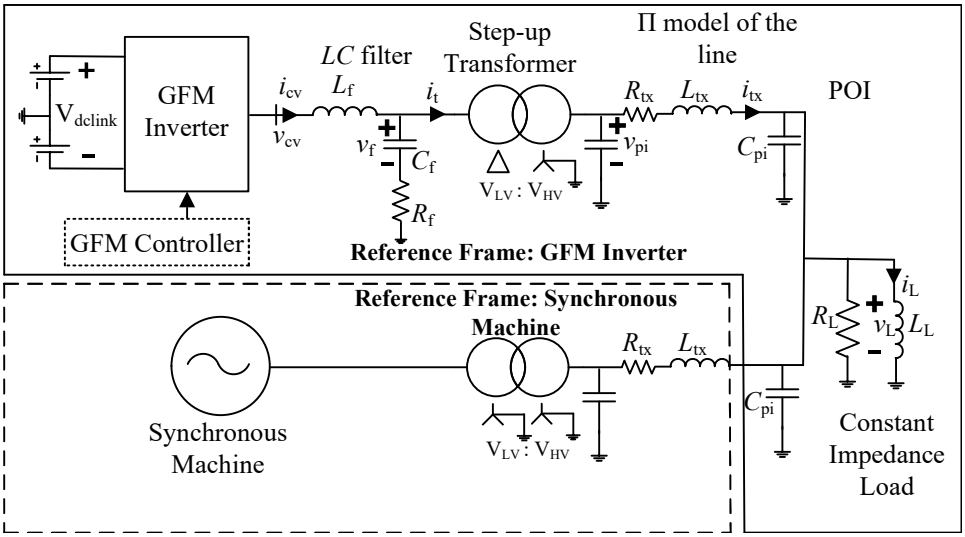

Fig. 3.1: Test system to study interactions between a GFM inverter and a synchronous machine.

The governor-turbine models that are applicable for load-frequency studies are adopted from [19] and depicted in Fig.3.2(a). The AC4A exciter model is used whose block diagram is given in Fig.3.2(b). The parameters of the synchronous machine, governor-turbine, and exciter are given in Table 3.1.

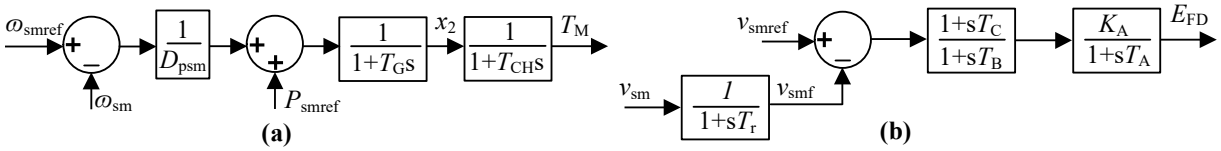

Fig. 3.2: Block diagram representation of (a) governor and turbine model, and (b) AC4A exciter model.

Table 3.1: List of Parameters of the Synchronous Machine

Ratings: $V_{\mathrm{LN,rms}} = 7.97$ kV, $I_{\mathrm{rms}} = 1.046$ kA	**Mechanical parameters**: $H_{\mathrm{sm}} = 3$ s
Steady-state parameters: $R_{\mathrm{a}} = 0.0014$ pu, $x_{\mathrm{l}} = 0.134$ pu, $x_{\mathrm{d}} = 1.25$ pu, $x_{\mathrm{q}} = 1.25$ pu	**Transient-state parameters:** $x_{\mathrm{d}}^{'} = 0.232$ pu, $x_{\mathrm{q}}^{'} = 0.715$ pu, $T_{\mathrm{do}}^{'} = 4.75$ s, $T_{\mathrm{qo}}^{'} = 1.5$ s
Sub-transient-state parameters: $x_{\mathrm{d}}^{''} = 0.15$ pu, $x_{\mathrm{q}}^{''} = 0.15$ pu, $T_{\mathrm{do}}^{''} = 0.059$ s, $T_{\mathrm{qo}}^{''} = 0.21$ s	**Governor-turbine parameters and inputs** $P_{\mathrm{smref}} = 0.7$ pu, $\omega_{\mathrm{smref}} = 1.0$ pu, $D_{\mathrm{psm}} = 0.03$ pu, $T_{\mathrm{G}} = 0.2$ s, $T_{\mathrm{CH}} = 0.3$ s
AC4A exciter parameters and inputs $V_{\mathrm{smref}} = 1.05$ pu, $K_{\mathrm{A}} = 200.0$, $T_{\mathrm{A}} = 0.015$ s,$T_{\mathrm{B}} = 10.0$ s, $T_{\mathrm{C}} = 1.0$ s, $T_{\mathrm{r}} = 0.02$ s	

3.3 Small-Signal Model Development

This section explicitly discusses the small-signal model development of the synchronous machine as GFM inverter's and network components' small-signal model development have been discussed in Chapter 2.

3.3.1 Reference frame transformation

The reference angle required for the transformation of boundary state variables between the synchronous machine's reference frame and the GFM inverter's reference frame is obtained from (3.1). The linearized representation of (3.1) can be obtained as shown in (3.2) whose expanded form of matrices given in Appendix C.4.1.

$$\mathrm{d}\delta/\mathrm{d}t = \omega_{\mathrm{b}}(\omega_{\mathrm{sm}} - \omega_{\mathrm{gfm}}) \tag{3.1}$$

$$\dot{\Delta\delta} = A_{\delta}\Delta\delta + \boldsymbol{A_{\delta \mathbf{gfm}}\Delta X_{\mathbf{gfm}}} + \boldsymbol{A_{\delta \mathbf{sm}}\Delta X_{\mathbf{sm}}} \tag{3.2}$$

3.3.2 Synchronous machine modeling

Synchronous machine modeling is based on the guidelines in [19]. The mechanical dynamics of the synchronous machine is modeled using the swing equation in (3.3), where T_{m} and T_{e} are the input mechanical torque and the output electrical torque of the synchronous machine in per unit, respectively.

$$\mathrm{d}\omega_{\mathrm{sm}}/\mathrm{d}t = (1/2H_{\mathrm{sm}})\,(T_{\mathrm{m}} - T_{\mathrm{e}} - K_{\mathrm{D}}(\omega_{\mathrm{sm}} - \omega_{\mathrm{smref}})) \tag{3.3}$$

The electrical dynamics of the synchronous machine are modeled by the stator and rotor fluxes as detailed in [19]. Since network dynamics are modeled using dynamic phasors, the synchronous machine's stator winding dynamics need to be considered. To derive a linearized model of the synchronous machine that provides a seamless integration with the rest of the linearized components of the system, the synchronous machine's connecting transformer impedance is assumed in series with the stator winding. The steps in the derivation process are given in Appedices C.1-C.3 and the resultant set of dynamic equations that govern the electrical dynamics of the synchronous machine is given in (3.4)-(3.9).

$$\mathrm{d}i_{\mathrm{d}}/\mathrm{d}t = (\omega_{\mathrm{b}}/L_{\mathrm{t}})\,(-R_{\mathrm{t}}i_{\mathrm{d}} - v_{\mathrm{pid}} + e_{\mathrm{d}} + L_{\mathrm{t}}\omega_{\mathrm{sm}}i_{\mathrm{q}}) \tag{3.4}$$

$$\mathrm{d}\psi_{\mathrm{fd}}/\mathrm{d}t = k_1\psi_{\mathrm{fd}} + k_2\psi_{1\mathrm{d}} + k_3 i_{\mathrm{d}} + k_4 E_{\mathrm{fd}} \tag{3.5}$$

$$\mathrm{d}\psi_{1\mathrm{d}}/\mathrm{d}t = k_5\psi_{\mathrm{fd}} + k_6\psi_{1\mathrm{d}} + k_7 i_{\mathrm{d}} \tag{3.6}$$

$$\mathrm{d}i_{\mathrm{q}}/\mathrm{d}t = (\omega_{\mathrm{b}}/L_{\mathrm{t}})\,(-R_{\mathrm{t}}i_{\mathrm{q}} - v_{\mathrm{piq}} + e_{\mathrm{q}} - L_{\mathrm{t}}\omega_{\mathrm{sm}}i_{\mathrm{d}}) \tag{3.7}$$

$$\mathrm{d}\psi_{1\mathrm{q}}/\mathrm{d}t = k_8\psi_{1\mathrm{q}} + k_9\psi_{2\mathrm{q}} + k_{10} i_{\mathrm{q}} \tag{3.8}$$

$$\mathrm{d}\psi_{2\mathrm{q}}/\mathrm{d}t = k_{11}\psi_{1\mathrm{q}} + k_{12}\psi_{2\mathrm{q}} + k_{13} i_{\mathrm{q}} \tag{3.9}$$

The constants $k_1 - k_{13}$ depend on the synchronous machine parameters and mentioned in

Appendix C.1. Linearization of (3.3)-(3.9) results in (3.10) whose expanded form of matrices are given in Apppendix. C.4.2.

$$\boldsymbol{\Delta \dot{X}_{\mathbf{m}}} = \boldsymbol{A_{\mathbf{m}}} \boldsymbol{\Delta X_{\mathbf{m}}} + \boldsymbol{A_{\mathbf{mGT}}} \boldsymbol{\Delta X_{\mathbf{GT}}} + \boldsymbol{A_{\mathbf{mE}}} \boldsymbol{\Delta X_{\mathbf{E}}} + \boldsymbol{A_{\mathbf{mN}}} \boldsymbol{\Delta X_{\mathbf{N}}} + \boldsymbol{A_{\mathbf{mL}}} \boldsymbol{\Delta X_{\mathbf{L}}} + \boldsymbol{B_{\mathbf{m}}} \boldsymbol{\Delta U_{\mathbf{sm}}} \tag{3.10}$$

where,

$$\boldsymbol{\Delta X_{\mathbf{m}}} = \begin{bmatrix} \Delta\omega_{\mathrm{sm}} & i_{\mathrm{d}} & \psi_{\mathrm{fd}} & \psi_{1\mathrm{d}} & i_{\mathrm{q}} & \psi_{1\mathrm{q}} & \psi_{2\mathrm{q}} \end{bmatrix}^{\mathrm{T}}$$

$$\boldsymbol{\Delta X_{\mathbf{GT}}} = \begin{bmatrix} \Delta x_2 & \Delta T_{\mathrm{m}} \end{bmatrix}^{\mathrm{T}} \quad \boldsymbol{\Delta X_{\mathbf{E}}} = \begin{bmatrix} \Delta v_{\mathrm{smf}} & \Delta x_3 & \Delta E_{\mathrm{fd}} \end{bmatrix}^{\mathrm{T}} \quad \boldsymbol{\Delta U_{\mathbf{sm}}} = \begin{bmatrix} \Delta P_{\mathrm{smref}} & \Delta v_{\mathrm{smref}} \end{bmatrix}^{\mathrm{T}}$$

3.3.3 Governor-turbine system

The dynamic equations that describe the considered turbine and governor models are given by (3.11)-(3.12).

$$\mathrm{d}x_2/\mathrm{d}t = (1/T_{\mathrm{G}})\left(-x_2 + P_{\mathrm{smref}} + (1/D_{\mathrm{psm}})\left(\omega_{\mathrm{smref}} - \omega_{\mathrm{sm}}\right)\right) \tag{3.11}$$

$$\mathrm{d}T_{\mathrm{m}}/\mathrm{d}t = (1/T_{\mathrm{CH}})\left(-T_{\mathrm{m}} + x_2\right) \tag{3.12}$$

The linearized form of (3.11)-(3.12) is given in (3.13) and the corresponding expanded form of matrices are given in Appendix. C.4.3

$$\boldsymbol{\Delta \dot{X}_{\mathbf{GT}}} = \boldsymbol{A_{\mathbf{GTm}}} \boldsymbol{\Delta X_{\mathbf{m}}} + \boldsymbol{A_{\mathbf{GT}}} \boldsymbol{\Delta X_{\mathbf{GT}}} + \boldsymbol{A_{\mathbf{GTE}}} \boldsymbol{\Delta X_{\mathbf{E}}} + \boldsymbol{A_{\mathbf{GTN}}} \boldsymbol{\Delta X_{\mathbf{N}}} + \boldsymbol{A_{\mathbf{GTL}}} \boldsymbol{\Delta X_{\mathbf{L}}} + \boldsymbol{B_{\mathbf{GT}}} \boldsymbol{\Delta U_{\mathbf{sm}}} \tag{3.13}$$

3.3.4 Exciter system

The dynamics of the AC4A exciter model are represented using (3.14)-(3.16).

$$\mathrm{d}v_{\mathrm{smf}}/\mathrm{d}t = (1/T_{\mathrm{r}})\,(-v_{\mathrm{smf}} + (e_{\mathrm{d}}^2 + e_{\mathrm{q}}^2)^{\frac{1}{2}}) \tag{3.14}$$

$$\mathrm{d}x_3/\mathrm{d}t = (1/T_{\mathrm{B}})\,(-x_3 + v_{\mathrm{smref}} - v_{\mathrm{smf}}) \tag{3.15}$$

$$\mathrm{d}E_{\mathrm{fd}}/\mathrm{d}t = (1/T_{\mathrm{A}}T_{\mathrm{B}})(-T_{\mathrm{B}}E_{\mathrm{fd}} + K_{\mathrm{A}}((T_{\mathrm{B}} - T_{\mathrm{C}})x_3 + T_{\mathrm{C}}(v_{\mathrm{smref}} - v_{\mathrm{smf}}))) \tag{3.16}$$

Linearization of (3.14)-(3.16) results in (3.17) of which the expanded form of matrices is given in Appendix C.4.4.

$$\boldsymbol{\Delta\dot{X}_{\mathbf{E}}} = \boldsymbol{A_{\mathbf{Em}}\Delta X_{\mathbf{m}}} + \boldsymbol{A_{\mathbf{EGT}}\Delta X_{\mathbf{GT}}} + \boldsymbol{A_{\mathbf{E}}\Delta X_{\mathbf{E}}} + \boldsymbol{A_{\mathbf{EN}}\Delta X_{\mathbf{N}}} + \boldsymbol{A_{\mathbf{EL}}\Delta X_{\mathbf{L}}} + \boldsymbol{B_{\mathbf{E}}\Delta U_{\mathbf{sm}}} \tag{3.17}$$

3.3.5 Network

The dynamics equations set (2.28)-(2.31) in section 2.2.4 are linearized in synchronous machine's reference frame and given in (3.18).

$$\boldsymbol{\Delta\dot{X}_{\mathbf{N}}} = \boldsymbol{A_{\mathbf{Nd}}\Delta X_{\mathbf{N}}} + \boldsymbol{B_{\mathbf{Nd1}}}\Delta\omega_{\mathrm{sm}} + \boldsymbol{B_{\mathbf{Nd2}}}\begin{bmatrix}\Delta i_{\mathrm{d}}\\ \Delta i_{\mathrm{q}}\end{bmatrix} + \boldsymbol{B_{\mathbf{Nd3}}}(\boldsymbol{B_{\mathbf{Nd4}}}\Delta\delta + \boldsymbol{B_{\mathbf{Nd5}}}\begin{bmatrix}\Delta v_{\mathrm{Ld}}\\ \Delta v_{\mathrm{Lq}}\end{bmatrix}) \tag{3.18}$$

The expanded forms of the matrices in (3.18) are shown in Appendix B.4. Eq.(3.18) can be rearranged as shown in (3.19).

$$\boldsymbol{\Delta\dot{X}_{\mathbf{N}}} = \boldsymbol{A_{\mathbf{N\delta}}}\Delta\delta + \boldsymbol{A_{\mathbf{Nm}}\Delta X_{\mathbf{m}}} + \boldsymbol{A_{\mathbf{NGT}}\Delta X_{\mathbf{GT}}} + \boldsymbol{A_{\mathbf{NE}}\Delta X_{\mathbf{E}}} + \boldsymbol{A_{\mathbf{N}}\Delta X_{\mathbf{N}}} + \boldsymbol{A_{\mathbf{NL}}\Delta X_{\mathbf{L}}} + \boldsymbol{B_{\mathbf{N}}\Delta U_{\mathbf{sm}}} \tag{3.19}$$

The expanded forms of most of the matrices in (3.19) are shown in Appendix B.4 while newly introduced state matrices by the synchronous machine are shown in Appendix C.4.5.

The above state equations are developed in synchronous machine's reference frames. Therefore, the overall state equation for the components in the synchronous machine reference frame is obtained as follows.

$$\boldsymbol{\Delta \dot{X}_{\mathrm{sm}}} = \boldsymbol{A_{\mathrm{sm}\delta}}\Delta\delta + \boldsymbol{A_{\mathrm{sm}}}\boldsymbol{\Delta X_{\mathrm{sm}}} + \boldsymbol{A_{\mathrm{smLoad}}}\boldsymbol{\Delta X_{\mathrm{L}}} + \boldsymbol{B_{\mathrm{sm}}}\boldsymbol{\Delta U_{\mathrm{sm}}} \tag{3.20}$$

Here,

$$\boldsymbol{\Delta X_{\mathrm{sm}}} = \begin{bmatrix} \boldsymbol{\Delta X_{\mathrm{m}}} & \boldsymbol{\Delta X_{\mathrm{GT}}} & \boldsymbol{\Delta X_{\mathrm{E}}} & \boldsymbol{\Delta X_{\mathrm{N}}} \end{bmatrix}^{\mathrm{T}}$$

$$\boldsymbol{A_{\mathrm{sm}\delta}} = \begin{bmatrix} \boldsymbol{0}_{7\times1} & \boldsymbol{0}_{2\times1} & \boldsymbol{0}_{3\times1} & \boldsymbol{A_{\mathrm{N}\delta}} \end{bmatrix}^{\mathrm{T}} \qquad \boldsymbol{A_{\mathrm{sm}}} = \begin{bmatrix} \boldsymbol{A_{\mathrm{m}}} & \boldsymbol{A_{\mathrm{mGT}}} & \boldsymbol{A_{\mathrm{mE}}} & \boldsymbol{A_{\mathrm{PN}}} \\ \boldsymbol{A_{\mathrm{GTm}}} & \boldsymbol{A_{\mathrm{GT}}} & \boldsymbol{A_{\mathrm{GTE}}} & \boldsymbol{A_{\mathrm{GTN}}} \\ \boldsymbol{A_{\mathrm{Em}}} & \boldsymbol{A_{\mathrm{EGT}}} & \boldsymbol{A_{\mathrm{E}}} & \boldsymbol{A_{\mathrm{EN}}} \\ \boldsymbol{A_{\mathrm{Nm}}} & \boldsymbol{A_{\mathrm{NGT}}} & \boldsymbol{A_{\mathrm{NE}}} & \boldsymbol{A_{\mathrm{N}}} \end{bmatrix}$$

$$\boldsymbol{A_{\mathrm{smLoad}}} = \begin{bmatrix} \boldsymbol{A_{\mathrm{mL}}} & \boldsymbol{A_{\mathrm{GTL}}} & \boldsymbol{A_{\mathrm{EL}}} & \boldsymbol{A_{\mathrm{NL}}} \end{bmatrix}^{\mathrm{T}} \quad \boldsymbol{B_{\mathrm{sm}}} = \begin{bmatrix} \boldsymbol{B_{\mathrm{m}}} & \boldsymbol{B_{\mathrm{GT}}} & \boldsymbol{B_{\mathrm{E}}} & \boldsymbol{B_{\mathrm{N}}} \end{bmatrix}^{\mathrm{T}}$$

3.3.6 Load

The dynamic equations set in (2.35)-(2.38) and their linearised representation in (2.39) are valid for the load model in this test system as well. Eq.(2.39) is rearranged for GFM inverter parallel with synchronous machine test configuration as shown in (3.21).

$$\boldsymbol{\Delta \dot{X}_{\mathrm{L}}} = \boldsymbol{A_{\mathrm{Load}\delta}}\Delta\delta + \boldsymbol{A_{\mathrm{Loadgfm}}}\boldsymbol{\Delta X_{\mathrm{gfm}}} + \boldsymbol{A_{\mathrm{Loadsm}}}\boldsymbol{\Delta X_{\mathrm{sm}}} + \boldsymbol{A_{\mathrm{Load}}}\boldsymbol{\Delta X_{\mathrm{L}}} + \boldsymbol{B_{\mathrm{Load}}}\boldsymbol{\Delta U_{\mathrm{L}}} \tag{3.21}$$

Except $\boldsymbol{A_{\mathrm{Loadsm}}}$, the expanded form of other state matrices are given in Appendix B.5. Since load is modeled in GFM inverter's reference frame $\boldsymbol{A_{\mathrm{Loadgfm}}}$ is equivalent to $\boldsymbol{A_{\mathrm{Loadgfm_1}}}$ in Appendix B.5. The expanded form of $\boldsymbol{A_{\mathrm{Loadsm}}}$ is given in Appendix C.4.6.

3.3.7 Overall system

The small signal model for the entire system can be obtained by combining the linearized equations of the sub-components above as shown in (3.22).

$$\boldsymbol{\Delta \dot{X}} = \boldsymbol{A \Delta X} + \boldsymbol{B \Delta U} \tag{3.22}$$

Here

$$\boldsymbol{\Delta X} = \begin{bmatrix} \boldsymbol{\Delta \delta} & \boldsymbol{\Delta X_{\mathbf{gfm}}} & \boldsymbol{\Delta X_{\mathbf{sm}}} & \boldsymbol{\Delta X_{\mathbf{L}}} \end{bmatrix}^{\mathrm{T}} \qquad \boldsymbol{\Delta U} = \begin{bmatrix} \boldsymbol{\Delta U_{\mathbf{gfm}}} & \boldsymbol{\Delta U_{\mathbf{sm}}} & \boldsymbol{\Delta R_{\mathbf{L}}} \end{bmatrix}^{\mathrm{T}}$$

$$\boldsymbol{A} = \begin{bmatrix} A_{\delta} & \boldsymbol{A_{\delta \mathbf{gfm}}} & \boldsymbol{A_{\delta \mathbf{sm}}} & \boldsymbol{0}_{1\times 4} \\ \boldsymbol{A_{\mathbf{gfm}\delta}} & \boldsymbol{A_{\mathbf{gfm}}} & \boldsymbol{0}_{17\times 16} & \boldsymbol{A_{\mathbf{gfmLoad}}} \\ \boldsymbol{A_{\mathbf{sm}\delta}} & \boldsymbol{0}_{16\times 17} & \boldsymbol{A_{\mathbf{sm}}} & \boldsymbol{A_{\mathbf{smLoad}}} \\ \boldsymbol{A_{\mathbf{Load}\delta}} & \boldsymbol{A_{\mathbf{Loadgfm}}} & \boldsymbol{A_{\mathbf{Loadsm}}} & \boldsymbol{A_{\mathbf{Load}}} \end{bmatrix} \qquad \boldsymbol{B} = \begin{bmatrix} \boldsymbol{0}_{1\times 4} & \boldsymbol{0}_{1\times 2} & \boldsymbol{0}_{1\times 1} \\ \boldsymbol{B_{\mathbf{gfm}}} & \boldsymbol{0}_{17\times 2} & \boldsymbol{0}_{1\times 1} \\ \boldsymbol{0}_{16\times 4} & \boldsymbol{B_{\mathbf{sm}}} & \boldsymbol{0}_{1\times 1} \\ \boldsymbol{0}_{4\times 4} & \boldsymbol{0}_{4\times 2} & \boldsymbol{B_{\mathbf{Load}}} \end{bmatrix}$$

3.3.8 Small-signal model validation

To validate the developed small-signal model against a detailed electromagnetic transient (EMT) model in PSCAD/EMTDC, the time-domain responses are obtained from the linearized model and the detailed EMT model to a 10% decrement of load resistance at $t = 15$ s and 2.5% increment of increment of load resistance at $t = 20$ s, 1% impulse of voltage reference of exciter for 0.1 s at $t = 15$ s and 5% increment of GFM inverter's active power reference at $t = 15$ s and given in Figs. 3.3(a), 3.3(b), and 3.3(c), respectively. These tests and others (not shown for brevity) verify the developed small-signal model's ability to track the EMT model's low-frequency content for adequately small disturbances around an operating point.

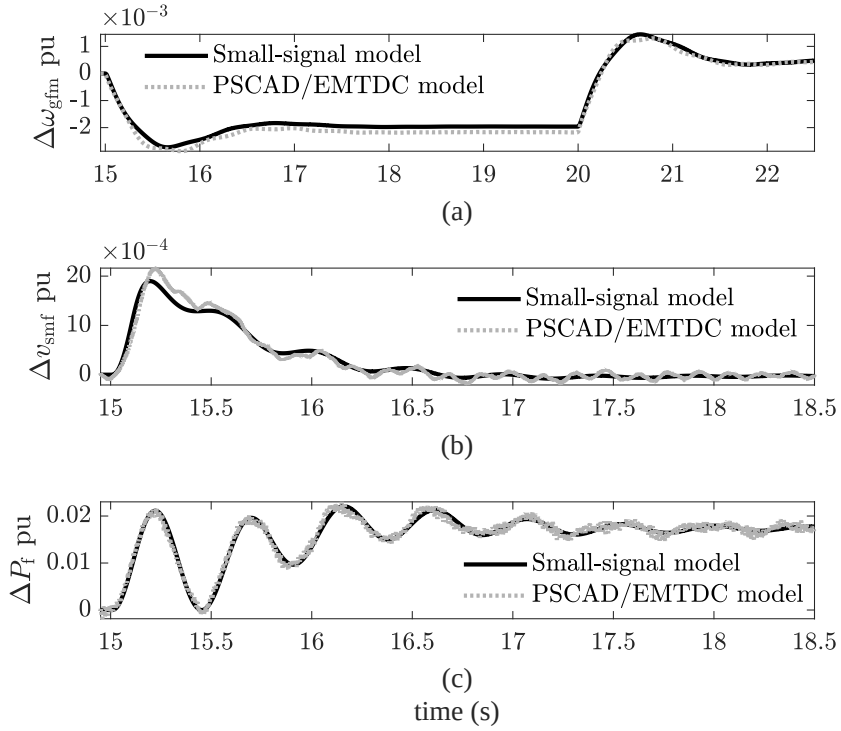

Fig. 3.3: Small-signal vs EMT response for (a) $\Delta R_{\mathrm{L}} = -10\%$ at t = 15 s and $\Delta R_{\mathrm{L}} = 2.5\%$ at t = 20 s, (b) $\Delta v_{\mathrm{smref}_1} = 1\%$ at t = 15 s for 0.1 s and (c) $\Delta P_{\mathrm{gfmref}} = 5\%$ at t = 15 s.

3.4 Eigenvalue Analysis

Eigenvalue analysis of the linearized (small signal) model reveals critical modes at 2.2 Hz and 0.4 Hz. Table 3.2 summarizes the characteristics of these critical modes as well as the state variables that significantly participate in them.

Table 3.2: Major Participants in the Critical Modes

Mode	**Freq** (Hz)	$\boldsymbol{\zeta}$ (%)	**Major participants**
1	2.2	7.7	δ[100%], ω_{sm}[59%], ω_{gfm}[40%], i_{cvd} [23%], i_{cvdhp} [22%]
2	0.4	51.9	T_{m} [100%], x_2 [74%], ω_{gfm} [53%], ω_{sm} [48%], x_1 [37%], i_{cvq} [32%], i_{cvqhp} [32%]

Mode 1 has significant participation from states that govern the electromechanical characteristics of the synchronous machine and the emulated electromechanical characteristics of the GFM inverter. Therefore, mode 1 is identified as a virtual electromechanical mode. Governor and turbine state variables significantly contribute to mode 2. Therefore, mode 2

is identified as a governor mode. Filter inductor current and its high-frequency components have considerable effect on both modes. The dynamics of the Q-v controller has a significant effect on mode 2. Figs. 3.4a and 3.4b give the mode shape diagrams for the critical modes 1 and 2, respectively. Figs. 3.4a shows the interaction between the GFM inverter's and the synchronous machine's rotational speeds. Fig. 3.4b reveals the prominent interaction between the governor-turbine system and the synchronous machine.

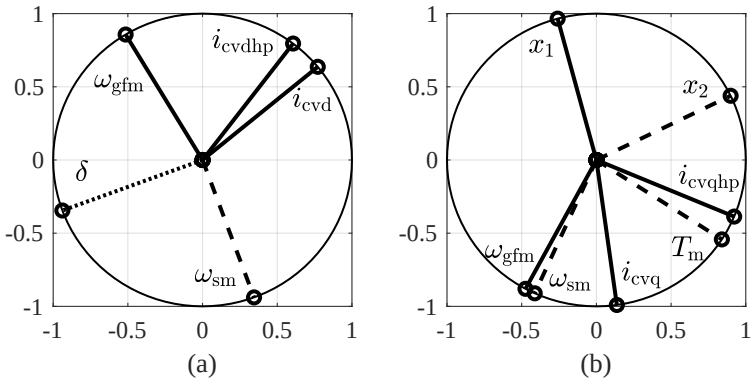

Fig. 3.4: Mode shapes of major participants from GFM inverter (solid line), synchronous machine (dashed line) and both (dotted line) for (a) mode 1 and (b) mode 2.

Following the participation factor analysis the below-listed control and network parameters are selected to identify their effect on the critical modes. The effect of GFM inverter penetration level is also studied. The results obtained from eigenvalue analysis are verified using PSCAD/EMTDC results.

- Electromechanical characteristics governing parameters(Inertia time constant and droop-coefficient of each machine).
- Parameters of governor-turbine system (T_{G}, T_{CH}).
- Parameters of the Q-v controller (T_{i})
- Effect of transient VI path (R_{vi0}, L_{vi0}).
- GFM inverter penetration level.

3.4.1 Effect of electromechanical characteristics governing parameters

The emulated electromechanical characteristics of the GFM inverter are mainly governed by the virtual inertia time constant (H_{gfm}) and the virtual droop co-efficient (D_{pgfm}) in the *P-f* controller. Similarly, the inertia time constant (H_{sm}) and *P-f* droop coefficient (D_{psm}) dictate the electromechanical characteristics of the synchronous machine. Additionally, the turbine-governor dynamics of the synchronous machine affect the electromechanical characteristics of the synchronous machine.

Effect of inertia time constant

To analyze the effect of the virtual inertia time constant, its value is changed from 0.5 s to 8 s while keeping the inertia time constant of the synchronous machine constant at 3 s. Next, the inertia time constant of the synchronous machine is changed from 0.5 s to 8 s while keeping the GFM inverter's inertia time constant at 3 s. The synchronous machine's inertia time constant is not variable in real systems. However, this analysis considers scenarios with different synchronous machines of different inertial levels connected to the test system.

The movement of the eigenvalue corresponding to mode 1 with changes in inertia time-constants of each machine is given in Fig.3.5. Although both modes have significant participation from the rotational speed of their respective machine, the effect of inertia time-constants of each machine on mode 2 is less due to its higher damping than mode 1. Therefore, the locus of eigenvalue corresponding to mode 2 is not shown for brevity. As shown in Fig.3.5, the inertia time-constants of each machine affect contrary to mode 1. i.e., high virtual inertia time-constants of the GFM inverter reduce the damping of mode 1 while high inertia time-constants of synchronous machine improve the damping of mode 1.

This opposite behavior can be explained as follows. The synchronous machine has a slow-acting capability due to its sluggish governor-turbine model. In contrast, the GFM inverter is capable of fast action with the instantaneous governor-turbine model adopted in the GFM

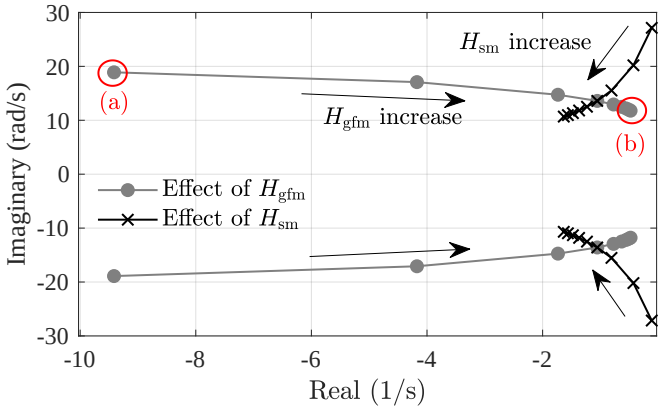

Fig. 3.5: Locus of eigenvalue corresponding to mode 1 for changes of inertia time constants in GFM inverter and synchronous machine.

controller (i.e., explicit, governor-turbine models are not included in the GFM controller). The increment of the virtual inertia time constant slows down the GFM inverter and brings its bandwidth close to that of the synchronous machine. This increases the tendency to interact between these two sources. On the other hand, a large inertia time constant in the synchronous machine makes it slower, leading to a narrower bandwidth compared to the fast-acting GFM inverter. This bandwidth separation discourages interactions.

The participation factor analysis for H_{gfm}= 0.5 s and H_{gfm}= 8 s scenarios (marked with red circles in Fig.3.5) reveals that the participation of ω_{gfm} has reduced from 60% to 21% and the participation of ω_{sm} has increased from 26% to 80% in mode 1 with the increment of the GFM inverter's inertia time-constant. This shows that with large inertia time constants of the GFM inverter, the synchronous machine dynamics govern the system responses. Fig.3.6 gives the time-domain responses obtained from PSCAD/EMTDC for a 5% P_{gfmref} impulse for 0.1 s at t = 15 s. The GFM inverter with a low inertia time constant (Fig.3.6(a)) has well-damped oscillations compared to the GFM inverter with a high inertia time constant (Fig.3.6(b)). This verifies the results obtained from the eigenvalue analysis.

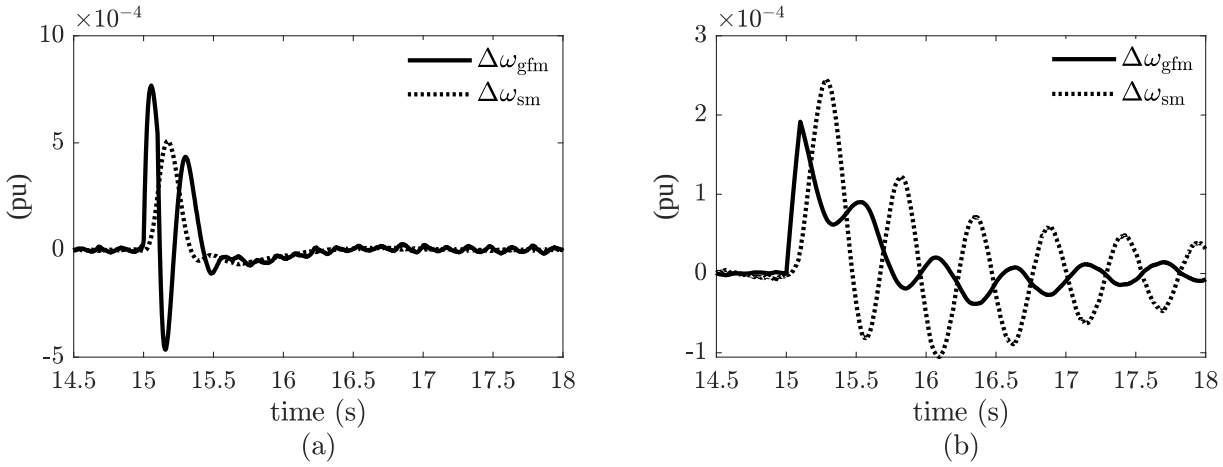

Fig. 3.6: The rotational speed variation for a 5% P_{gfmref_1} impulse at t = 15 s for 0.1 s with $H_{\text{sm}} = 3$ s and (a) $H_{\text{gfm}} = 0.5$ s and (b) $H_{\text{gfm}} = 8$ s.

Effect of *P-f* droop co-efficient

The *P-f* droop coefficient of one of the machines is changed from 0.01 pu to 0.08 pu while keeping the *P-f* droop coefficient of the other machine at 0.03 pu. Fig. 3.7(a), and Fig. 3.7(b) give the movement of eigenvalue corresponding to modes 1 and 2, respectively, with changes in *P-f* droop coefficients of each machine. As shown in Fig.3.7, the *P-f* droop coefficients of each machine type affect both mode 1 and mode 2 conversely; i.e., large *P-f* droop coefficient values of the GFM inverter reduce the stability greatly, while large *P-f* droop coefficient values of synchronous machines slightly improve the stability of the system. Furthermore, a minimal effect on the oscillatory frequency can be observed.

This behavior can be explained similarly to section 3.4.1. The increment of D_{pgfm} increases the time-constant of the *P-f* controller, which is given by $2H_{\text{gfm}}D_{\text{pgfm}}$. Therefore, the bandwidth of the GFM inverter will be close to the bandwidth of the synchronous machine. This increases the machines' tendency to oscillate against each other. On the other hand, the sluggish synchronous machine will be further slowed down with higher *P-f* droop coefficient values (D_{psm}). Therefore, the tendency to interact between the slow-acting synchronous machine and the fast-acting GFM inverter will be reduced, leading to well-damped oscillations. Another perspective for this phenomenon is that a large $P-f$ droop coefficient

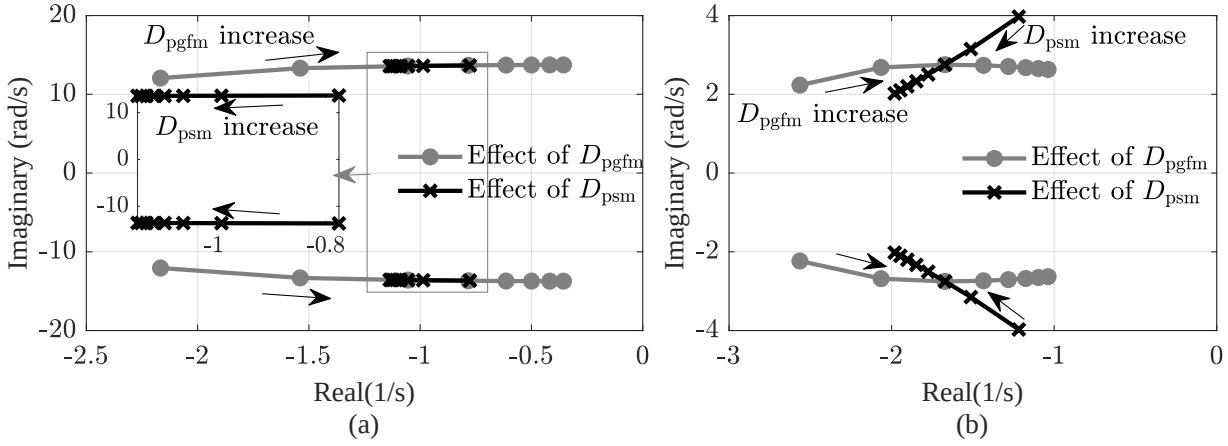

Fig. 3.7: Locus of eigenvalue corresponds to (a) mode 1, and (b) mode 2, for changes in *P-f* droop co-efficient of the GFM inverter and synchronous machine.

of the synchronous machine reduces its contribution allowing the fast-acting GFM inverter to dictate system dynamics and vice versa. This shift of power contribution for a given frequency deviation between the fast-acting and slow-acting machine increases and decreases the damping of the inter-machine interaction, respectively.

Further, the sensitivity of modes to D_{psm} is lower compared to D_{pgfm}. The feedback of the speed deviation is instantly applied in the GFM controller, compared to the prolonged feedback coming via the governor-turbine model of the synchronous machine. This is the reason for the lower sensitivity to D_{psm} compared to the D_{pgfm}.

3.4.2 Effect of governor-turbine system

Though the swing equation and the *P-f* droop characteristic are implemented in both sources, the ultimate effect from these two loops is altered due to the presence of the slow-acting governor and turbine system in the synchronous machine. To validate this argument the following study is conducted.

The inherent delay introduced through a turbine system cannot be changed in real systems. However, this analysis intends to highlight the effect of governor-turbine delays. Therefore, the time constants of the governor and turbine models are changed from 0.001 s

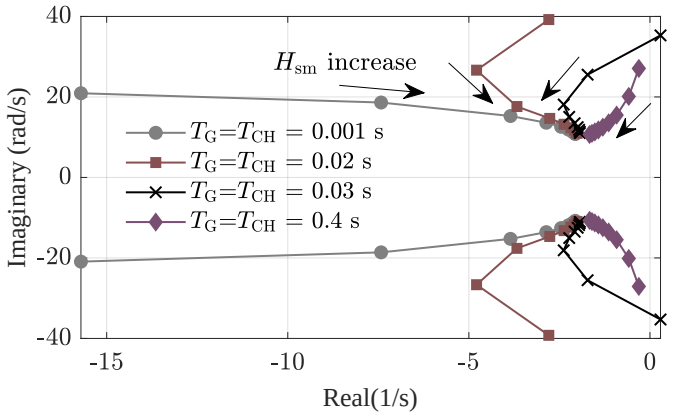

Fig. 3.8: The locus of eigenvalue corresponds to mode 1 with changes in H_{sm} with different governor-turbine dynamics.

to 0.4 s. At each T_G (=T_{CH}) value, the value of the synchronous machine's inertia time constant is changed from 0.5 s to 8 s. The movement of the eigenvalue corresponding to mode 1 is plotted in Fig.3.8. The arrow by each graph shows the direction of the eigenvalue movement with the increment of the synchronous machine's inertia time constant. A governor-turbine system with fast-acting capability moves the eigenvalue corresponding to critical mode, similar to the GFM inverter. This verifies that the slow-acting governor-turbine system alters the response of the synchronous machine and that a fast-acting governor-turbine system can bring the synchronous machine's operating characteristics closer to the fast-acting GFM inverter.

3.4.3 Effect of *Q-v* controller

Due to the significant participation of x_1 in mode 2, the integrator time constant of PI controller in the Q-v controller is changed over [0.025, 0.625] s to identify its effect on the critical modes. The effect on eigenvalues corresponding to modes 1 and 2 are shown in Fig.3.9. The impact of the Q-v controller dynamics on these two critical modes is minimal. However, a significant sensitivity to Q-v controller dynamics is observed with a non-ideal dc-side and detailed discussions are given in Chapter 5.

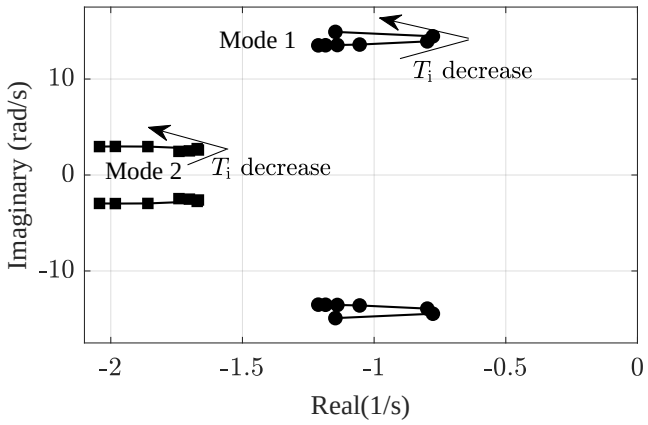

Fig. 3.9: The locus of eigenvalue corresponds to modes 1 and 2 with changes in T_i.

3.4.4 Effect of transient VI path

To analyze the effect of the transient virtual impedance path, values of R_{vi0}, L_{vi0}, X/R ratio, and Z_{vi0} are changed as mentioned in section 2.3.2. The eigenvalue analysis reveals that mode 1 is susceptible to the transient VI path's changes compared to mode 2. The locus of eigenvalue corresponds to mode 1 with changes of transient VI path parameters shown in Fig. 3.10. The arrow by each curve shows the direction of the eigenvalue movement with the increment of the relevant parameter.

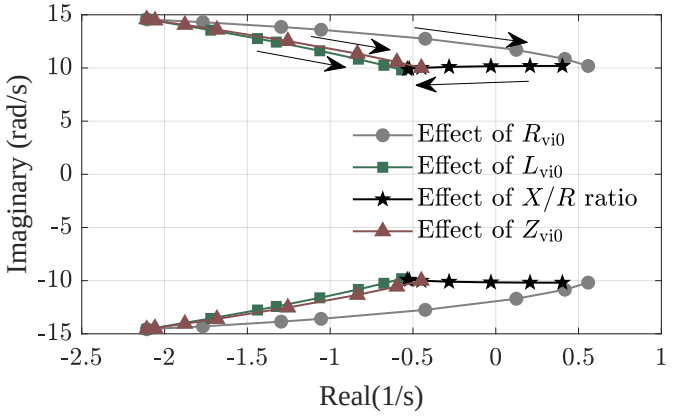

Fig. 3.10: The locus of eigenvalue corresponds to modes 1 with changes in R_{vi0}, L_{vi0}, X/R ratio and Z_{vi0}.

As shown in Fig 3.10, introducing neither the transient virtual resistance nor the transient virtual inductance improves the damping of the virtual electromechanical mode. This

behavior contradicts the improved damping observed in the virtual electromechanical mode of the parallel connected GFM inverters in section 2.3.2 with increased transient virtual inductance. This can be due to the prominence of the sluggish GFM inverter's tendency to interact with the slow-acting synchronous machine over the positive impact provided by the improved decoupling between *P-f* and *Q-v* controller paths with increased transient virtual inductance.

3.4.5 GFM inverter penetration level

The eigenvalue analysis is extended to study the effect of the GFM inverter penetration level. The sizes of each machine, connecting transformers, and the filter elements are set as shown in Table 3.3.

Table 3.3: Network Parameters for Different GFM Inverter Penetration Levels

Parameter	**Value**								
S_{GFM} (MVA)	5	10	15	20	25	30	35	40	45
S_{SM} (MVA)	45	40	35	30	25	20	15	10	5
L_{f} (mH)	10.12	5.06	3.37	2.53	2.02	1.69	1.45	1.26	1.12
C_{f} (μF)	6.96	13.93	20.89	27.86	34.82	41.78	48.75	55.71	62.68
R_{f} (Ω)	8.98	4.49	2.99	2.24	1.79	1.50	1.28	1.12	0.99

The traces of eigenvalue correspond to mode 1 and mode 2 with different GFM inverter penetration levels are given in Fig.3.11. The large penetration of fast-acting GFM inverter has damped both the critical modes.

The detailed time domain rotational speed variations obtained from PSCAD/EMTDC for a 5% impulse given to P_{gfmref} for 0.1 s at t = 15 s are given in Fig. 3.12. Responses for the GFM inverter penetration levels of 10% and 90% (marked in red circles in Fig.3.11) are given in Figs. 3.12a and 3.12b, respectively. Time domain responses verify the ability of the GFM inverter dominant systems to damp inter-machine interactions as predicted by the eigenvalue analysis.

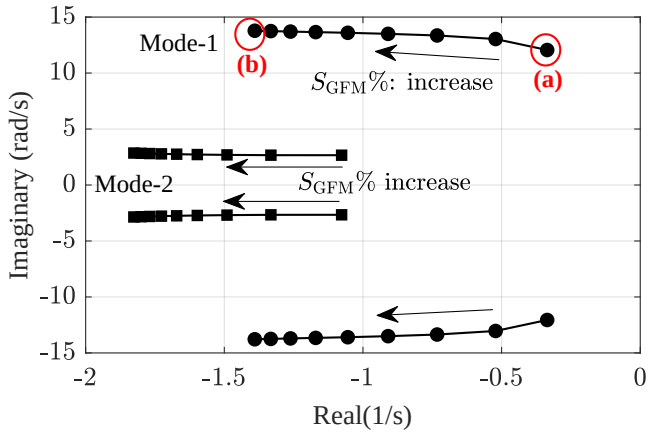

Fig. 3.11: The locus of eigenvalue corresponds to modes 1 and 2 with changes in GFM inverter penetration level.

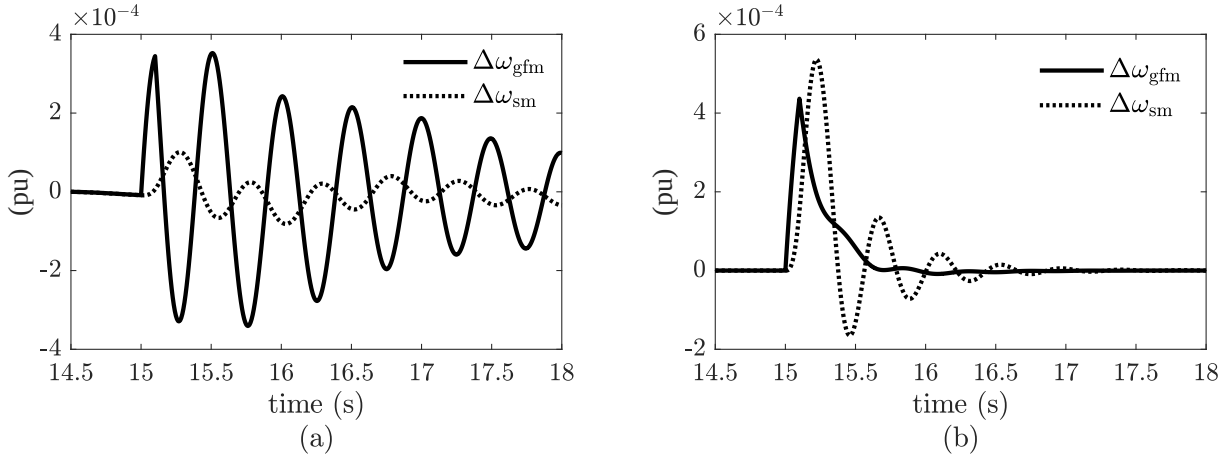

Fig. 3.12: The rotational speed variation for a 5% P_{gfmref_1} impulse at t = 15 s for 0.1 s with (a) S_{GFM}:S_{SM}=10% (b) S_{GFM}:S_{SM}=90%.

3.5 Summary

This chapter analyzed the interactions that may occur between a GFM inverter and a synchronous machine. Eigenvalue analysis revealed a similar inter-machine interaction identified with parallel connected GFM inverters in Chapter 2. Additionally, a well-damped governor mode was identified. The key contributions of the chapter are:

- Development and validation of a small-signal model for the exemplar system of parallel-connected GFM inverter and a synchronous machine by including the full dynamics of the VSM layer, transient virtual impedance path, network, synchronous machine,

governor-turbine system, and exciter.

- Identification of a contrary behavior between the GFM inverter and synchronous machine in affecting the critical modes in the system. The effect of the synchronous machine's governor-turbine system in evoking the contrary behavior was revealed.
- Demonstration of the ability of a GFM controller with a low bandwidth to dominate the power system.

Chapter 4

Effect of Grid-Forming Inverter's Current-Limiting Methods

A GFM inverter must have an explicit current-limiting algorithm to avoid thermal overloading of power electronic switches. Current-limiting methods for GFM inverters are discussed in [2, 22, 24] under different categorizations. The most common categories are the no-loop and multiple-loop current-limiting algorithms. The no-loop category limits the converter's terminal voltage to limit the current output from the converter. This is commonly carried out using a current-dependent virtual impedance [15] or a predefined voltage-current droop relationship [25]. The multi-loop control structure utilizes inner control layers that consist of either only a current-limiting loop [26] or both voltage- and current-limiting loops [27,28].

The multi-loop control structures shift the inverter's operation to a current source during over-currents, while no-loop controllers preserve the voltage source characteristics. This behavior of the multi-loop control structure minimizes the overlap between the pre-fault and during the fault power angle curves, leading to a challenging fault recovery [29]. The reduction of voltage reference generated by $Q - v$ controller via current-dependent virtual impedance [22], decrease in set values of active power and reactive power according to the voltage at the point of common coupling [24], and reduction of current references

proportional to over-current levels [30] have been implemented to retain the voltage source characteristics of the inverter in the multi-loop control structure. Though the majority of controllers focus on balanced faults, there are controllers in the natural reference frame (i.e., *abc* domain) [30], stationary reference frame (i.e. $\alpha\beta$ domain) [31], and synchronous reference frame (i.e., dq domain) [32] that can handle unbalanced faults.

The eigenvalue analysis of the current-dependent virtual impedance-based no-loop control strategy was discussed in Chapter 3 with the parallel connected GFM inverter and synchronous machine-based test system. Using the same test system, eigenvalue analyses are conducted on two of the multi-loop control structures. The virtual admittance-based inner current controller consists of the inner current controller for which the current references are obtained by a virtual admittance [26]. The other multi-loop control structure consists of inner voltage and current controllers, which is referred to as cascaded voltage-current controllers [28].

Section 4.1 discusses the two multi-loop current-limiting methods. The small-signal model developed in Chapter 3 is modified according to the considered current-limiting method, and the steps are included in section 4.2. Eigenvalue analysis for the virtual admittance-based inner current controller and the cascaded voltage-current controller are included in section 4.3. The possibilities of causing interactions due to the current-limiting method are also investigated. Proper current controller parameters are selected following the eigenvalue analysis. Section 4.4 includes detailed PSCAD/EMTDC results to demonstrate the Fault-Ride-Through (FRT) capability of the considered current-limiting methods. The chapter summary is included in section 4.5.

4.1 Current-Limiting Methods

Chapter 3 discussed the virtual-impedance-based current controller. Therefore, this chapter discusses the virtual admittance-based inner current controller method and the cascaded

voltage-current controller.

4.1.1 Virtual admittance-based inner current controller

The high-level representation of the GFM controller with the virtual admittance-based inner current controller is shown in the block diagram given in Fig. 4.1. The *P-f* and *Q-v* controller loops are the same as the controller loops used in Chapter 2. The virtual admittance block and the decoupled current controller are elaborated in Figs. 4.2 and 4.3, respectively. The control parameters in Table 4.1 are used, while keeping the other control and the network parameters at the values given in Chapter 3.

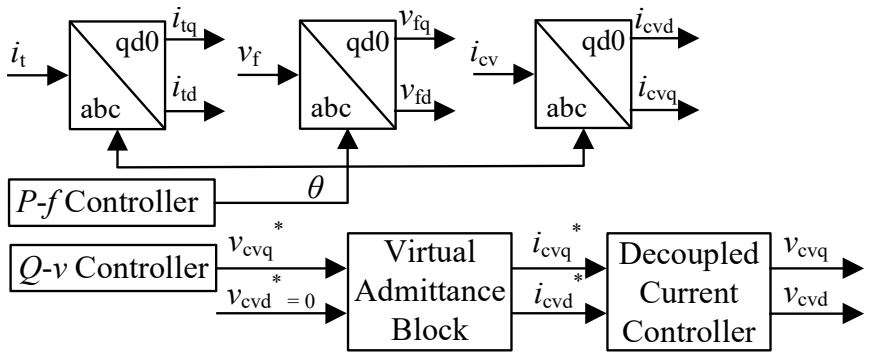

Fig. 4.1: Block diagram representation of GFM controller with virtual admittance based inner current controller.

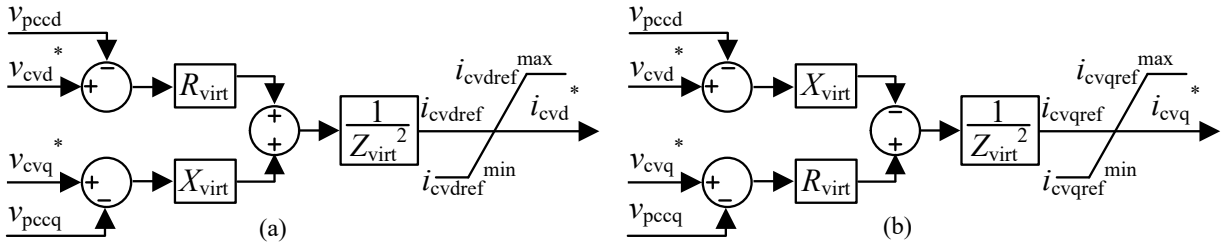

Fig. 4.2: Converter current reference calculation from virtual admittance block for (a) d - axis (b) q - axis.

The converter terminal's expected voltage ($v_{cvq}{}^*$, $v_{cvd}{}^* = 0$) generated by the *Q-v* controller is taken as the input to the virtual admittance block. The virtual admittance block

assumes a series connected virtual resistance and reactance ($R_{\text{virt}} + jX_{\text{virt}}$) between the converter terminal and the point of common coupling (terminal of LC filter). Z_{vrit} is the magnitude of the series virtual impedance. The expected converter terminal current components (i_{cvdref}, i_{cvqref}) are limited according to i_{q} prioritization logic. Using q-axis current limits given in Table 4.1 d-axis maximum and minimum values are calculated as ${i_{\text{cvdref}}}^{\text{max}} = ({i_{\text{cvqref}}}^{\text{max}^2} - {i_{\text{cvqref}}}^2)^{1/2}$ and ${i_{\text{cvdref}}}^{\text{min}} = -{i_{\text{cvdref}}}^{\text{max}}$.

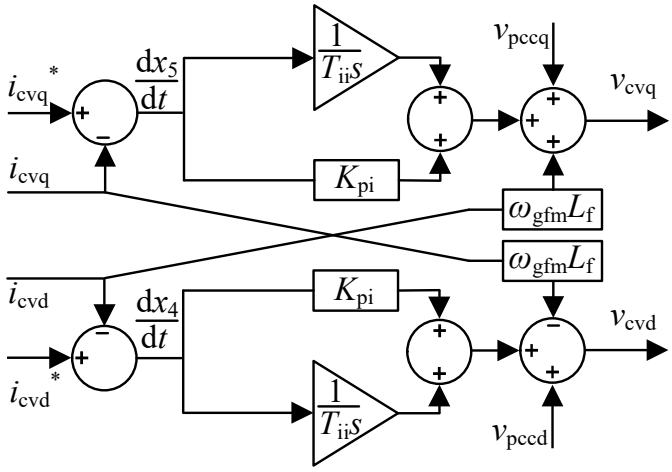

Fig. 4.3: Block diagram representation of decoupled current controller.

As shown in Fig. 4.3, the limited converter terminal current references (${i_{\text{cvd}}}^*$, ${i_{\text{cvq}}}^*$) are compared with the instantaneous converter terminal current components (i_{cvd}, i_{cvq}) and the error signals are passed through the conventional decoupled current controller. The decoupled current controller issues the converter terminal voltage commands (v_{cvd} and v_{cvq}).

Table 4.1: Control Parameters for Virtual Admittance based Inner Current Controller

Virtual admittance block	**Decoupled current controller**
$X_{\text{virt}} = 1$, $R_{\text{virt}} = 0$ ${i_{\text{cvqref}}}^{\text{max}} = 1.1$ pu, ${i_{\text{cvqref}}}^{\text{min}} = $ -1.1 pu	$K_{\text{pi}} = 0.1$, $T_{\text{ii}} = 0.05$ s

4.1.2 Cascaded voltage-current controller

Figure 4.4 gives the high-level representation of the GFM controller with the cascaded voltage-current controller. The *P-f* and *Q-v* controller loops are identical to the corresponding controller loops used in Chapter 2. The decoupled current controller is the same as in Fig. 4.3. Compared to the previously mentioned current-limiting methods, the output of the *Q-v* controller is the expected voltage at the filter capacitor instead of the converter terminal voltage. This voltage reference is then passed through a voltage controller that is developed based on the voltage drop across the filter capacitor. The block diagram of the decoupled voltage controller is given in Fig. 4.5. The control parameters shown in Table 4.2 are used together with the other relevant control and network parameters given in Chapter 3. These control parameter values are selected through a genetic algorithm-based optimizer in PSCAD/EMTDC.

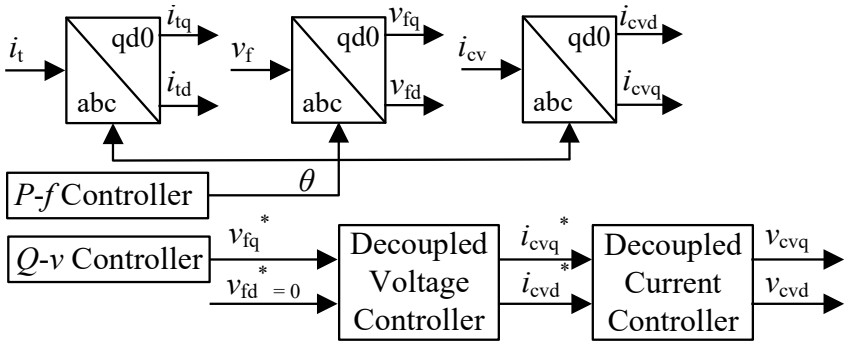

Fig. 4.4: Block diagram representation of GFM controller with cascaded voltage - current controller.

Table 4.2: Control Parameters for Cascaded Voltage-Current Controller

***Q-v* controller**	**Decoupled voltage controller**	**Decoupled current controller**
$K_p = 0.998$, $T_i = 0.284$ s	$K_{pv} = 0.969$, $K_{av} = 2$ $T_{iv} = 0.374$ s	$K_{pi} = 0.430$, $T_{ii} = 0.241$ s

The decoupled voltage controller outputs the converter terminal current commands (i_{cvdref}, i_{cvqref}). Those current commands are limited according to the i_q prioritization logic explained in section 4.1.1

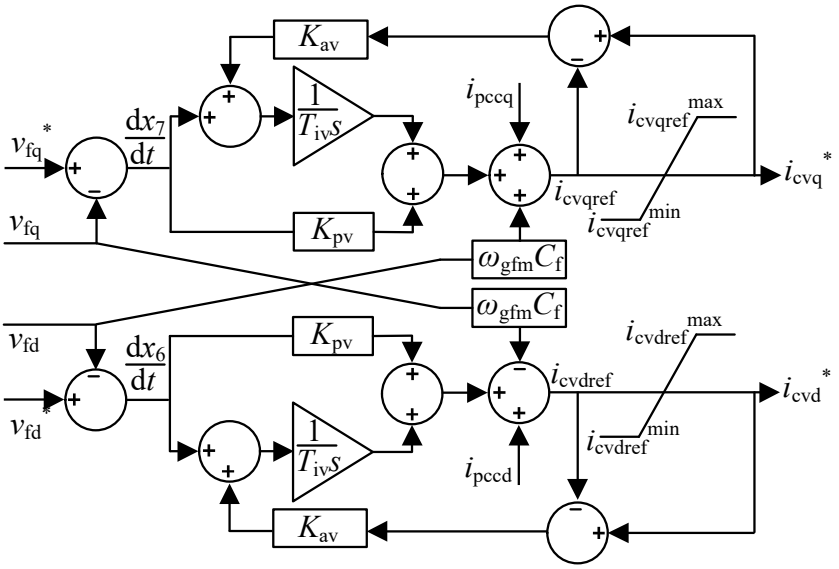

Fig. 4.5: Block diagram representation of decoupled voltage controller.

4.2 Small-Signal Model Development

The details related to the small-signal model derivation of *P-f* controller, *Q-v* controller, network, and synchronous machine have already been discussed in Chapters 2 and 3. The high-frequency converter current components (i_{cvdhp}, i_{cvqhp}) exclusively belonging to the transient virtual impedance path will not apply to the virtual admittance-based inner current controller and the cascaded voltage-current controller. Therefore, the linearized model of the *LC* filter and the transformer will be represented using the states given in (4.1).

$$\boldsymbol{\Delta X_{\mathbf{LCL}}} = \begin{bmatrix} \Delta i_{\text{cvd}} & \Delta i_{\text{cvq}} & \Delta v_{\text{fd}} & \Delta v_{\text{fq}} & \Delta i_{\text{td}} & \Delta i_{\text{tq}} \end{bmatrix}^{\text{T}} \tag{4.1}$$

New states will be added according to the current controlling strategy. The virtual admittance-based inner current controller introduces two states represented by $\boldsymbol{\Delta X_{\mathbf{CC}}} = \begin{bmatrix} \Delta x_4 & \Delta x_5 \end{bmatrix}^{\text{T}}$. On top of these two states the cascaded voltage-current controller introduces two additional states represented by $\boldsymbol{\Delta X_{\mathbf{VC}}} = \begin{bmatrix} \Delta x_6 & \Delta x_7 \end{bmatrix}^{\text{T}}$. Those relevant modifications will be discussed for the virtual admittance-based inner current controller and cascaded voltage and current controller in sections 4.2.1 and 4.2.2, respectively.

4.2.1 Virtual admittance-based inner current controller

Power controller

The small-signal model derivation of this component is similar to section 2.2.2. The linearized representation of the power controller corresponding to the virtual admittance-based inner current controller embedded GFM controller is given in (4.2).

$$\boldsymbol{\Delta \dot{X}_P} = \boldsymbol{A_P \Delta X_P} + \boldsymbol{A_{PCC} \Delta X_{CC}} + \boldsymbol{A_{PLCL} \Delta X_{LCL}} + \boldsymbol{A_{PN} \Delta X_N} + \boldsymbol{A_{PL} \Delta X_L} + \boldsymbol{B_P \Delta U_{gfm}} \tag{4.2}$$

The expanded form of matrices in (4.2) are similar to expanded matrices given in Appendix B.2, except, $\boldsymbol{A_{PCC}}$ and $\boldsymbol{A_{PLCL}}$ that are shown in Appendix D.1.

Virtual admittance block

In developing the small-signal model, it is assumed that the dq components of the converter current are below the limits. Therefore, the virtual admittance block output can be represented as in (4.3)-(4.4). Here, v_{td} and v_{tq} are the the output of the Q-v controller concerning the high voltage side of the connecting transformer

$$i_{\mathrm{cvd}}{}^{*} = \frac{R_{\mathrm{virt}}}{R_{\mathrm{virt}}{}^{2} + X_{\mathrm{virt}}{}^{2}}(v_{\mathrm{td}} - v_{\mathrm{pccd}}) + \frac{X_{\mathrm{virt}}}{R_{\mathrm{virt}}{}^{2} + X_{\mathrm{virt}}{}^{2}}(v_{\mathrm{tq}} - v_{\mathrm{pccq}}) \tag{4.3}$$

$$i_{\mathrm{cvq}}{}^{*} = -\frac{X_{\mathrm{virt}}}{R_{\mathrm{virt}}{}^{2} + X_{\mathrm{virt}}{}^{2}}(v_{\mathrm{td}} - v_{\mathrm{pccd}}) + \frac{R_{\mathrm{virt}}}{R_{\mathrm{virt}}{}^{2} + X_{\mathrm{virt}}{}^{2}}(v_{\mathrm{tq}} - v_{\mathrm{pccq}}) \tag{4.4}$$

The linearized representation of (4.3)-(4.4) is given in (4.5). The expanded form of the relevant matrices is given in Appendix D.2.

$$\begin{bmatrix} \Delta i_{\mathrm{cvd}}{}^{*} & \Delta i_{\mathrm{cvq}}{}^{*} \end{bmatrix}^{\mathrm{T}} = \boldsymbol{A_{icvdqrefP} \Delta X_P} + \boldsymbol{A_{icvdqrefLCL} \Delta X_{LCL}} + \boldsymbol{B_{icvdqref} \Delta U_{gfm}} \tag{4.5}$$

Decoupled current controller

The set of non-linear equations that govern the dynamics of the decoupled current controller is given in (4.6)-(4.7).

$$\mathrm{d}x_4/\mathrm{d}t = {i_{\mathrm{cvd}}}^* - i_{\mathrm{cvd}} \tag{4.6}$$

$$\mathrm{d}x_5/\mathrm{d}t = {i_{\mathrm{cvq}}}^* - i_{\mathrm{cvq}} \tag{4.7}$$

Linearizing (4.6)-(4.7) and substitution of (4.5) yields (4.8). The expanded form of the relevant matrices is given in Appendix D.3.

$$\boldsymbol{\Delta \dot{X}_{CC}} = \boldsymbol{A_{CCP}\Delta X_P} + \boldsymbol{A_{CC}\Delta X_{CC}} + \boldsymbol{A_{CCLCL}\Delta X_{LCL}} + \boldsymbol{A_{CCN}\Delta X_N} + \boldsymbol{A_{CCL}\Delta X_L} + \boldsymbol{B_{CC}\Delta U_{gfm}} \tag{4.8}$$

LC filter and transformer

The dq-domain non-linear equations that govern the dynamics of the LC filter and the transformer are similar to the equations in (2.15)-(2.20). The linearized representation of this component in the virtual admittance-based inner current controller embedded scenario is given in (4.9). The expanded form of the relevant matrices is given in Appendix D.4.

$$\boldsymbol{\Delta \dot{X}_{LCL}} = \boldsymbol{A_{LCLP}\Delta X_P} + \boldsymbol{A_{LCLCC}\Delta X_{CC}} + \boldsymbol{A_{LCL}\Delta X_{LCL}} + \boldsymbol{A_{LCLN}\Delta X_N} + \boldsymbol{A_{LCLL}\Delta X_L} + \boldsymbol{B_{LCL}\Delta U_{gfm}} \tag{4.9}$$

Network

The small-signal model derivation of this component is similar to Section 2.2.4. The corresponding linearized representation with the virtual admittance-based inner current controller

is given in (4.10).

$$\boldsymbol{\Delta \dot{X}_{N}} = \boldsymbol{A_{NP}\Delta X_{P}} + \boldsymbol{A_{NCC}\Delta X_{CC}} + \boldsymbol{A_{NLCL}\Delta X_{LCL}} + \boldsymbol{A_{N}\Delta X_{N}} + \boldsymbol{A_{NL}\Delta X_{L}} + \boldsymbol{B_{N}\Delta U_{gfm}} \tag{4.10}$$

The expanded form of matrices in (4.10) are similar to expanded matrices given in Appendix B.4, except, $\boldsymbol{A_{NCC}}$ and $\boldsymbol{A_{NLCL}}$ that are shown in Appendix D.5.

The overall state equation for the components above in the GFM inverter's reference frame can be represented as shown in (4.11).

$$\boldsymbol{\Delta \dot{X}_{gfm}} = \boldsymbol{A_{gfm}\Delta X_{gfm}} + \boldsymbol{A_{gfmsm}\Delta X_{sm}} + \boldsymbol{A_{gfmLoad}\Delta X_{L}} + \boldsymbol{B_{gfm}\Delta U_{gfm}} \tag{4.11}$$

Here,

$$\boldsymbol{\Delta X_{gfm}} = \begin{bmatrix} \boldsymbol{\Delta X_{P}} & \boldsymbol{\Delta X_{CC}} & \boldsymbol{\Delta X_{LCL}} & \boldsymbol{\Delta X_{N}} \end{bmatrix}^{T}$$

$$\boldsymbol{A_{gfm}} = \begin{bmatrix} \boldsymbol{A_{P}} & \boldsymbol{A_{PCC}} & \boldsymbol{A_{PLCL}} & \boldsymbol{A_{PN}} \\ \boldsymbol{A_{CCP}} & \boldsymbol{A_{CC}} & \boldsymbol{A_{CCLCL}} & \boldsymbol{A_{CCN}} \\ \boldsymbol{A_{LCLP}} & \boldsymbol{A_{LCLCC}} & \boldsymbol{A_{LCL}} & \boldsymbol{A_{LCLN}} \\ \boldsymbol{A_{NP}} & \boldsymbol{A_{NCC}} & \boldsymbol{A_{NLCL}} & \boldsymbol{A_{N}} \end{bmatrix}$$

$$\boldsymbol{A_{gfmLoad}} = \begin{bmatrix} \boldsymbol{A_{PL}} & \boldsymbol{A_{CCL}} & \boldsymbol{A_{LCLL}} & \boldsymbol{A_{NL}} \end{bmatrix}^{T}$$

$$\boldsymbol{B_{gfm}} = \begin{bmatrix} \boldsymbol{B_{P}} & \boldsymbol{B_{CC}} & \boldsymbol{B_{LCL}} & \boldsymbol{B_{N}} \end{bmatrix}^{T}$$

$$\boldsymbol{A_{gfmsm}} = \boldsymbol{0}_{17\times 16}$$

The linearization of the synchronous machine and the load components in section 3.3 will be intact in the presence of the virtual admittance-based inner current controller. Therefore, the overall system's state matrix can be obtained similarly to section 3.3.7.

4.2.2 Cascaded voltage-current controller

Power controller

The small-signal model derivation of this component is similar to section 2.2.2. The linearized representation of the power controller corresponding to the cascaded voltage-current controller embedded GFM controller is given in (4.12).

$$\boldsymbol{\Delta \dot{X}_P} = \boldsymbol{A_P \Delta X_P} + \boldsymbol{A_{PVC} \Delta X_{VC}} + \boldsymbol{A_{PCC} \Delta X_{CC}} + \boldsymbol{A_{PLCL} \Delta X_{LCL}} + \boldsymbol{A_{PN} \Delta X_N} + \boldsymbol{A_{PL} \Delta X_L} + \boldsymbol{B_P \Delta U_{gfm}} \quad (4.12)$$

The expanded form of matrices in (4.12) are similar to expanded matrices given in Appendix B.2 and Appendix D.1. Here, $\boldsymbol{A_{PVC}} = \boldsymbol{0}_{5\times 2}$.

Decoupled voltage controller

The input to the decoupled voltage controller block is the output of the Q-v controller referred to the high voltage side of the transformer, which is given in (4.13)- (4.14).

$$v_{\mathrm{fd}}{}^{*} = \sin(-30^{\circ})(-K_{\mathrm{p}}(D_{\mathrm{q}}(Q_{\mathrm{ref}} - Q_{\mathrm{f}}) + E_{\mathrm{ref}} - E_{\mathrm{f}}) - x_1/T_{\mathrm{i}}) \quad (4.13)$$

$$v_{\mathrm{fq}}{}^{*} = \cos(-30^{\circ})(-K_{\mathrm{p}}(D_{\mathrm{q}}(Q_{\mathrm{ref}} - Q_{\mathrm{f}}) + E_{\mathrm{ref}} - E_{\mathrm{f}}) - x_1/T_{\mathrm{i}}) \quad (4.14)$$

The linearization of (4.13)-(4.14) results in (4.15).

$$\begin{bmatrix} \Delta v_{\mathrm{fd}}{}^{*} \\ \Delta v_{\mathrm{fq}}{}^{*} \end{bmatrix} = \begin{bmatrix} \sin(-30^{\circ}) \\ \cos(-30^{\circ}) \end{bmatrix} \boldsymbol{C_E \Delta X_P} + \begin{bmatrix} \sin(-30^{\circ}) \\ \cos(-30^{\circ}) \end{bmatrix} \boldsymbol{D_E \Delta U_{gfm}} \quad (4.15)$$

The expanded form of matrices in (4.15) are similar to the matrices given in Appendix B.2. The set of non-linear equations that govern the dynamics of the decoupled voltage controller

is given in (4.16)-(4.17).

$$\mathrm{d}x_6/\mathrm{d}t = {v_{\mathrm{fd}}}^* - v_{\mathrm{fd}} \tag{4.16}$$

$$\mathrm{d}x_7/\mathrm{d}t = {v_{\mathrm{fq}}}^* - v_{\mathrm{fq}} \tag{4.17}$$

Linearizing (4.16)-(4.17) and substituting (4.15) yeilds (4.18).

$$\boldsymbol{\Delta \dot{X}_{VC}} = \boldsymbol{A_{VCP}\Delta X_P} + \boldsymbol{A_{VC}\Delta X_{VC}} + \boldsymbol{A_{VCCC}\Delta X_{CC}} + \boldsymbol{A_{VCLCL}\Delta X_{LCL}} + \boldsymbol{A_{VCN}\Delta X_N} + \boldsymbol{A_{VCL}\Delta X_L} + \boldsymbol{B_{VC}\Delta U_{gfm}} \tag{4.18}$$

The expanded form of matrices is in Appendix E.1.

Decoupled current controller

The input to the decoupled current controller is the output from the decoupled voltage controller given in (4.19)-(4.20).

$${i_{\mathrm{cvd}}}^* = K_{\mathrm{pv}}({v_{\mathrm{fd}}}^* - v_{\mathrm{fd}}) + (1/T_{\mathrm{iv}})x_6 + i_{\mathrm{td}} - \omega C_{\mathrm{f}} v_{\mathrm{fq}} \tag{4.19}$$

$${i_{\mathrm{cvq}}}^* = K_{\mathrm{pv}}({v_{\mathrm{fq}}}^* - v_{\mathrm{fq}}) + (1/T_{\mathrm{iv}})x_7 + i_{\mathrm{tq}} + \omega C_{\mathrm{f}} v_{\mathrm{fd}} \tag{4.20}$$

The linearization of (4.19)-(4.20) and substitution of (4.15) results in (4.21).

$$\begin{bmatrix} \Delta {i_{\mathrm{cvd}}}^* \\ \Delta {i_{\mathrm{cvq}}}^* \end{bmatrix} = \boldsymbol{A_{icvdqrefP}\Delta X_P} + \boldsymbol{A_{icvdqrefVC}\Delta X_{VC}} + \boldsymbol{A_{icvdqrefLCL}\Delta X_{LCL}} + \boldsymbol{B_{icvdqref}\Delta U_{gfm}} \tag{4.21}$$

The dynamics of the decoupled current controller can be represented similarly to (4.6)-(4.7). The lineaization of (4.6)-(4.7) and substitution of (4.21) results in (4.22). The expanded

form of the matrices is given in Appendix E.2.

$$\boldsymbol{\Delta \dot{X}_{CC}} = \boldsymbol{A_{CCP}\Delta X_P} + \boldsymbol{A_{CCVC}\Delta X_{VC}} + \boldsymbol{A_{CC}\Delta X_{CC}} + \boldsymbol{A_{CCLCL}\Delta X_{LCL}} + \boldsymbol{A_{CCN}\Delta X_N} + \boldsymbol{A_{CCL}\Delta X_L} + \boldsymbol{B_{CC}\Delta U_{gfm}} \quad (4.22)$$

LC filter and transformer

The small-signal model derivation of this component is similar to section 4.2.1. The linearized representation of this component in the cascaded voltage-current controller embedded scenario is given in (4.23). The expanded form of the relevant matrices is shown in Appendix E.3.

$$\boldsymbol{\Delta \dot{X}_{LCL}} = \boldsymbol{A_{LCLP}\Delta X_P} + \boldsymbol{A_{LCLVC}\Delta X_{VC}} + \boldsymbol{A_{LCLCC}\Delta X_{CC}} + \boldsymbol{A_{LCL}\Delta X_{LCL}} + \boldsymbol{A_{LCLN}\Delta X_N} + \boldsymbol{A_{LCLL}\Delta X_L} + \boldsymbol{B_{LCL}\Delta U_{gfm}} \quad (4.23)$$

Network

The small-signal model derivation of this component is similar to Section 2.2.4. The corresponding linearized representation with the cascaded voltage-current controller is given in (4.24).

$$\boldsymbol{\Delta \dot{X}_N} = \boldsymbol{A_{NP}\Delta X_P} + \boldsymbol{A_{NVC}\Delta X_{VC}} + \boldsymbol{A_{NCC}\Delta X_{CC}} + \boldsymbol{A_{NLCL}\Delta X_{LCL}} + \boldsymbol{A_N\Delta X_N} + \boldsymbol{A_{NL}\Delta X_L} + \boldsymbol{B_N\Delta U_{gfm}} \quad (4.24)$$

The expanded form of matrices in (4.24) are similar to expanded matrices given in Appendix B.4, except, $\boldsymbol{A_{NVC}}$, $\boldsymbol{A_{NCC}}$ and $\boldsymbol{A_{NLCL}}$ that are shown in Appendix E.4.

The overall state equation for the components mentioned above in the GFM inverter's

reference frame can be represented as shown in (4.25).

$$\boldsymbol{\Delta \dot{X}_{gfm}} = \boldsymbol{A_{gfm}} \boldsymbol{\Delta X_{gfm}} + \boldsymbol{A_{gfmsm}} \boldsymbol{\Delta X_{sm}} + \boldsymbol{A_{gfmLoad}} \boldsymbol{\Delta X_{L}} + \boldsymbol{B_{gfm}} \boldsymbol{\Delta U_{gfm}} \tag{4.25}$$

Here,

$$\boldsymbol{\Delta X_{gfm}} = \begin{bmatrix} \boldsymbol{\Delta X_{P}} & \boldsymbol{\Delta X_{VC}} & \boldsymbol{\Delta X_{CC}} & \boldsymbol{\Delta X_{LCL}} & \boldsymbol{\Delta X_{N}} \end{bmatrix}^{T}$$

$$\boldsymbol{A_{gfm}} = \begin{bmatrix} \boldsymbol{A_{P}} & \boldsymbol{A_{PVC}} & \boldsymbol{A_{PCC}} & \boldsymbol{A_{PLCL}} & \boldsymbol{A_{PN}} \\ \boldsymbol{A_{VCP}} & \boldsymbol{A_{VC}} & \boldsymbol{A_{VCCC}} & \boldsymbol{A_{VCLCL}} & \boldsymbol{A_{VCN}} \\ \boldsymbol{A_{CCP}} & \boldsymbol{A_{CCVC}} & \boldsymbol{A_{CC}} & \boldsymbol{A_{CCLCL}} & \boldsymbol{A_{CCN}} \\ \boldsymbol{A_{LCLP}} & \boldsymbol{A_{LCLVC}} & \boldsymbol{A_{LCLCC}} & \boldsymbol{A_{LCL}} & \boldsymbol{A_{LCLN}} \\ \boldsymbol{A_{NP}} & \boldsymbol{A_{NVC}} & \boldsymbol{A_{NCC}} & \boldsymbol{A_{NLCL}} & \boldsymbol{A_{N}} \end{bmatrix}$$

$$\boldsymbol{A_{gfmLoad}} = \begin{bmatrix} \boldsymbol{A_{PL}} & \boldsymbol{A_{VCL}} & \boldsymbol{A_{CCL}} & \boldsymbol{A_{LCLL}} & \boldsymbol{A_{NL}} \end{bmatrix}^{T}$$

$$\boldsymbol{B_{gfm}} = \begin{bmatrix} \boldsymbol{B_{P}} & \boldsymbol{B_{VC}} & \boldsymbol{B_{CC}} & \boldsymbol{B_{LCL}} & \boldsymbol{B_{N}} \end{bmatrix}^{T}$$

$$\boldsymbol{A_{gfmsm}} = \boldsymbol{0}_{19\times 16}$$

The linearization of the synchronous machine and the load components in section 3.3 will be intact in the presence of the cascaded voltage-current controller. Therefore, the overall system's state matrix can be obtained similarly to section 3.3.7.

4.2.3 Small-signal model validation

This section validates the small-signal models developed for the aforementioned current controllers against corresponding detailed EMT models in PSCAD/EMTDC. Figs. 4.6 and 4.7 give the time-domain responses obtained from the linearized model and the detailed EMT model of virtual admittance-based inner current controller embedded GFM inverter and cascaded voltage-current controller embedded GFM inverter systems, respectively. The

following disturbances are applied to obtain the subplot of each graph: (a) $\Delta\omega_{\text{gfmref}} = 1\%$ at t = 15 s for 0.1 s, (b) $\Delta R_{\text{L}} = -10\%$ at t = 15 s and $\Delta R_{\text{L}} = 2.5\%$ at t = 20 s and (c) $\Delta E_{\text{ref}} = 1\%$ at t = 15 s. These tests and others (not shown for brevity) confirm that the developed small-signal models can track the low-frequency oscillation of the EMT model for adequately small disturbances around an operating point.

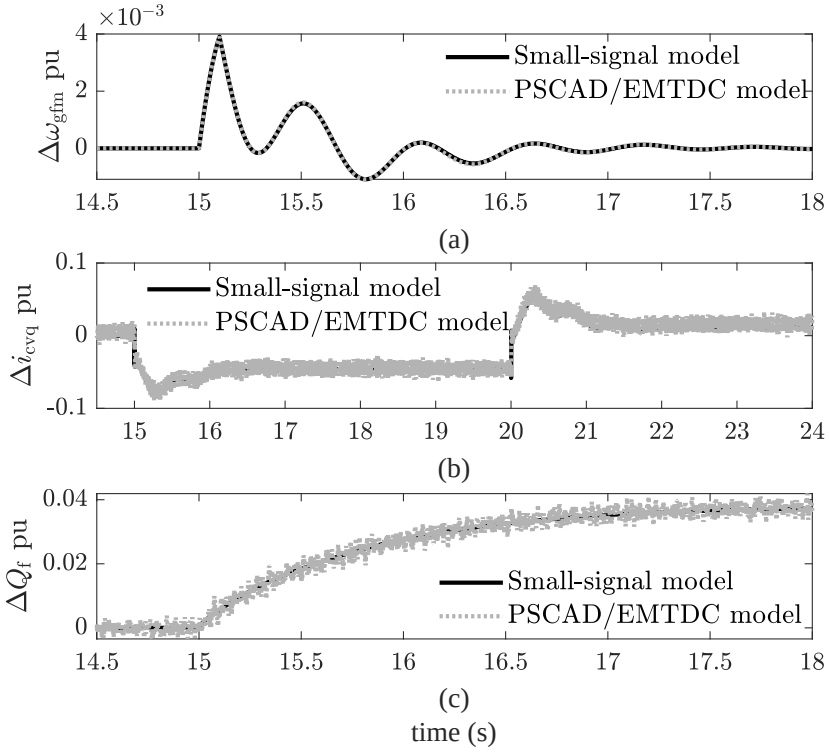

Fig. 4.6: Small-signal vs. EMT response for virtual admittance based inner current controller embedded GFM inverter system.

4.3 Eigenvalue Analysis

This section discusses the results obtained from eigenvalue analysis for the above-mentioned current controllers' embedded scenarios.

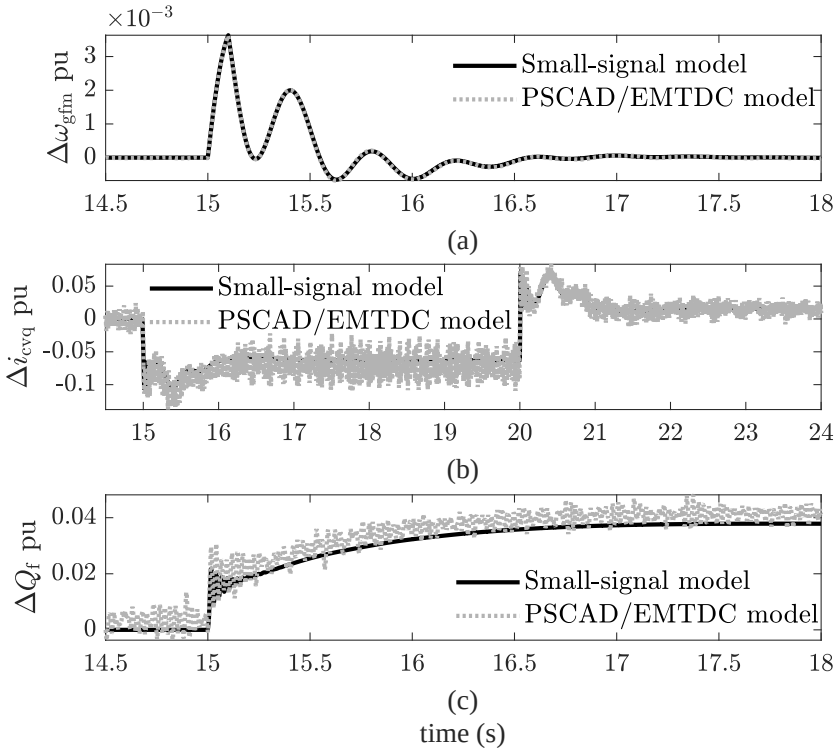

Fig. 4.7: Small-signal vs. EMT response for cascaded voltage-current controller embedded GFM inverter system.

4.3.1 Virtual admittance-based inner current controller

Besides the two critical modes identified with the virtual impedance-based current controller embedded scenario (Chapter 3), the virtual admittance-based inner current controller introduces two additional modes. Table 4.3 summarizes those critical modes' characteristics and significantly participating state variables.

Table 4.3: Major Participants in the Critical Modes with virtual Admittance based Inner Current Controller

Mode	**Freq** (Hz)	$\boldsymbol{\zeta}$ (%)	**Major participants**
1	1.8	13.4	δ[100%], ω_{sm}[56%], ω_{gfm}[45%]
2	0.4	63.3	T_{m} [100%], x_2 [73%], ω_{gfm} [67%], ψ_{fd} [46%], ω_{sm} [33%], x_1 [24%], δ [23%]
3	48.3	60.8	i_{cvd} [100%], i_{cvq} [95%], x_4 [66%], x_5 [62%], i_{q} [41%], i_{d} [40%]
4	333.8	7.5	v_{fd} [100%], v_{fq} [100%], i_{cvd} [66%], i_{cvq} [66%], i_{td} [52%], i_{tq} [52%], i_{txd} [27%], i_{txq} [27%]

Modes 1 and 2, respectively, correspond to virtual electromechanical mode and governor mode identified in Chapter 3. Therefore, mode shape diagrams are given only for modes 3 and 4 in Figs.4.8a and 4.8b, respectively. As shown in mode shape diagrams, modes 3 and 4 are network modes excited by the virtual admittance-based inner current controller.

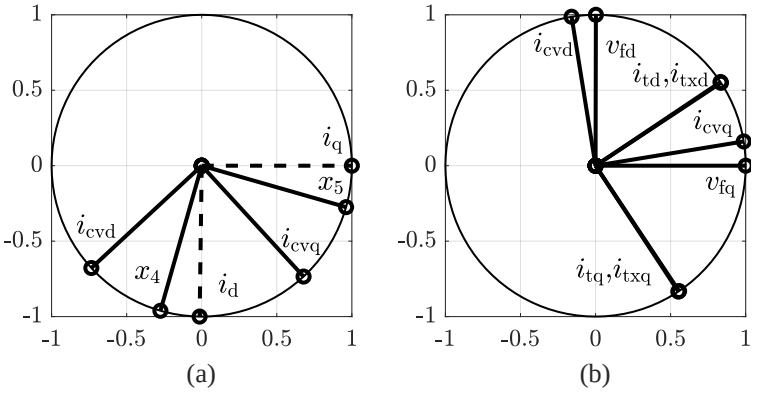

Fig. 4.8: Mode shapes of major participants from GFM inverter (solid line) and synchronous machine (dashed line) for (a) mode 3 and (b) mode 4.

This eigenvalue analysis reveals that high-bandwidth inner controller loops lead to high-frequency network interactions. Therefore, depending on the GFM controller topology, GFM inverters can excite interactions in a wide frequency range.

A separation of significantly participating state variables in the low-frequency modes (i.e., modes 1-2) and high-frequency modes (i.e., modes 3-4) can be observed in Table 4.3. Further, the effect on low-frequency modes from their significantly participating control and network parameters have already been discussed in Chapters 2 and 3. Therefore, the sensitivity analyses are limited to the following list.

- Effect of virtual admittance
- Effect of the inner decoupled current controller
- GFM inverter penetration level.

Effect of virtual admittance block

The effect of the virtual admittance block is analyzed by changing R_{virt}, X_{virt}, X/R ratio, and Z_{virt}. X_{virt} is changed between 0.1 pu - 1.2 pu while keeping $R_{\text{virt}} = 0$. Similarly, the effect of R_{virt} is analyzed. To analyze the effect of the X/R ratio, its value is changed between 0.1 and 5 while keeping Z_{virt} at 0.5 pu. Z_{virt} is changed between 0.01 pu and 1 pu with a X/R ratio of 2 to analyze the effect of Z_{virt}. Except for mode 2, all the other modes are significantly affected by the changes in the virtual admittance parameters. Figs. 4.9a, 4.9b and 4.9c give the locus of eigenvalues correspond to modes 4, 3 and 1, respectively. The arrow by each curve shows the movement of the eigenvalue with the increment of the corresponding parameter.

As shown in Figs. 4.9a and 4.9b, the increment of the virtual impedance (i.e., either X_{virt}, R_{virt} or both) has improved the damping of these two network modes. The increment of the virtual impedance reduces the sensitivity to voltage changes between the converter terminal and PCC, leading to a slower GFM controller. Such slow controllers discourage network interactions. Oppositely, the increment of virtual impedance (i.e., either X_{virt}, R_{virt} or both) has reduced the damping of the virtual electromechanical mode as shown in Fig. 4.9c. This is because the sluggish GFM inverter encourages the interactions between the GFM inverter and the synchronous machine. In particular, the increment of R_{virt} has worsened the damping of mode 1 due to the increased coupling effect between $P - f$ and $Q - v$ droop paths.

The operating conditions marked from red circles in Fig. 4.9 correspond to (a): $X_{\text{virt}} =$ 0.35 pu, $R_{\text{virt}} = 0$ and (b):$X_{\text{virt}} = 0$ pu, $R_{\text{virt}} = 0.8$ pu. Filter capacitor voltage's q-axis component variation following a ΔR_{L} = -0.1 pu at t = 10 s is obtained from PSCAD/EMTDC and given in Fig. 4.10a. Negatively damped oscillations at the frequency of mode 4 can be observed in v_{fq}. Fig. 4.10b gives the ω_{sm} variation following a 0.1 pu ω_{gfmref} impulse at t = 10 s. This shows the highly under damped oscillations correspond to mode 1. These verify the results obtained from eigenvalue analysis.

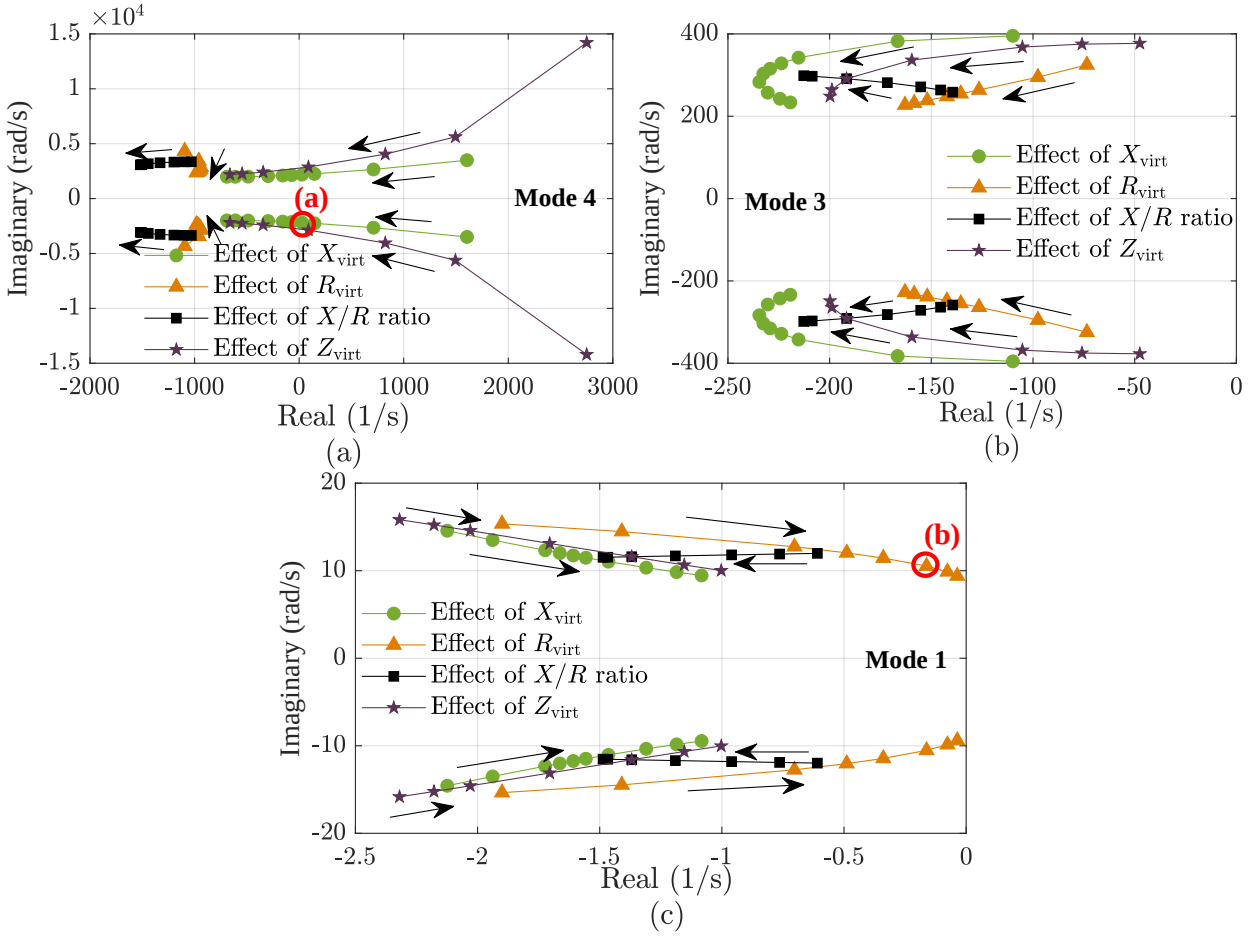

Fig. 4.9: Locus of eigenvalue for changes in R_{virt}, X_{virt}, X/R ratio and Z_{virt} in (a) mode 4, (b) mode 3 and (c) mode 1.

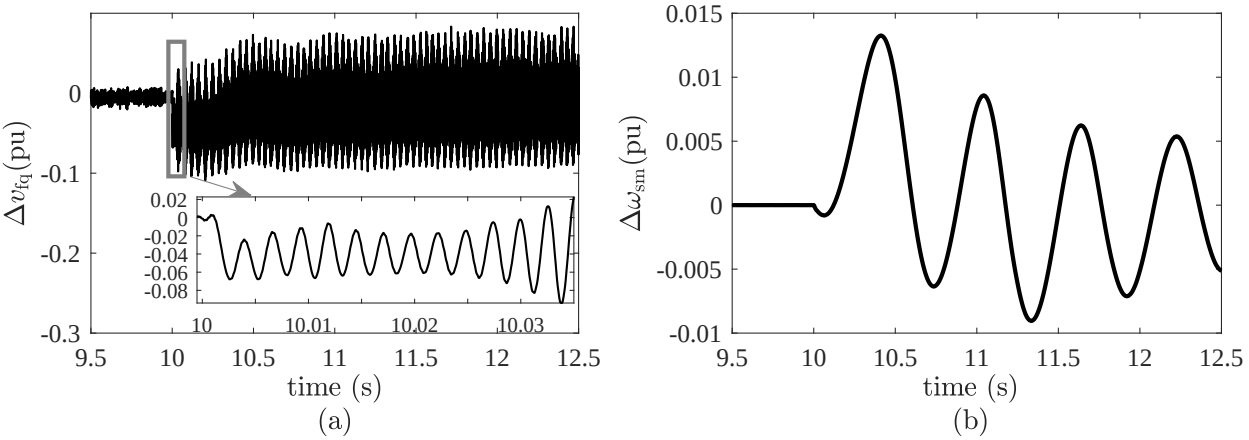

Fig. 4.10: PSCAD/EMTDC responses for (a) $X_{\text{virt}} = 0.35$ pu, $R_{\text{virt}} = 0$ and (b) $X_{\text{virt}} = 0$ pu, $R_{\text{virt}} = 0.8$ pu.

Effect of inner decoupled current controller

The inner decoupled current controller effect on the critical modes is first analyzed by changing the PI controller's integral time constant (T_{ii}) in the range of 0.005 s - 0.1 s while keeping proportional gain (K_{pi}) of the PI controller at 0.1. Then K_{pi} is changed from 0 to 1 while keeping $T_{\text{ii}} = 0.05$ s. The movement of the eigenvalue corresponding to each critical mode reveals that the effect of the inner controller dynamics on the low-frequency interactions, i.e., modes 1 and 2, are negligible. However, the impact on the network modes, i.e., modes 3 and 4 are significant. Figs. 4.11a and 4.11b give the locus of eigenvalue corresponds to mode 4 and 3, respectively.

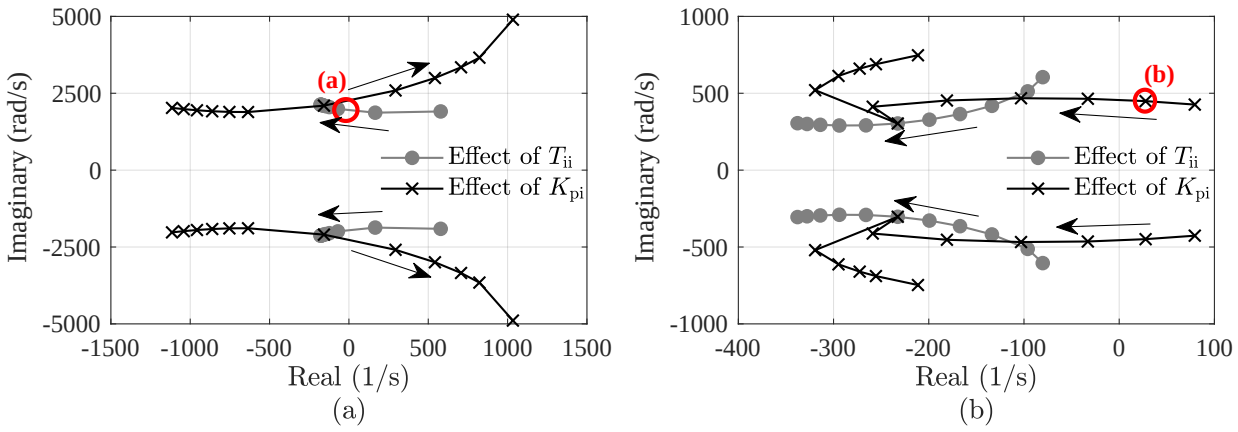

Fig. 4.11: Locus of eigenvalue corresponds to (a) mode 4 and (b) mode 3 for changes in inner decoupled controller dynamics.

As shown in Fig. 4.11, the increment of T_{ii} has increased the damping of both the network modes. This is because of the sluggish GFM controller's reluctance to excite high-frequency network modes. However, large values of K_{pi} reduce the damping of mode 4 while increasing the damping of mode 3. Therefore, there is a limited region for K_{pi}, which makes this GFM inverter system stable. The operating points marked from red circles in Fig. 4.11 corresponds to (a) $T_{\text{ii}} = 0.02$ s, $K_{\text{pi}} = 0.1$ and (b) $T_{\text{ii}} = 0.05$ s, $K_{\text{pi}} = 0.01$. PSCAD/EMTDC responses for -20% and -10% step changes in load resistance, respectively, for operating conditions (a) and (b) are given in Figs. 4.12a and 4.12b, respectively. Under damped oscillations

corresponding to mode 4 can be observed in 4.12a. The negatively damped oscillations corresponding to mode 3 are observable in 4.12b. These verify the results obtained from eigenvalue analysis.

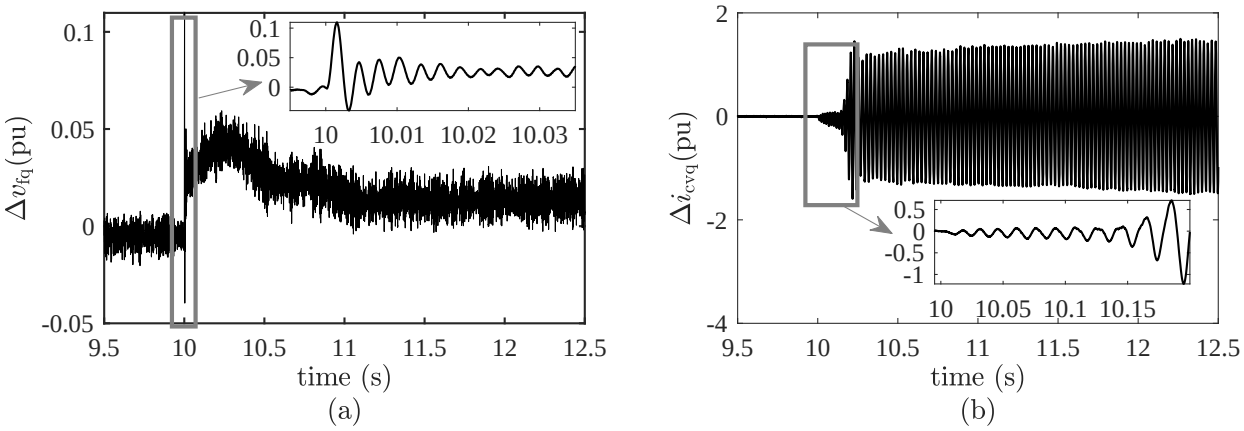

Fig. 4.12: PSCAD/EMTDC responses for (a) $T_{\mathrm{ii}} = 0.02$ s, $K_{\mathrm{pi}} = 0.1$ and (b) $T_{\mathrm{ii}} = 0.05$ s, $K_{\mathrm{pi}} = 0.01$.

GFM inverter penetration level

To analyze the effect of virtual admittance-based inner current controller embedded GFM inverter penetration level on the system stability, the network parameters are changed as mentioned in Table 3.3. The eigenvalue analysis reveals that compared to mode 4, all the other modes are negligibly sensitive to the inverter penetration level. Fig 4.13 shows the impact of GFM inverter penetration level on mode 4. As shown in Fig 4.13 the virtual admittance-based inner current controller embedded GFM inverter's dominance has pushed the system to instability. On the contrary, the virtual impedance-based current controller embedded GFM inverter penetration level improves the system stability in section 3.4.5. This is because the virtual impedance-based current controller does not have high-bandwidth inner control layers that will excite network modes. Therefore, this clearly shows the high-bandwidth inner control layers in the GFM controller topology restrain the possibility of reaching high GFM inverter penetration.

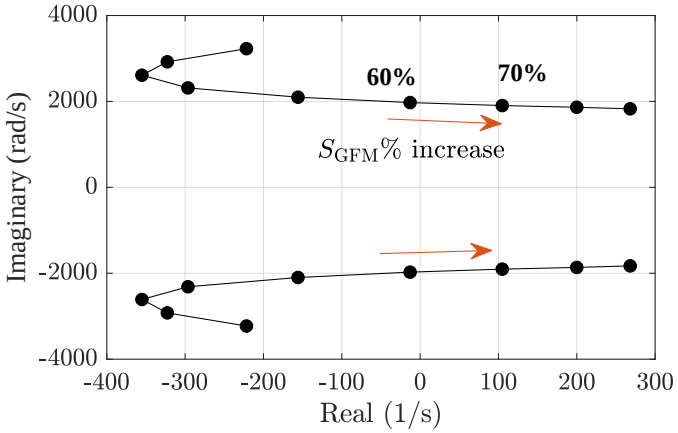

Fig. 4.13: The locus of eigenvalue corresponds to mode 4 with changes in GFM inverter penetration level.

4.3.2 Cascaded voltage-current controller

The eigenvalue analysis for cascaded voltage-current controller embedded GFM inverter system reveals three critical modes as shown in Table 4.4. Modes 1 and 2, respectively, correspond to the virtual electromechanical mode and the governor mode identified in Chapter 3. Mode 3 corresponds to the 48.3 Hz network mode identified in the virtual admittance-based inner current controller embedded GFM inverter system in section 4.3.1. However, the mode 3 of the cascaded voltage-current controller embedded scenario shows a significantly lower damping compared to the virtual admittance-based inner current controller embedded scenario.

Table 4.4: Major Participants in the Critical Modes with Cascaded Voltage-Current Controller

Mode	**Freq** (Hz)	ζ (%)	**Major participants**
1	2.6	14.6	δ[100%], ω_{sm}[50%], ω_{gfm}[50%]
2	0.5	57.9	T_{m} [100%], x_2 [77%], ω_{gfm} [67%], ω_{sm} [45%],
3	39.1	6.4	i_{cvq} [100%], i_{cvd} [76%], i_{d} [67%], i_{q} [67%], i_{tq} [41%], i_{td} [39%], E_{f} [26%], i_{txq} [22%], i_{txd} [20%]

Though the effect on those modes has been discussed with different GFM controllers, this section analyzes the impact of cascaded control structure on system stability. It also analyzes the effect of cascaded voltage-current controller embedded GFM inverter penetration.

Effect of cascaded voltage-current controller bandwidth

To analyze the effect of the cascaded nature of the controller on the system stability, firstly, the most inner current controller's bandwidth is changed by changing the integral time constant of the PI controllers in that layer from 0.01 s to 0.45 s. Then, the voltage controller's bandwidth and current controller's bandwidth are changed. For this exercise, the integral time constants of the voltage control layer are set between 0.025 s and 0.5 s. Further, to extend the analysis, the $Q - v$ controller's bandwidth is changed along with the aforementioned time constants for the inner control layers. To accomplish this, the integral time constant in the $Q - v$ controller path is changed from 0.05 s to 0.55 s.

The eigenvalue analysis shows that the changes in the cascaded controller bandwidth do not significantly affect the virtual electromechanical and governor modes. The movement of eigenvalues of mode 3 to the changes in the bandwidths of current controller, both voltage and current controllers and all three control layers, i.e., $Q-v$, voltage and current controllers are shown in Fig. 4.14.

As shown in Fig 4.14, mode 3 is majorly sensitive to inner current controller dynamics. i.e., the faster the inner current controller, the higher the possibility of reaching instability. The fast-acting capability of both the inner control layers (i.e., voltage and current) reduces the stability further. However, the sensitivity to outer $Q-v$ controller dynamics is minimal. It is worth noting that even the inner control layers of the cascaded voltage-current controller have comparative bandwidths to the current controller in the virtual admittance-based inner current controller, the high-frequency interaction in the LC filter components (i.e., mode 4 in section 4.3) is not excited. This demonstrates the cascaded voltage-current controller's ability to dampen the LC filter interactions.

GFM inverter penetration level

The impact of cascaded voltage-current controller embedded GFM inverter penetration is analyzed by setting the network parameters as mentioned in Table 3.3. According to eigenvalue

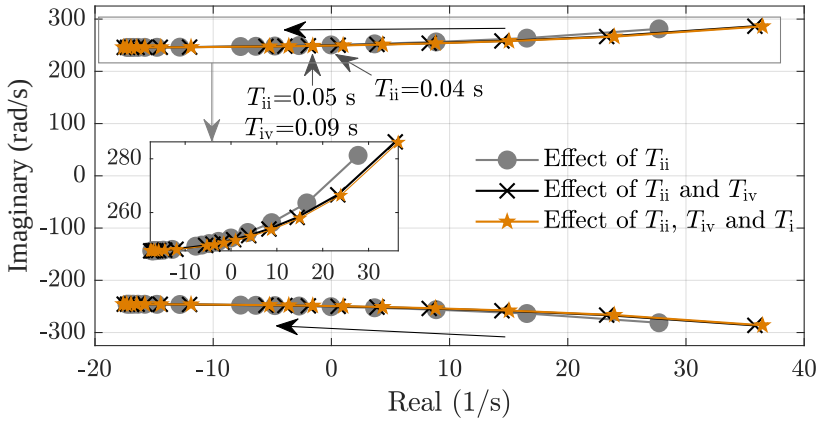

Fig. 4.14: The locus of eigenvalue corresponds to mode 3 with changes in cascaded voltage-current controller bandwidth.

analysis, modes 1 and 2 are negligibly affected by the cascaded voltage-current controller embedded GFM inverter penetration level compared to mode 3. The movement of eigenvalue corresponds to mode 3 is shown in Fig. 4.15.

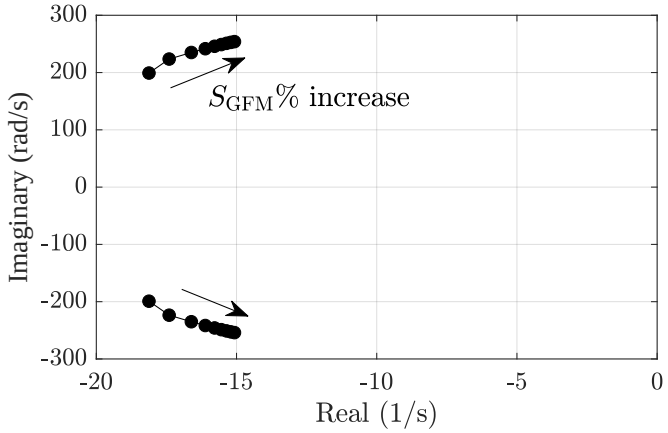

Fig. 4.15: The locus of eigenvalue corresponds to mode 3 with changes in GFM inverter penetration level.

Significant penetrations of cascaded voltage-current controller embedded GFM inverter reduce the stability slightly, however system remains in the stability region. The possibility of extending the GFM inverter penetration level is promising in the cascaded voltage-current controller utilized GFM inverter scenario compared to the virtual admittance-based inner current controller utilized GFM inverter scenario.

4.4 Fault-Ride-Through Capability

Following the eigenvalue analysis for the GFM inverter systems consisting of a virtual impedance-based current controller, virtual admittance-based inner current controller, and cascaded voltage-current controller, the parameters in Table 4.5 are selected. The current dependent virtual impedance path's parameters (i.e., K_{pRVI}, K_{pLVI} and $i_{\text{threshold}}$) of the virtual impedance-based current controller are selected following detailed PSCAD/EMTDC simulations as mentioned in [33].

Table 4.5: The Selected Control Parameters for each Current Limiting Method

Virtual impedance based current controller
$K_{\text{pRvi}} = 5$, $i_{\text{threshold}} = 1.1$, $R_{\text{vi0}} = L_{\text{vi0}} = K_{\text{pLvi}} = 0$
Virtual admittance based inner current controller
$X_{\text{virt}} = 0.49$, $R_{\text{virt}} = 0.098$, $K_{\text{pi}} = 0.05$, $T_{\text{ii}} = 0.07$ s
Cascaded voltage-current controller
$T_{\text{i}} = 0.284$ s, $T_{\text{iv}} = 0.374$ s, $T_{\text{ii}} = 0.241$ s

To compare the robustness of the current limiting methods, the GFM inverter is controlled using each of those above current limiting algorithms. At each current controller-embedded scenario, a three-phase-to-ground fault is applied to the LC filter terminal for 0.1 s. The obtained results from each current limiting algorithm are shown in Fig. 4.16. Here, VICC: virtual impedance-based current controller, VAICC: virtual admittance-based inner current controller, and CVCC: cascaded voltage-current controller. The detailed time domain results verify the ability of each current limiting algorithm to limit the converter current well below 2.0 pu and successfully fault-ride-through with the synchronous machine.

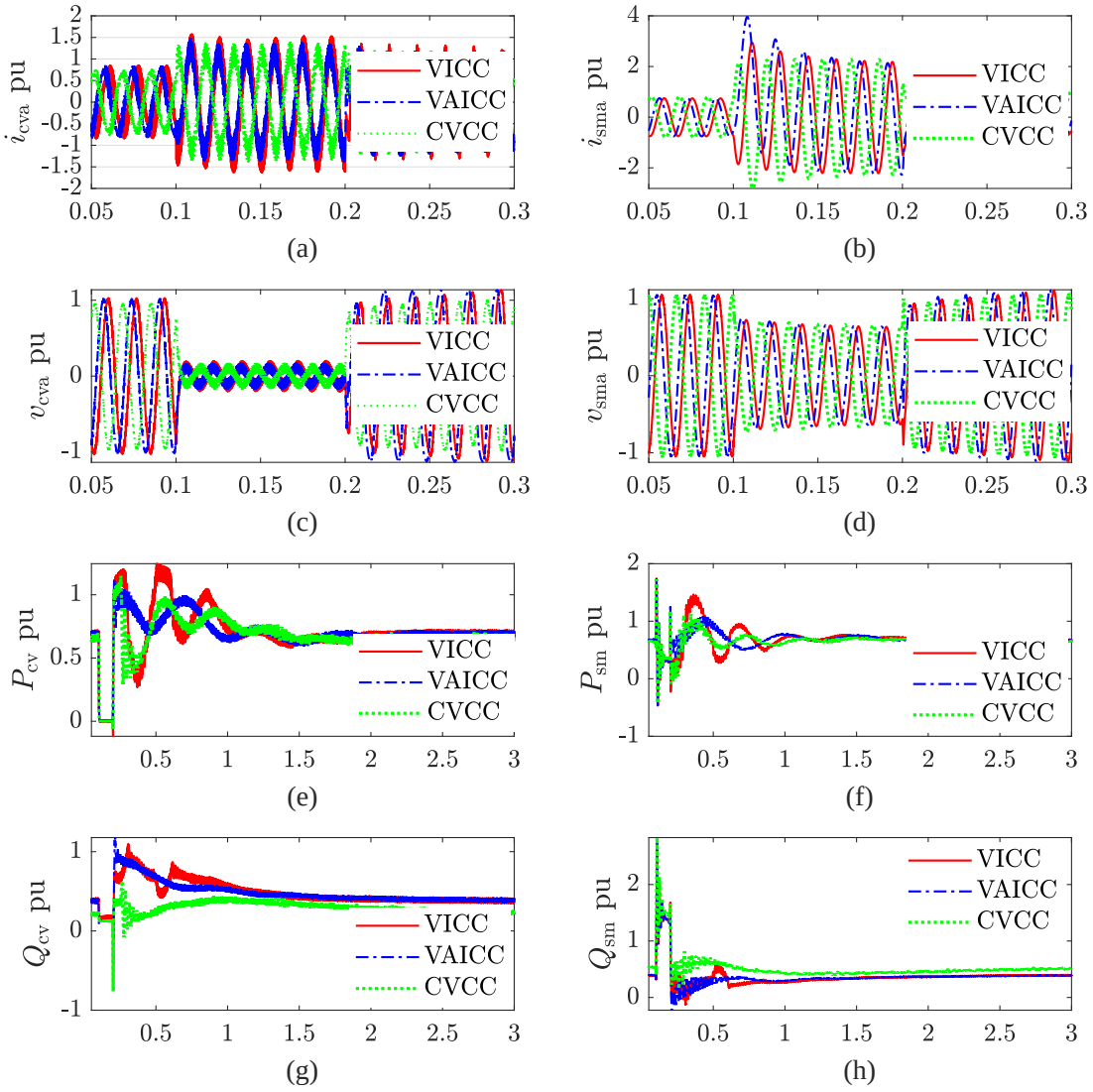

Fig. 4.16: The fault responses corresponding to phase-a current of (a) converter, (b) synchronous machine, phase-a terminal voltage of (c) converter, (d) synchronous machine, active power output of (e) converter, (f) synchronous machine, and reactive power output of (g) converter, (h) synchronous machine from the test system consisting of parallel connected GFM inverter and synchronous machine.

The study is extended by analyzing the ability of the above current-limiting algorithms to fault-ride through with a single GFM inverter in the islanded mode. The same fault condition as mentioned above is applied. The detailed time domain responses obtained from PSCAD/EMTDC are shown in Fig.4.17. This shows the ability of each of the considered current limiting algorithms embedded GFM inverters in islanded mode to feed and recover

from a three-phase-to-ground fault at the converter terminal.

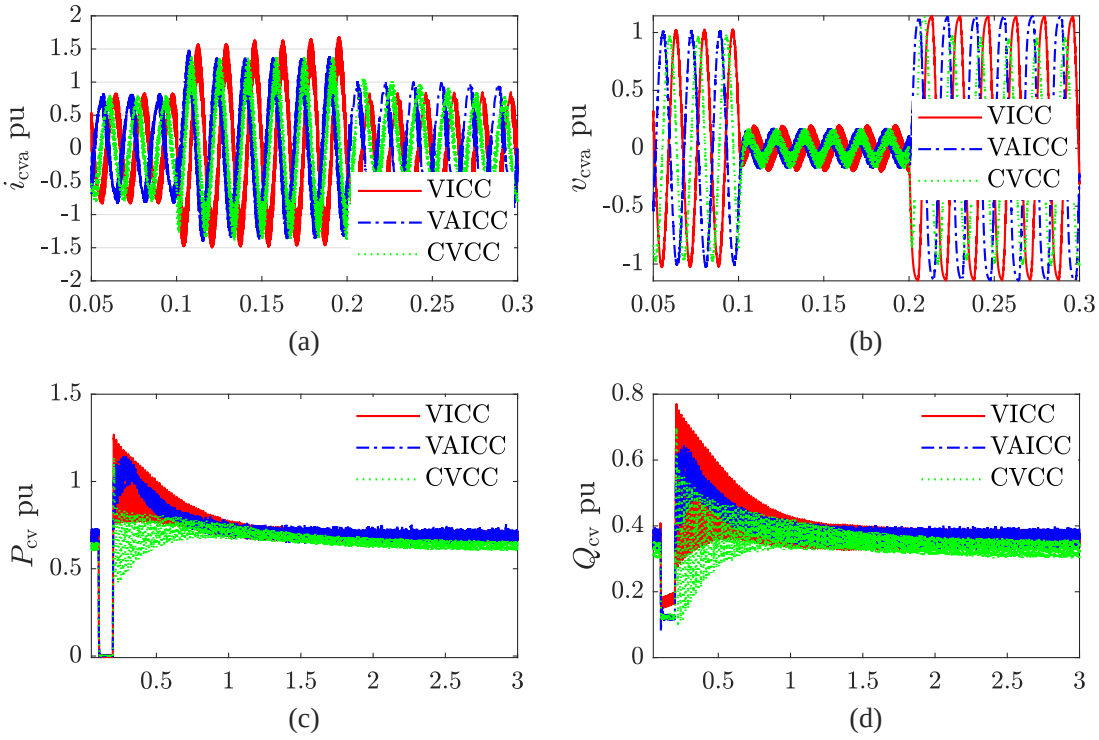

Fig. 4.17: The fault responses corresponding to converter's (a) phase-a current, (b) phase-a terminal voltage, (c) active power output, and (d) reactive power output from the test system consisting of a GFM inverter in the islanded mode.

The ability of the parallel-connected GFM inverter system (in Chapter 2) to fault-ride through with a three-phase-to-ground fault applied at one of the GFM inverter's *LC* filter terminal is also studied. The detailed PSCAD/EMTDC results are shown in Fig. 4.18. This indicates that although all three current limiting algorithms can successfully limit the fault current, the cascaded voltage-current controller can not recover from the fault. Both GFM inverters act as current sources, leading to challenging fault recovery in multi-loop structures. However, the virtual admittance-based inner current controller recovers from the fault due to its fast-acting capability compared to the sluggish response from the cascaded voltage-current controller.

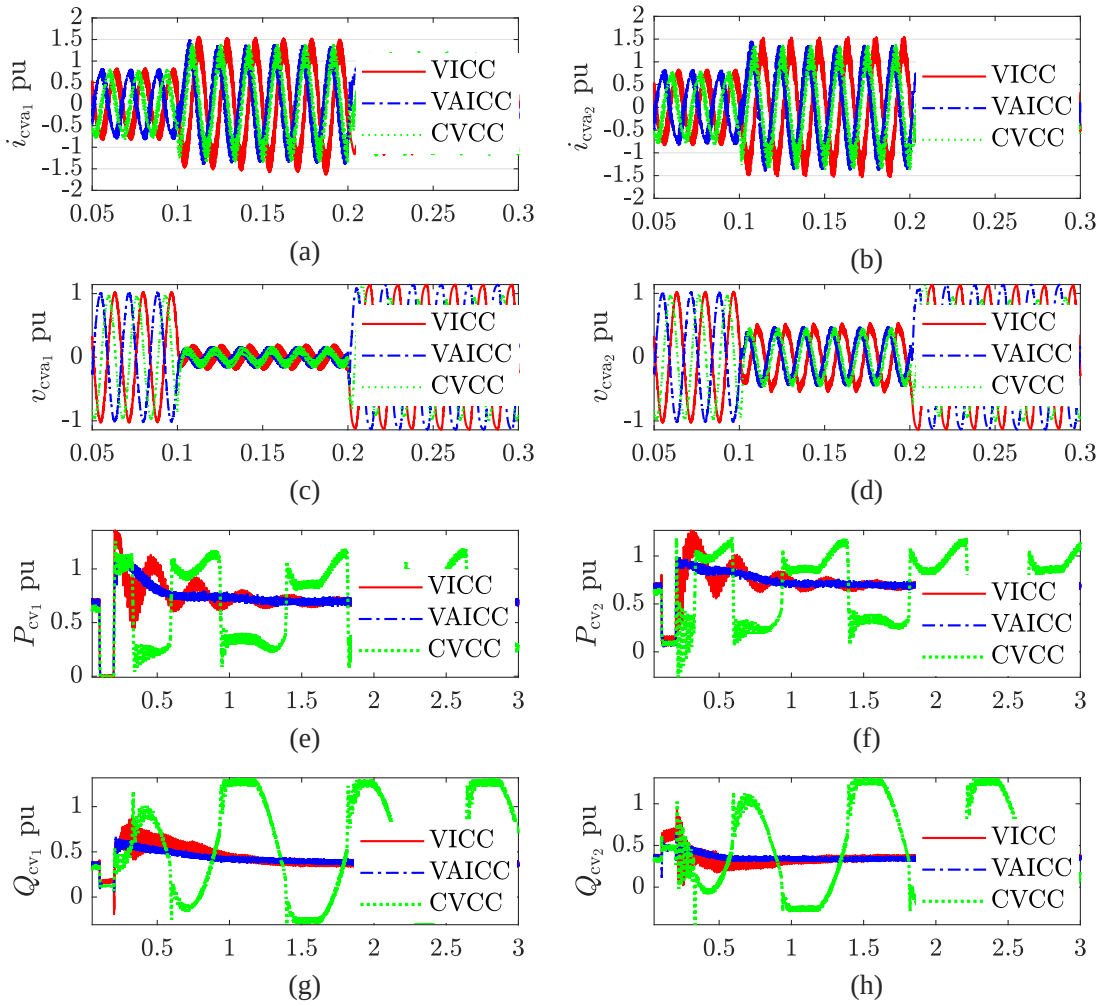

Fig. 4.18: The fault responses corresponding to phase-a current of (a) converter-1, (b) converter-2, phase-a terminal voltage of (c) converter-1, (d) converter-2, active power output of (e) converter-1, (f) converter-2, and reactive power output of (g) converter-1, (h) converter-2 from the test system consisting of parallel connected GFM inverters in the islanded mode.

The FRT test results from different system configurations reveal the ability of the no-loop current controller to ride through faults with all the tested system configurations. However, the current limiting is less tight in no-loop (i.e., when only the current dependent virtual impedance is used) compared to multi-loop controllers. The cascaded voltage-current controller fails to ride through faults when only parallel GFM inverters are present. This is because its operation as a sluggish current source during the fault. The multi-loop controller with only an inner decoupled current controller allows successful fault-ride-through under

all the tested conditions and provides a tighter current control with compared to other considered current-limiting methods.

4.5 Summary

This chapter analyzed the effect of no-loop (virtual impedance-based current controller) and multi-loop current controllers (virtual admittacne-based inner current controller, cascaded voltage-current controller) in causing interactions in GFM inverter systems. A comparative analysis of the FRT capability of each considered current limiting method was also conducted. The key contributions of this chapter are:

- Demonstration of the ability of multi-loop control structures to excite high-frequency network modes compared to the no-loop current controller, which challenges the multi-loop controllers embedded in GFM inverters to dominate the power system.

- Identification of the ability of fast-acting inner controllers to reduce the damping of the network modes while having a negligible impact on virtual electromechanical and governor modes.

- Revealing of the opposite effect of virtual impedance (i.e., used for current reference calculation in the virtual admittance-based inner current controller) in the network modes and the virtual electromechanical mode.

- Illustration of the capability of the cascaded voltage-current controller structure to damp filter interactions compared to the virtual admittance-based inner current controller, which consists of only an inner current controller.

- Demonstration of the ability of the considered current limiting methods to limit the fault current well below 2.0 pu in the systems consisting of only GFM inverters and GFM inverters in parallel with synchronous machines.

- Demonstration of the inability of the slow-acting multi-loop cascaded voltage-current control structure to recover from fault, especially when there are no other voltage sources in the system.

Chapter 5

Effect of the DC-Side Dynamics

The power modulations carried out by a GFM inverter are profoundly affected by the capability of the inverter's dc-side circuit to support such modulations. Virtual synchronous machine-based power management controllers have been introduced to dc microgrids through extensive consideration of different dc-side dynamic devices, including renewable energy sources, energy storage devices, dc loads, etc., [34–36]. However, these studies do not include an analysis of interactions or ac-side dynamics. An example of stability analysis of a dual-droop-controlled dc microgrid without considering the ac-side dynamics can be found in [37].

The effects of dc-side dynamics on GFL inverters have been extensively studied for multi-terminal HVDC [38], solar PV [39], and wind plant applications [40]. However, most studies of GFM inverters assume an ideal dc side [11–13] that can meet the ac-side power modulation requirements. Interactions are, however, influenced by the dc-side circuitry and controller(s), and ignoring them leads to incorrect and incomplete conclusions. These dc-side limitations can lead to power imbalances, interactions, and degradation of the dc-link voltage, jeopardizing the overall performance of the GFM inverter. The survey of contemporary literature clearly shows a gap in knowledge for analyzing the root causes of interactions in GFM inverter systems considering both dc and ac dynamics.

This chapter presents an in-depth study of the interactions in grid-forming inverter systems, considering the critical dynamics contributed by the inverter's dc-side and ac-side. The test system with the parallel connected GFM inverter and the synchronous machine is selected for the study with the virtual admittance-based inner current controller in Chapter 4. A dc-source connection via a bi-directional dc-dc converter is considered for the dc-side of the GFM inverter, as this test system represents several practical applications.

The discussion on dc-side circuitry and controller is given in section 5.1, and the discussions on the GFM controller and the ac network components can be found in Chapters 2 to 4. Section 5.2 includes the modification to small-signal modeling from section 4.2.1. The eigenvalue analysis is included in section 5.3. The results of the eigenvalue analysis are compared with section 4.3.1 that considered the ideal dc-side. A chapter summary and a list of contributions are given in section 5.4.

5.1 Test System

The test system considered for the study is depicted in Fig.5.1. The ac network parameters are similar to Chapter 3. The topology and parameters of the virtual admittance-based inner current controller embedded GFM controller are given in Chapters 2 and 4. The ideal dc-side and the dc source connected via a bi-directional dc-dc converter are identified as configuration A and configuration B, respectively, in Fig.5.1.

Configuration B consists of a smoothing inductor (L_{bat}), dc-link voltage filter capacitor (C_{dc}), and a bi-directional dc-dc converter with its controller. The dc-dc converter controller consists of an outer dc-link voltage loop and an inner source-current loop (see Fig. 5.2). The duty cycle (d) generated by the dc-side controller is compared against a high-frequency sawtooth waveform to generate the switching commands for the bi-directional dc-dc converter. Since the current flowing out of the battery is considered positive, S_2 is treated as the main switch and S_1 receives a complementary switching command. The dc-side circuitry

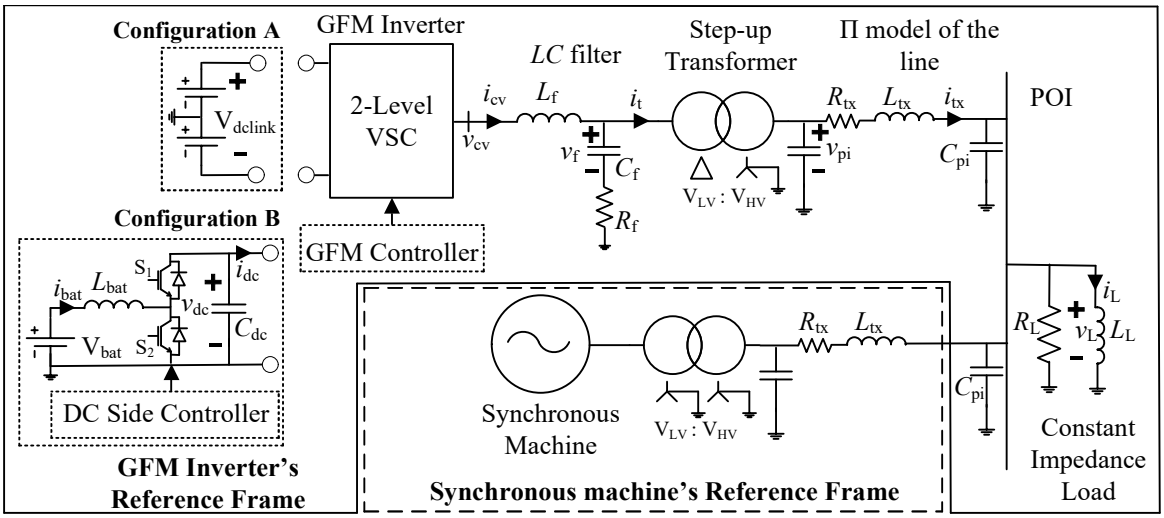

Fig. 5.1: Test system to study dc-side effect on GFM inverter interactions.

Table 5.1: Control and Network Parameters of the DC Side

DC-circuitry parameters
$V_{dclink} = 26$ kV, $V_{bat} = 13$ kV, $L_{bat} = 25$ mH, $C_{dc} = 7.5$ mF
DC-voltage loop parameters
$V_{dcref} = 26$ kV, $T_{ivdc} = 0.1$ s, $K_{pvdc} = 0.5$, $T_{vdc} = 0.01$ s
DC-current loop parameters
$T_{iibat} = 0.05$ s, $K_{pibat} = 0.5$, $T_{ibat} = 0.01$ s, $T_{idc} = 0.01$ s

parameters and the dc-side controller parameters are given in Table 5.1.

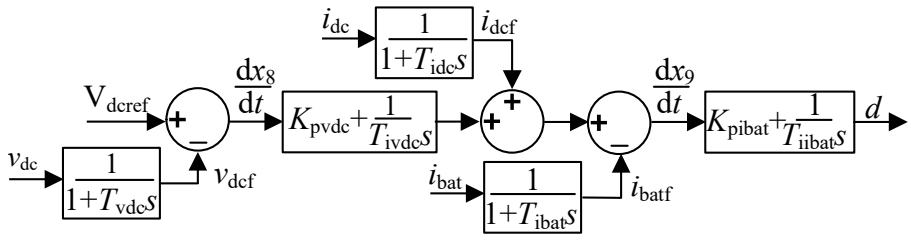

Fig. 5.2: Control block diagram of the dc-dc converter.

5.2 Small-Signal Model Development

5.2.1 DC-side circuitry and controller

The integration of dc-side configuration A with the rest of the model has already been discussed in previous chapters. To include configuration B in the model, the output of the Q-v controller is assumed to be the modulation index, m, for the PWM modulator of the GFM inverter. In per-unit, the relationship between the dc-side voltage, v_{dc}, and the peak voltage of the ac side voltage of the converter terminal, v_{pk}, is given in (5.1).

$$v_{\mathrm{pk}} = m v_{\mathrm{dc}} \tag{5.1}$$

The expected converter terminal voltage's dq components generated by the Q-v controller to the high-voltage side of the transformer are identified as v_{td} and v_{tq} and calculated as per (5.2). The 30° phase shift is due to the $\Delta - \mathrm{Y}$ transformer.

$$v_{\mathrm{td}} = m v_{\mathrm{dc}} \sin(-30^\circ) \qquad\qquad v_{\mathrm{tq}} = m v_{\mathrm{dc}} \cos(-30^\circ) \tag{5.2}$$

Assuming a lossless converter, the power balance between dc and ac sides is as shown in (5.3), where i_{dc} is the dc line current. The d and q components of the converter current are given by i_{cvd} and i_{cvq}, respectively.

$$v_{\mathrm{dc}} i_{\mathrm{dc}} = v_{\mathrm{td}} i_{\mathrm{cvd}} + v_{\mathrm{tq}} i_{\mathrm{cvq}} \tag{5.3}$$

By substituting (5.2) in (5.3), (5.4) can be obtained.

$$i_{\mathrm{dc}} = \sin(-30^\circ) m i_{\mathrm{cvd}} + \cos(-30^\circ) m i_{\mathrm{cvq}} \tag{5.4}$$

The non-linear equations that describe the dynamics of the dc-side circuitry and the dc-side controller are given in (5.5)-(5.11).

$$\mathrm{d}i_{\mathrm{bat}}/\mathrm{d}t = (\omega_{\mathrm{b}}/L_{\mathrm{bat}})\,(\mathrm{V}_{\mathrm{bat}} - v_{\mathrm{dc}}(1-d)) \tag{5.5}$$

$$\mathrm{d}v_{\mathrm{dc}}/\mathrm{d}t = (\omega_{\mathrm{b}}/C_{\mathrm{dc}})\,(-i_{\mathrm{dc}} + i_{\mathrm{bat}}(1-d)) \tag{5.6}$$

$$\mathrm{d}v_{\mathrm{dcf}}/\mathrm{d}t = (1/T_{\mathrm{vdc}})\,(v_{\mathrm{dc}} - v_{\mathrm{dcf}}) \tag{5.7}$$

$$\mathrm{d}i_{\mathrm{dcf}}/\mathrm{d}t = (1/T_{\mathrm{idc}})\,(i_{\mathrm{dc}} - i_{\mathrm{dcf}}) \tag{5.8}$$

$$\mathrm{d}i_{\mathrm{batf}}/\mathrm{d}t = (1/T_{\mathrm{ibat}})\,(i_{\mathrm{bat}} - i_{\mathrm{batf}}) \tag{5.9}$$

$$\mathrm{d}x_8/\mathrm{d}t = V_{\mathrm{dcref}} - v_{\mathrm{dcf}} \tag{5.10}$$

$$\mathrm{d}x_9/\mathrm{d}t = K_{\mathrm{pvdc}}(V_{\mathrm{dcref}} - v_{\mathrm{dcf}}) + (1/T_{\mathrm{ivdc}})\,x_8 + i_{\mathrm{dcf}} - i_{\mathrm{batf}} \tag{5.11}$$

The output of the dc-side controller, which is the dc-dc conventer's duty cycle (d), is given by (5.12).

$$d = (1/T_{\mathrm{iibat}})\,x_9 + K_{\mathrm{pibat}}(K_{\mathrm{pvdc}}(V_{\mathrm{dcref}} - v_{\mathrm{dcf}}) + (1/T_{\mathrm{ivdc}})\,x_8 + i_{\mathrm{dcf}} - i_{\mathrm{batf}}) \tag{5.12}$$

Readily the linearized versions of (5.5)-(5.11) can be obtained as shown in (5.13).

$$\begin{aligned}\boldsymbol{\Delta\dot{X}_{\mathbf{DC}}} = \boldsymbol{A_{\mathbf{DC}}\Delta X_{\mathbf{DC}}} + \boldsymbol{A_{\mathbf{DCP}}\Delta X_{\mathbf{P}}} + \boldsymbol{A_{\mathbf{DCCC}}\Delta X_{\mathbf{CC}}} + \boldsymbol{A_{\mathbf{DCLCL}}\Delta X_{\mathbf{LCL}}} + \boldsymbol{A_{\mathbf{DCN}}\Delta X_{\mathbf{N}}} + \\ \boldsymbol{A_{\mathbf{DCL}}\Delta X_{\mathbf{L}}} + \boldsymbol{B_{\mathbf{DCgfm}}\Delta U_{\mathbf{gfm}}} + \boldsymbol{B_{\mathbf{DC}}\Delta U_{\mathbf{DC}}}\end{aligned} \tag{5.13}$$

Here, $\boldsymbol{\Delta X_{\mathbf{P}}}, \boldsymbol{\Delta X_{\mathbf{CC}}}, \boldsymbol{\Delta X_{\mathbf{LCL}}}, \boldsymbol{\Delta X_{\mathbf{N}}}, \boldsymbol{\Delta X_{\mathbf{L}}}$, and $\boldsymbol{\Delta U_{\mathbf{gfm}}}$ are similar to section 4.2.1. $\boldsymbol{\Delta X_{\mathbf{DC}}}$ and $\boldsymbol{\Delta U_{\mathbf{DC}}}$ are defined as follows;

$$\boldsymbol{\Delta X_{\mathbf{DC}}} = \begin{bmatrix} \Delta i_{\mathrm{bat}} & \Delta v_{\mathrm{dc}} & \Delta v_{\mathrm{dcf}} & \Delta i_{\mathrm{dcf}} & \Delta i_{\mathrm{batf}} & \Delta x_8 & \Delta x_9 \end{bmatrix}^{\mathrm{T}}$$

$$\boldsymbol{\Delta U_{DC}} = \begin{bmatrix} \Delta \mathrm{V_{dcref}} \end{bmatrix}$$

The expanded forms of the matrices in (5.13) are in Appendix F.1.

5.2.2 Power controller

The small-signal model derivation of this component is similar to section 4.2.1. The linearized representation of the power controller with dc-side configuration B is given in (5.14).

$$\boldsymbol{\Delta \dot{X}_P} = \boldsymbol{A_{PDC}\Delta X_{DC}} + \boldsymbol{A_P\Delta X_P} + \boldsymbol{A_{PCC}\Delta X_{CC}} + \boldsymbol{A_{PLCL}\Delta X_{LCL}} + \boldsymbol{A_{PN}\Delta X_N} + \boldsymbol{A_{PL}\Delta X_L} + \boldsymbol{B_P\Delta U_{gfm}} + \boldsymbol{B_{PDC}\Delta U_{DC}} \quad (5.14)$$

The expanded form of matrices in (5.14) are similar to expanded matrices given in Appendix B.2 and Appendix D.1, except, $\boldsymbol{A_{PDC}} = \boldsymbol{0}_{5\times 7}$ and $\boldsymbol{B_{PDC}} = \boldsymbol{0}_{5\times 1}$.

5.2.3 Virtual admittance block

The dynamics of virtual admittance can be represented by (4.3)-(4.4) as mentioned in section 4.2.1. The linearized representation of (4.3)-(4.4) with dc-side configuration B is given by (5.15).

$$\begin{bmatrix} \Delta {i_{\mathrm{cvd}}}^* \\ \Delta {i_{\mathrm{cvq}}}^* \end{bmatrix} = \boldsymbol{A_{icvdqrefDC}\Delta X_{DC}} + \boldsymbol{A_{icvdqrefP}\Delta X_P} + \boldsymbol{A_{icvdqrefLCL}\Delta X_{LCL}} + \boldsymbol{B_{icvdqref}\Delta U_{gfm}} \quad (5.15)$$

The expanded form of $\boldsymbol{A_{icvdqrefLCL}}$ is the same as in Appendix D.2. The expanded form of $\boldsymbol{A_{icvdqrefP}}$ and $\boldsymbol{B_{icvdqref}}$ are v_{dc0} times the corresponding matrices in Appendix D.2. Here, v_{dc0} is the per unitized dc-link voltage from configuration B at the considered operating point. Appendix F.2 gives $\boldsymbol{A_{icvdqrefDC}}$.

5.2.4 Decoupled current controller

The dynamics of the decoupled current controller can represented using (4.6)-(4.7) in section 4.2.1. The linearized representation with the dc-side configuration B is shown in (5.16).

$$\boldsymbol{\Delta \dot{X}_{CC}} = \boldsymbol{A_{CCDC}\Delta X_{DC}} + \boldsymbol{A_{CCP}\Delta X_{P}} + \boldsymbol{A_{CC}\Delta X_{CC}} + \boldsymbol{A_{CCLCL}\Delta X_{LCL}} + \boldsymbol{A_{CCN}\Delta X_{N}} + \boldsymbol{A_{CCL}\Delta X_{L}} + \boldsymbol{B_{CC}\Delta U_{gfm}} + \boldsymbol{B_{CCDC}\Delta U_{DC}} \quad (5.16)$$

By considering the expanded forms of matrices in (5.15), the expanded forms of matrices in (5.16) can be obtained similar to Appendix D.3, except, $\boldsymbol{A_{CCDC}} = \boldsymbol{A_{icvdqrefDC}}$ and $\boldsymbol{B_{CCDC}} = \boldsymbol{0}_{2\times 1}$.

5.2.5 LC filter and transformer

Similar to section 4.2.1, the linearized representation of this component can be obtained as shown in (5.17) for the dc-side configuration B embedded scenario.

$$\boldsymbol{\Delta \dot{X}_{LCL}} = \boldsymbol{A_{LCLDC}\Delta X_{DC}} + \boldsymbol{A_{LCLP}\Delta X_{P}} + \boldsymbol{A_{LCLCC}\Delta X_{CC}} + \boldsymbol{A_{LCL}\Delta X_{LCL}} + \boldsymbol{A_{LCLN}\Delta X_{N}} + \boldsymbol{A_{LCLL}\Delta X_{L}} + \boldsymbol{B_{LCL}\Delta U_{gfm}} + \boldsymbol{B_{LCLDC}\Delta U_{DC}} \quad (5.17)$$

The expanded forms of matrices in (5.17) can be obtained as shown in Appendix D.4 while incorporating the changes introduced by (5.15). The expanded forms of $\boldsymbol{A_{LCLDC}}$ and $\boldsymbol{B_{LCLDC}}$ are given in Appendix F.3.

5.2.6 Network

The linearized model of this component can be obtained as mentioned in section 4.2.1. The small-signal model for the dc-side configuration B embedded scenario can be represented as

(5.18).

$$\Delta\dot{\boldsymbol{X}}_{\mathbf{N}} = \boldsymbol{A}_{\mathbf{NDC}}\Delta\boldsymbol{X}_{\mathbf{DC}} + \boldsymbol{A}_{\mathbf{NP}}\Delta\boldsymbol{X}_{\mathbf{P}} + \boldsymbol{A}_{\mathbf{NCC}}\Delta\boldsymbol{X}_{\mathbf{CC}} + \boldsymbol{A}_{\mathbf{NLCL}}\Delta\boldsymbol{X}_{\mathbf{LCL}} + \boldsymbol{A}_{\mathbf{N}}\Delta\boldsymbol{X}_{\mathbf{N}} + \boldsymbol{A}_{\mathbf{NL}}\Delta\boldsymbol{X}_{\mathbf{L}} + \boldsymbol{B}_{\mathbf{N}}\Delta\boldsymbol{U}_{\mathbf{gfm}} + \boldsymbol{B}_{\mathbf{NDC}}\Delta\boldsymbol{U}_{\mathbf{DC}} \quad (5.18)$$

The expanded forms of matrices can be found in Appendix B.4 and Appendix D.5, except, $\boldsymbol{A}_{\mathbf{NDC}} = \boldsymbol{0}_{4\times7}$ and $\boldsymbol{B}_{\mathbf{NDC}} = \boldsymbol{0}_{4\times1}$.

The overall state equation for the components above in the GFM inverter's reference frame can be represented as shown in (5.19).

$$\Delta\dot{\boldsymbol{X}}_{\mathbf{gfm}} = \boldsymbol{A}_{\mathbf{gfm}}\Delta\boldsymbol{X}_{\mathbf{gfm}} + \boldsymbol{A}_{\mathbf{gfmsm}}\Delta\boldsymbol{X}_{\mathbf{sm}} + \boldsymbol{A}_{\mathbf{gfmLoad}}\Delta\boldsymbol{X}_{\mathbf{L}} + \boldsymbol{B}_{\mathbf{gfm}}\Delta\boldsymbol{U}_{\mathbf{gfm}} + \boldsymbol{B}_{\mathbf{gfmDC}}\Delta\boldsymbol{U}_{\mathbf{DC}} \quad (5.19)$$

Here,

$$\Delta\boldsymbol{X}_{\mathbf{gfm}} = \begin{bmatrix} \Delta\boldsymbol{X}_{\mathbf{DC}} & \Delta\boldsymbol{X}_{\mathbf{P}} & \Delta\boldsymbol{X}_{\mathbf{CC}} & \Delta\boldsymbol{X}_{\mathbf{LCL}} & \Delta\boldsymbol{X}_{\mathbf{N}} \end{bmatrix}^{\mathrm{T}}$$

$$\boldsymbol{A}_{\mathbf{gfm}} = \begin{bmatrix} \boldsymbol{A}_{\mathbf{DC}} & \boldsymbol{A}_{\mathbf{DCP}} & \boldsymbol{A}_{\mathbf{DCCC}} & \boldsymbol{A}_{\mathbf{DCLCL}} & \boldsymbol{A}_{\mathbf{DCN}} \\ \boldsymbol{A}_{\mathbf{PDC}} & \boldsymbol{A}_{\mathbf{P}} & \boldsymbol{A}_{\mathbf{PCC}} & \boldsymbol{A}_{\mathbf{PLCL}} & \boldsymbol{A}_{\mathbf{PN}} \\ \boldsymbol{A}_{\mathbf{CCDC}} & \boldsymbol{A}_{\mathbf{CCP}} & \boldsymbol{A}_{\mathbf{CC}} & \boldsymbol{A}_{\mathbf{CCLCL}} & \boldsymbol{A}_{\mathbf{CCN}} \\ \boldsymbol{A}_{\mathbf{LCLDC}} & \boldsymbol{A}_{\mathbf{LCLP}} & \boldsymbol{A}_{\mathbf{LCLCC}} & \boldsymbol{A}_{\mathbf{LCL}} & \boldsymbol{A}_{\mathbf{LCLN}} \\ \boldsymbol{A}_{\mathbf{NDC}} & \boldsymbol{A}_{\mathbf{NP}} & \boldsymbol{A}_{\mathbf{NCC}} & \boldsymbol{A}_{\mathbf{NLCL}} & \boldsymbol{A}_{\mathbf{N}} \end{bmatrix}$$

$$\boldsymbol{A}_{\mathbf{gfmLoad}} = \begin{bmatrix} \boldsymbol{A}_{\mathbf{DCL}} & \boldsymbol{A}_{\mathbf{PL}} & \boldsymbol{A}_{\mathbf{CCL}} & \boldsymbol{A}_{\mathbf{LCLL}} & \boldsymbol{A}_{\mathbf{NL}} \end{bmatrix}^{\mathrm{T}}$$

$$\boldsymbol{B}_{\mathbf{gfm}} = \begin{bmatrix} \boldsymbol{B}_{\mathbf{DCgfm}} & \boldsymbol{B}_{\mathbf{P}} & \boldsymbol{B}_{\mathbf{CC}} & \boldsymbol{B}_{\mathbf{LCL}} & \boldsymbol{B}_{\mathbf{N}} \end{bmatrix}^{\mathrm{T}}$$

$$\boldsymbol{B}_{\mathbf{gfmDC}} = \begin{bmatrix} \boldsymbol{B}_{\mathbf{DC}} & \boldsymbol{B}_{\mathbf{PDC}} & \boldsymbol{B}_{\mathbf{CCDC}} & \boldsymbol{B}_{\mathbf{LCLDC}} & \boldsymbol{B}_{\mathbf{NDC}} \end{bmatrix}^{\mathrm{T}}$$

$$\boldsymbol{A}_{\mathbf{gfmsm}} = \boldsymbol{0}_{24\times16}$$

The linearization of the synchronous machine and the load components in section 3.3 will be

intact in the presence of the virtual admittance-based inner current controller and the dc-side configuration B. Therefore, the overall system's state matrix can be obtained similarly to section 3.3.7.

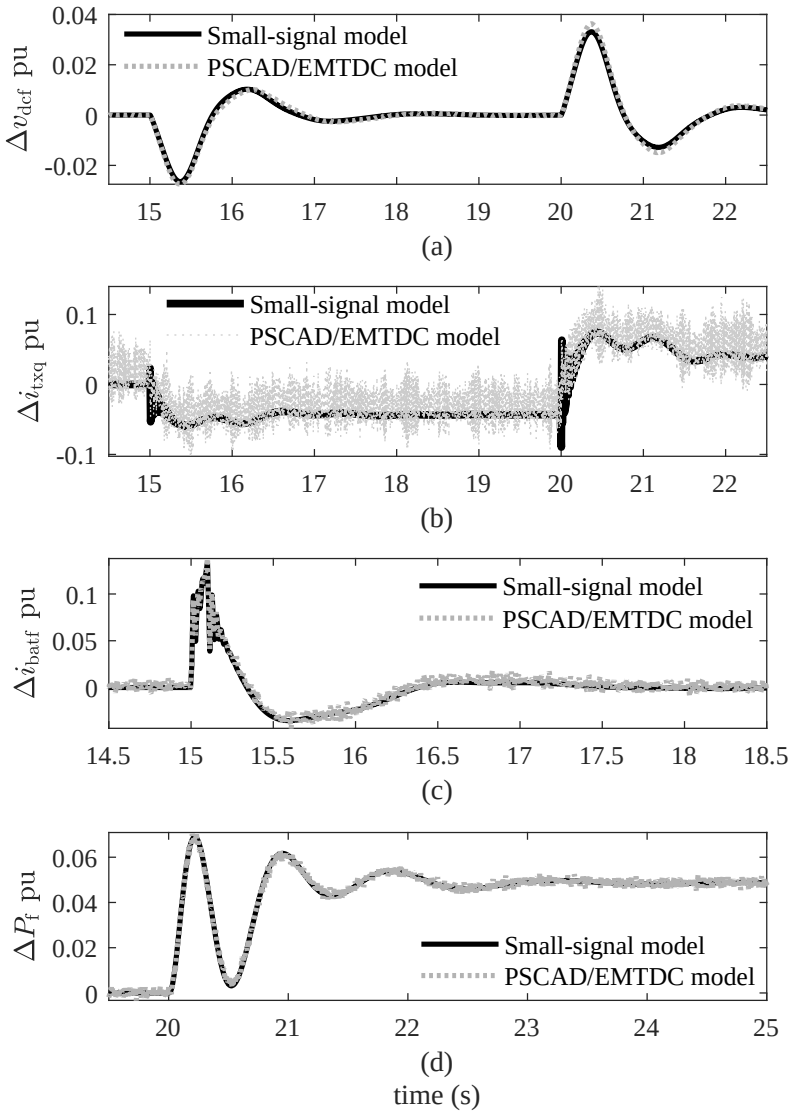

Fig. 5.3: Small-signal model vs EMT responses for (a) ΔR_{L} = -10% at t = 15 s and ΔR_{L} = 2.5% at t = 20 s, (b) ΔR_{L} = -10% at t = 15 s and ΔR_{L} = 10% at t = 20 s (c) $\Delta v_{\mathrm{dcref}}$=10% at t = 15 s for 0.1 s and (d) $\Delta P_{\mathrm{gfmref}}$ = 0.1 pu of GFM inverter at t = 20 s.

5.2.7 Small-signal model validation

The small-signal model with the dc-side configuration B is validated against the detailed EMT model in PSCAD/EMTDC. The responses obtained from the linearized and detailed

EMT models at the operating point specified in section 5.1, with SCR = 2, when the GFM inverter is 90% loaded, and when the GFM inverter is in charging mode are given in Figs. 5.3(a), 5.3(b), 5.3(c), and 5.3(d), respectively. These tests and others (not shown for brevity) confirm that the developed small-signal model can track the low-frequency oscillation of the EMT model for adequately small disturbances around an operating point.

5.3 Eigenvalue Analysis

A comparative eigenvalue analysis is carried out considering the two dc-side configurations. Four critical modes are identified for dc-side configuration A in section 4.3.1. An additional two oscillatory modes (modes 5 and 6) are introduced by the dc-side configuration B. Fig. 5.4 depicts the locus of identified critical modes using white and black markers for dc-side configuration A and B, respectively, and Table 5.2 lists major participants in the six critical modes identified for dc-side configuration B. The mode-shapes for the identified six critical modes with the dc-side configuration B are given in Fig. 5.5.

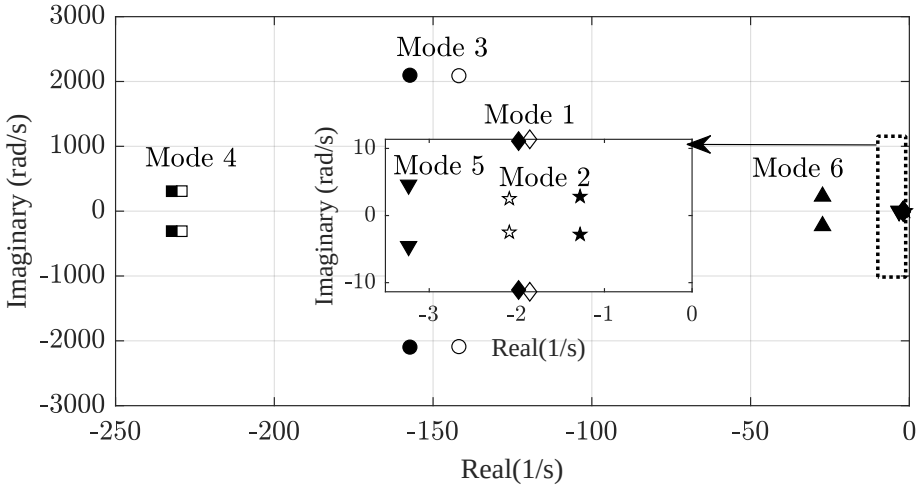

Fig. 5.4: Locus of eigenvalues corresponding to the critical modes with dc-side configuration A (white markers) and dc-side configuration B (black markers).

Table 5.2: Major Participants in the Critical Modes of Configuration B

Mode	**Freq** (Hz)	**ζ** (%)	**Major Participants**
1	1.80	14.2	δ[100%], ω_{sm}[61%], ω_{gfm}[46%]
2	0.40	29.0	x_8[100%], T_{m}[62%], x_2[47%], x_1[39%], v_{dc}[39%], ω_{sm}[38%]
3	49.0	60	i_{cvd}[100%], i_{cvq}[99%], x_4[65%], x_5[64%], i_{d}[42%], i_{q}[42%]
4	333.7	7.5	v_{fq}[100%], v_{fd}[100%], i_{cvq}[66%], i_{cvd}[66%], i_{tq}[52%], i_{td}[52%]
5	0.70	60.0	v_{dc}[100%], x_8[79%], ω_{gfm}[60%], ψ_{fd}[39%], ω_{sm}[37%], T_{m}[34%], x_2[31%]
6	36.2	12.5	i_{bat}[100%], i_{batf}[94%]

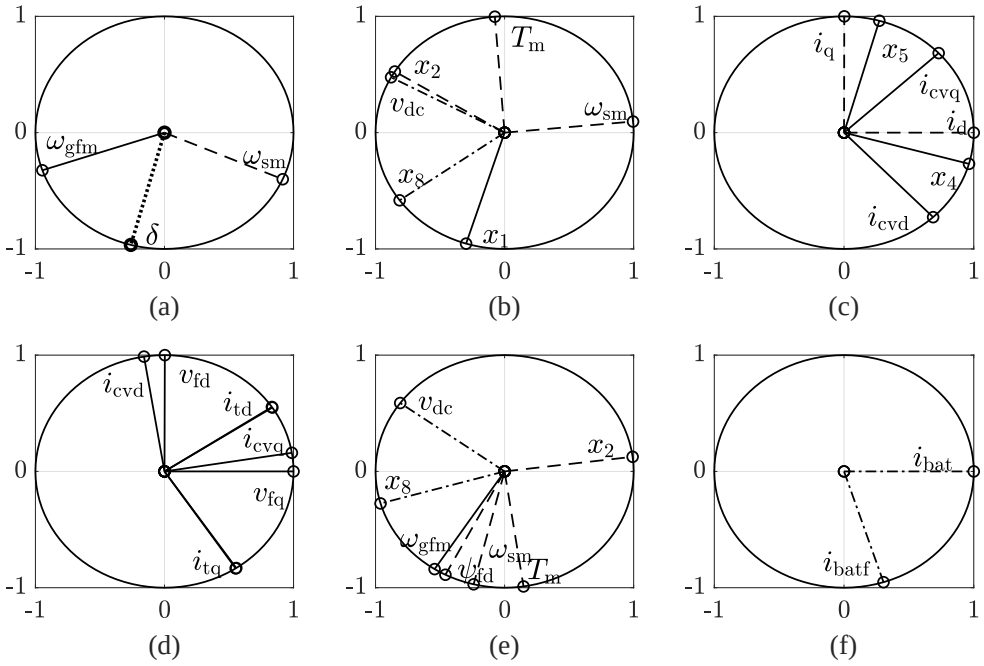

Fig. 5.5: Mode shapes of major participants in dc-side config. B from GFM inverter (solid), synchronous machine (dashed), both GFM inverter and synchronous machine (doted) and dc side (dash-dot) for (a) mode 1, (b) mode 2, (c) mode 3,(d) mode 4, (e) mode 5 and (f) mode 6.

As shown in Fig. 5.4, modes 1-4 are common between the two dc-side configurations. Participation factor analysis for modes 1,3, and 4 of both dc-side configurations shows a similar set of major participants as reflected in Table 5.2. This reveals that for the tested conditions, the dc-side dynamics do not interact with these relatively high-frequency modes. The mode shape diagram for mode 1 in Fig. 5.5a shows the virtual electromechanical

interaction identified in section 4.3.1. Fig. 5.5c and 5.5d show the two network modes corresponding to modes 3 and 4 in section 4.3.1.

DC-side configuration B introduces major participants from dc-side circuitry and its controller to mode 2 compared to dc-side configuration A as shown in Fig. 5.6. This discloses possible interactions between the dc-side circuitry and its associated controller with the synchronous machine and its governor-turbine system. This clearly shows that proper modeling of the dc-side circuitry and controller is vital in capturing all the root causes of interactions in a GFM inverter system. The mode shape diagram for mode 2 in Fig. 5.5b confirms possible interaction between the dc-side circuitry and the synchronous machine. Both modes 2 and 5 have a similar set of significantly participating state variables while mode 5 is well damped compared to mode 2. The mode shape diagram for mode 5 in Fig. 5.5e shows possible interactions between the dc-side controller and the governor-turbine system of the synchronous machine. Therefore, modes 2 and 5 are identified as controller modes. Mode 6 is a controller mode that has major participants from the dc-side circuitry and its controller. Eigenvalue analysis identifies mode 6 as a critical mode due to its low damping.

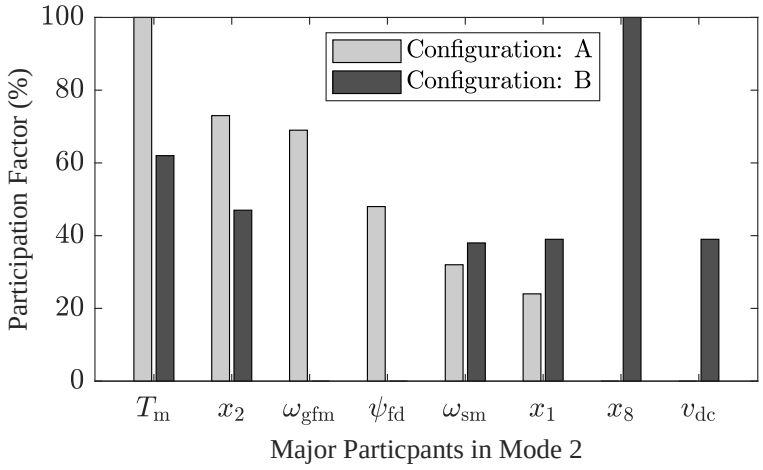

Fig. 5.6: Comparison of major participants in mode 2 with dc-side configurations A and B.

The following sections analyze the sensitivity of the identified critical modes to dc-side and GFM controller parameters. According to participation factor analysis, the electrome-

chanical characteristics of the synchronous machine, LC filter parameters, and control parameters of the virtual admittance block and the decoupled current controller also affect the six critical modes. However, as this study's main focus is to demonstrate the effect of the dc-side dynamics in GFM inverter systems, the presented sensitivity analysis is limited to the following list.

- Effect of dc-side parameters.
- Effect of GFM controller parameters.
- Effect of both dc-side and GFM controller parameters.

5.3.1 Effect of dc-side parameters

The dc-side circuitry and controller parameters are varied to identify their effect. The integral time constants of the dc-link voltage loop and the dc-source current loop controllers were changed over $[0.02, 0.8]$ s and $[0.01, 0.4]$ s, respectively, to obtain both fast- and slow-acting dc-side controllers. Similarly, L_{bat} and C_{dc} were changed from over $[0.005, 0.2]$ H and $[0.0015, 0.06]$ F, respectively, to create high to low bandwidths.

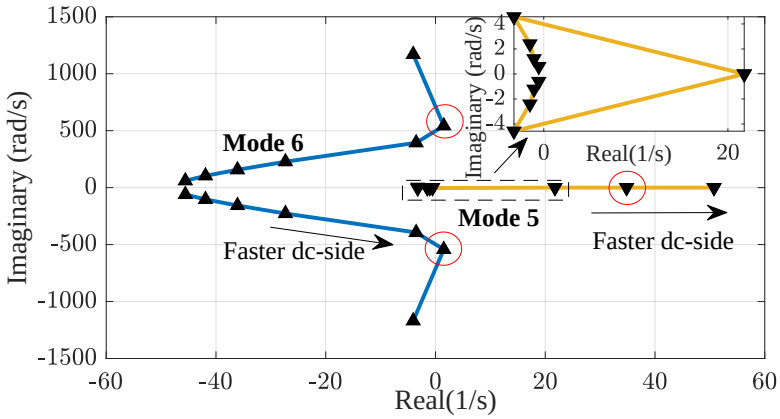

Fig. 5.7: Locus of critical eigenvalues corresponding to modes 5 and 6 for changes in dc-side dynamics.

The locus of the eigenvalues corresponding to the six critical modes reveals that for the given GFM controller, the effects of the dc-side dynamics on modes 1 to 4 are negligible

(not shown for brevity). However, modes 5 and 6 reach instability with fast-acting dc-side circuitry as shown in Fig. 5.7. Participation factor analysis at the unstable operating points reveals that these instabilities are indeed due to the dc-side controller and circuitry interactions. For the operating point marked with red circles in Fig. 5.7, PSCAD/EMTDC simulation results are shown in Fig. 5.8 for a 0.1 pu V_{dcref} pulse of 0.1 s. The traces verify the negatively damped, aggressive battery current oscillation and its interactions with the dc-link voltage.

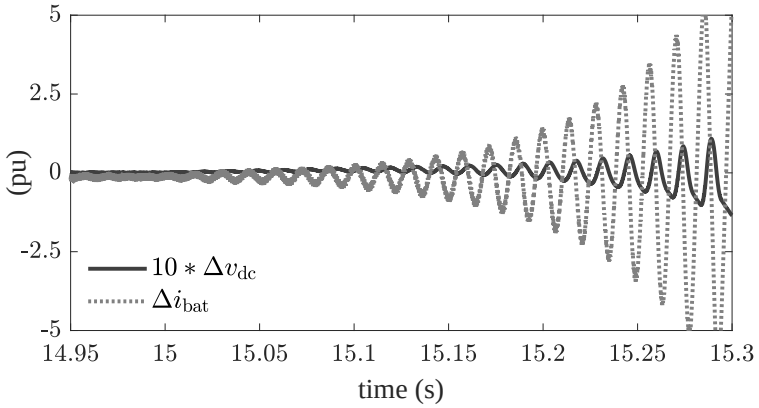

Fig. 5.8: PSCAD/EMTDC simulation results for the considered example case to demonstrate dc-side circuitry interactions.

5.3.2 Effect of GFM controller parameters

GFM controller dynamics are mainly governed by its virtual inertia time constant (H_{gfm}) and the integral time constant (T_i) of the Q-v controller path. Therefore, to obtain fast-acting to slow-acting GFM inverters, H_{gfm} and T_i are varied over $[0.3, 7.5]$ s and $[0.025, 0.625]$ s, respectively.

The eigenvalues' movement of six critical modes shows that modes 3, 4, and 6 are least affected by GFM controller dynamics. This is due to the absence of GFM controller states' participation in these three critical modes. However, modes 1, 2, and 5 are significantly affected by the dynamics of the GFM controller, and the corresponding traces are given in Fig. 5.9. The arrow in each graph shows the direction of the corresponding parameter's

increment.

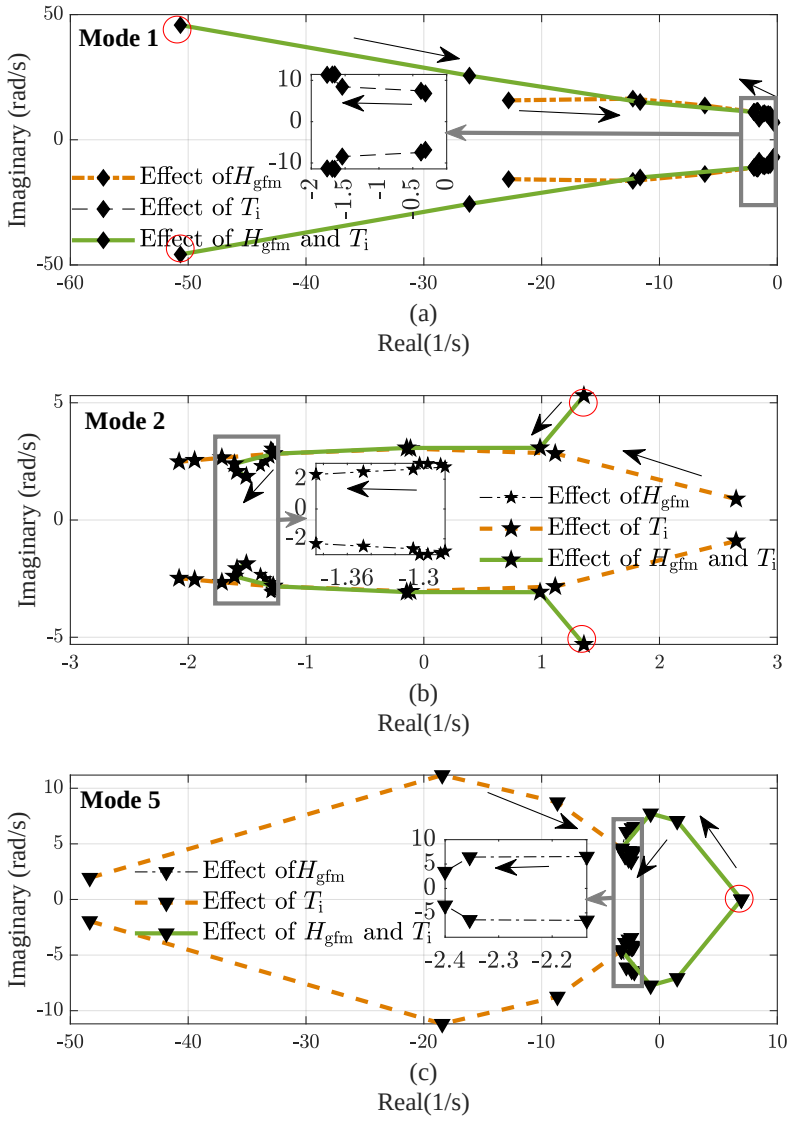

Fig. 5.9: Locus of critical eigenvalues corresponding to modes (a) 1, (b) 2, and (c) 5 for changes in GFM controller dynamics.

As shown in Fig. 5.9(a), mode 1 is highly sensitive to the virtual inertia time constant (H_{gfm}). The increment of the virtual inertia time constant has reduced the damping of mode 1. This behavior is also observed with dc-side configuration A (section 3.4.1). Large virtual inertia time constants bring the dynamics of the GFM inverter close to the sluggish governor-turbine-equipped synchronous machine's dynamics. Therefore the tendency to interact between these two sources increases. This is the reason for the compromised damping

of mode 1 for high virtual inertia time constant values.

As shown in Figs. 5.9(b) and 5.9(c), modes 2 and 5 are highly sensitive to Q-v controller dynamics. Fast-acting GFM controllers bring the system to instability. The participation factor and mode shape analysis (not shown for brevity) at the unstable operating points reveal that mainly the interaction between Q-v controller and dc-link voltage has led to system instability. The instability of mode 2 with a fast-acting GFM controller was not observed with dc-side configuration A (section 3.4.3), whereas mode 5 is not modeled in configuration A. Therefore, this analysis clearly shows the importance of considering dc-side dynamics in selecting GFM controller parameters for a given dc-side configuration. Considering the operating point marked with red circles in Fig. 5.9, PSCAD/EMTDC responses are obtained for a 0.1 pu pulse applied to ω_{gfmref} at $t = 15$ s for 0.1 s. The undamped response of Q-v controller state, x_1 in Fig. 5.10 verifies the predictions of eigenvalue analysis.

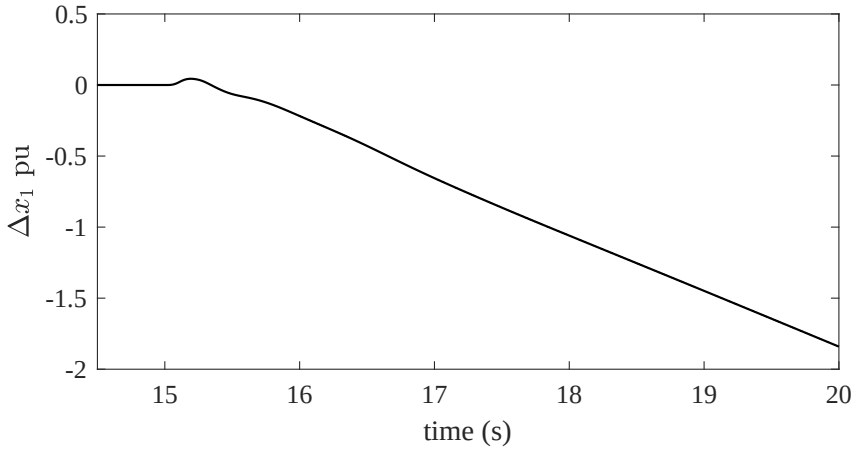

Fig. 5.10: PSCAD/EMTDC simulation results for the considered example case to demonstrate system instability.

Generally, dc-side dynamics are to be aligned with the GFM controller's dynamics to achieve the desired power balance between the dc and ac sides. Therefore, these sensitivity analyses are extended by incorporating matching GFM controller's bandwidths with each

dc-side's bandwidth considered.

5.3.3 Effect of both dc-side and GFM controller parameters

The overall performance of the GFM inverter depends on the dynamics of its dc-side and the associated GFM controller's dynamics. Therefore, the changes in sections 5.3.1 and 5.3.2 are carried out simultaneously to obtain fast-acting to slow-acting GFM inverters. The control and network parameters used in each of the test scenarios are given in Table 5.3. Figs. 5.11a and 5.11b show the locus of eigenvalues corresponding to modes 1-3 and modes 4-6 with the changes in GFM inverter (both dc and ac sides) dynamics. They clearly show that fast-acting GFM controllers accompanied by fast-acting dc-sides can easily bring the system towards instability.

Table 5.3: The Network and Control Parameters at each Test Scenario

Parameter	**Values at Test Scenarios**						
	1	2	3	4	5	6	7
L_{bat} (mH)	5	7.5	10	25	50	100	200
C_{dc} (mF)	1.5	2.5	3	7.5	15	30	60
T_{ivdc} (s)	0.02	0.03	0.04	0.1	0.2	0.4	0.8
T_{iibat} (s)	0.01	0.015	0.02	0.05	0.1	0.2	0.4
H_{gfm} (s)	0.3	0.6	1.2	3	4.5	6	7.5
T_{i} (s)	0.025	0.05	0.1	0.25	0.375	0.5	0.625

Participation factor and mode shape analysis at unstable operating points reveal that a fast-acting dc-side can easily interact with the GFM controller, synchronous machine, and LC filter. The exemplar operating point that is marked with red circles in Figs. 5.11(a) and 5.11(b) corresponds to test scenario 1. The mode shape diagrams for the unstable modes (i.e., modes 2, 4, and 5) at this operating condition are given in Fig. 5.12.

As shown in Fig. 5.12a, mode 2 has reached instability with the interaction between the governor-turbine system and the dc-side controller. Fig 5.12b shows that the interaction between the dc-side and the LC filter components has made mode 4 unstable. The mode shape diagram for mode 5 in Fig. 5.12c shows that the dc-side's interactions with the

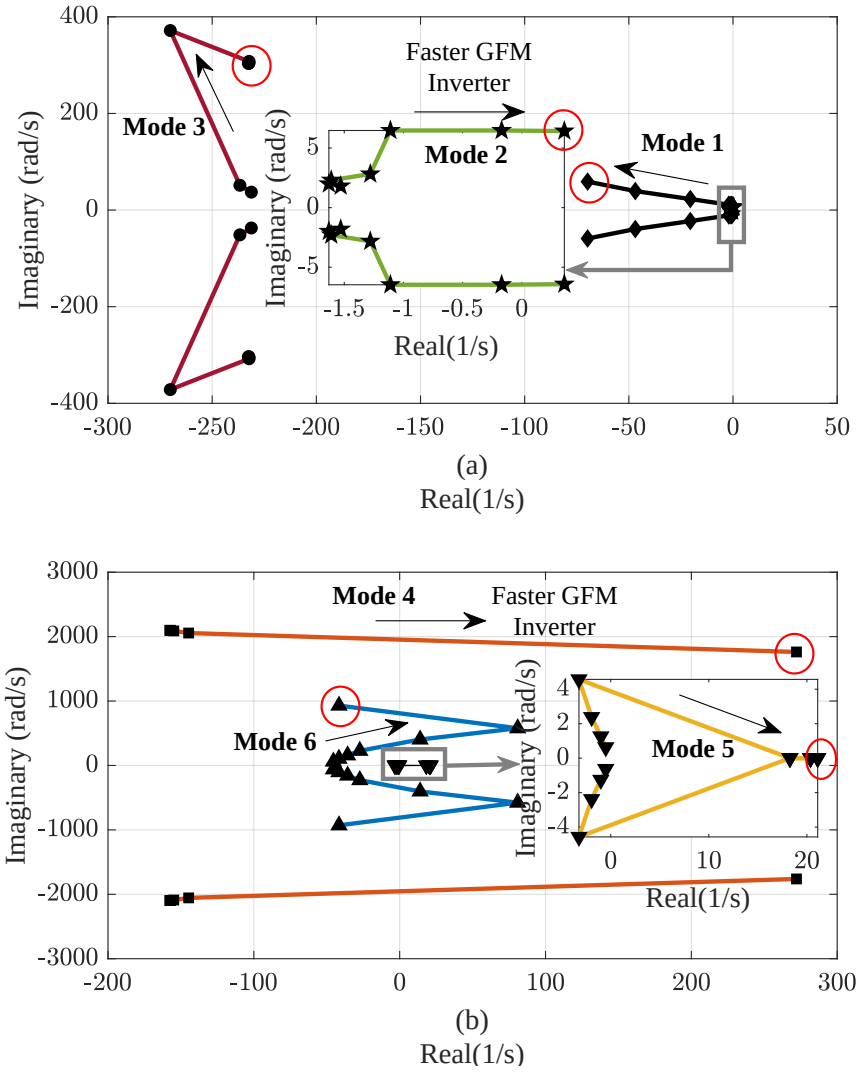

Fig. 5.11: Locus of critical eigenvalues corresponding to (a) mode 1-3, (b) mode 4-6 for changes in GFM inverter dynamics.

GFM controller push the system to instability. This clearly shows the ample possibilities of interactions between the dc-side and the rest of the network and control blocks. For the same exemplar operating point, the responses obtained from PSCAD/EMTDC for a 0.1 pu V_{dcref} pulse of 0.1 s at $t = 15$ s is given in Fig. 5.13. This verifies the existence of adverse interaction between the dc-side circuitry and the LC filter components.

Participation factor analysis is conducted for all six critical modes in each test scenario. Then the percentage of participation from dc-side states in each oscillatory mode at each

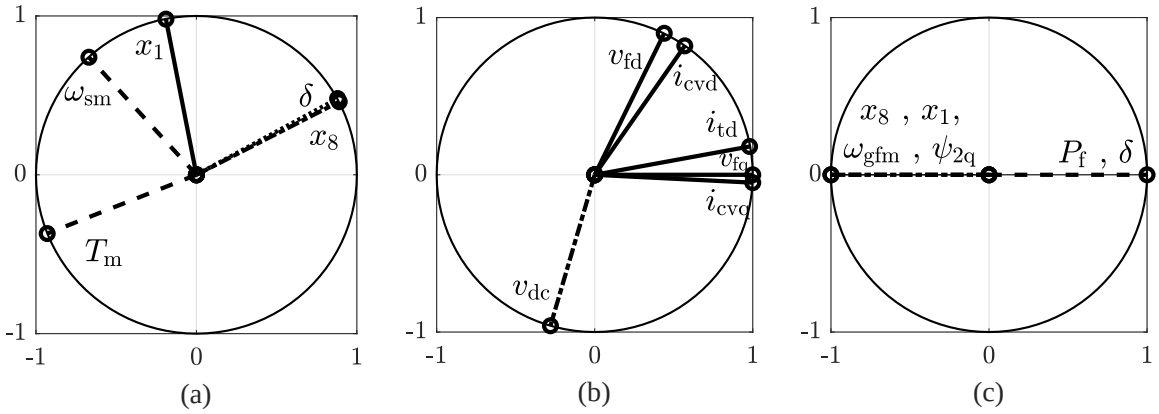

Fig. 5.12: Mode shapes of major participants for the considered example case from GFM inverter (solid), synchronous machine (dashed), GFM inverter and synchronous machine (dotted) and dc side (dash-dot) for (a) mode 2, (b) mode 4, and (c) mode 5.

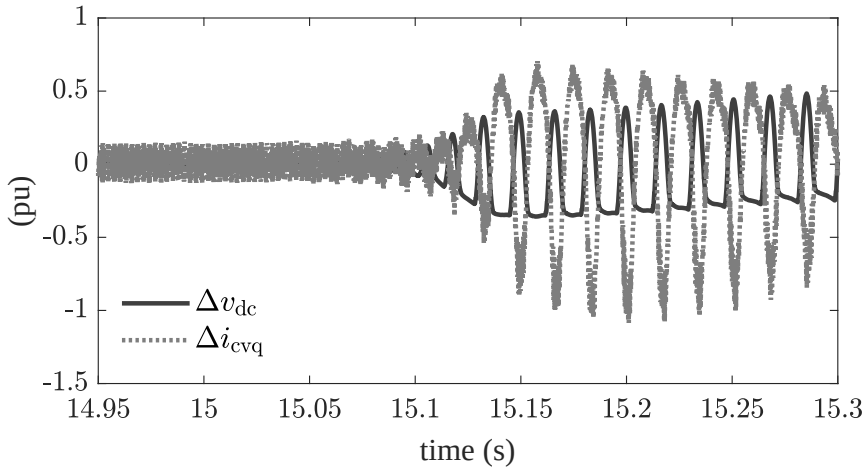

Fig. 5.13: PSCAD/EMTDC simulation results for the considered example case to demonstrate the dc-side circuitry and the LC filter components interactions.

tested condition is calculated and presented in Fig.5.14. As shown the dc-side significantly participates in all modes in fast-acting GFM inverters. However, with slow-acting GFM inverters (Test Scenarios 6-7) the dc-side participation is greatly reduced in modes 1 to 4 and is limited to appear in modes 5 and 6. Modes 1 to 4 appeared even in dc-side configuration A (i.e., with an ideal dc source). Modes 5 to 6 were introduced by dc-side configuration B (i.e., with bi-directional dc-dc converter and dc-side controller). Therefore, under such sluggish GFM inverter conditions, the GFM inverter can be modeled without paying attention to dc-side dynamics. However, the control and network parameters corresponding to test scenarios

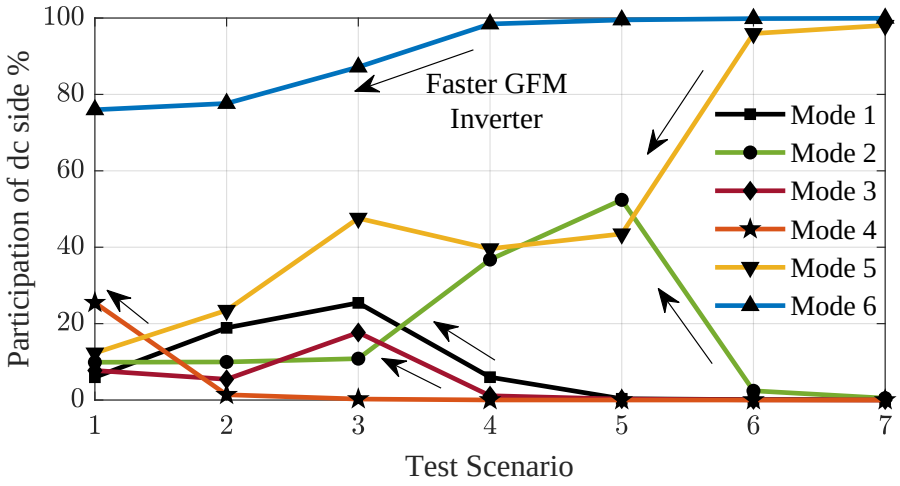

Fig. 5.14: The participation of dc-side state variables in each critical mode for each test scenario.

6 and 7 give the GFM inverter an extremely sluggish action. This jeopardizes the fast-acting capability of power-electronic inverters. Therefore, for the practical operating range of GFM inverters, the dc-side dynamics are required to be modeled in order to capture the full range of interactions that can happen in a GFM inverter system.

To analyze the validity of the results, the same sensitivity study is conducted with different short circuit ratios, different loading levels of GFM inverter, and different charging levels of GFM Inverter. The tested operating conditions and the system's stability are summarized in Table 5.4.

Table 5.4: Effect of GFM Inverter Parameters under Different Operating Conditions

Operating Condition	**Operating Condition-Specific Parameters**	**Stability at Test Scenarios**			
		1	2	3	4- 7
SCR = 7	tx line length = 5 km	Unstable Modes: 5,6	Unstable Modes: 5,6	Unstable Modes: 5,6	Stable
SCR = 5	tx line length = 10 km	Unstable Modes: 2,4,5	Unstable Modes: 5,6	Unstable Modes: 5,6	Stable
SCR = 2	tx line length = 40 km	Unstable Modes: 2,4,5	Unstable Modes: 4,5,6	Unstable Modes: 5,6	Stable
GFM Inv. 50% Loaded	$P_{\text{gfmref}} = 0.5$ pu, $P_{\text{smref}} = 0.9$ pu	Unstable Modes: 2,5,6	Unstable Modes: 2,5,6	Unstable Modes: 5,6	Stable
GFM Inv. 70% Loaded	$P_{\text{gfmref}} = 0.7$ pu, $P_{\text{smref}} = 0.7$ pu	Unstable Modes: 2,4,5	Unstable Modes: 5,6	Unstable Modes: 5,6	Stable
GFM Inv. 90% Loaded	$P_{\text{gfmref}} = 0.9$ pu,$P_{\text{smref}} = 0.5$ pu	Unstable Modes: 5,6	Unstable Modes: 5,6	Unstable Modes: 5,6	Stable
Charging Level 10%	$P_{\text{gfmref}} =$ -0.1 pu, $P_{\text{smref}} = 0.8$ pu $R_{\text{L}} = 110.62\ \Omega$, $L_{\text{L}} = 0.58$ H	Unstable Modes: 5,6	Unstable Modes: 5,6	Unstable Modes: 1,5,6	Stable
Charging Level 20%	$P_{\text{gfmref}} =$ -0.2 pu, $P_{\text{smref}} = 0.9$ pu $R_{\text{L}} = 110.62\ \Omega$, $L_{\text{L}} = 0.58$ H	Unstable Modes: 5,6	Unstable Modes: 5,6	Unstable Modes: 1,5,6	Stable

As shown, the extensive studies on different operating conditions verify that fast-acting GFM inverters have limited stability. Participation factor and mode shape analyses (not shown for brevity) at these unstable modes show possible interactions between dc-side controller and dc-side circuitry, dc-side and GFM controller, dc-side and governor-turbine system and dc-side and LC filter components. This verifies the robustness of the study results even under different operating conditions.

5.4 Summary

This chapter analyzed the effects of GFM inverter's dc-side dynamics on interactions. The dc-side dynamics were introduced by a dc-source connected via a bidirectional dc-dc converter and the dc-side controller. Eigenvalue analysis revealed the significant presence of dc-side dynamics in a wide range of inverter and grid operating conditions. Therefore, the inclusion of dc-side dynamics during the controller design stage and the system studies stage is necessary. The list of contributions of this chapter is mentioned below.

- Development and validation of a small-signal model for an exemplar system of a GFM inverter paralleled with a synchronous machine by including the full dynamics of the dc-side circuitry, VSM layer, current limiter, network, and synchronous machine.
- Computation and comparison of the system eigenvalues with and without the dc-side dynamics to highlight the importance of modeling the dc-side dynamics.
- Identification of possible dc-side interactions with the GFM controller, ac network components, and synchronous machine.
- Detailed analysis of the role of operating conditions on the dc-side's impact on system stability.

Chapter 6

Conclusions, Contributions and Future Work

GFM controller is a promising converter-control method, which provides controllability over the converter terminal's voltage and frequency through power modulations. There are numerous GFM controller topologies in the literature. However, there existed a research gap in identifying the root causes of interactions that can be excited by a GFM controller. Therefore, in this research, a small-signal model-based eigenvalue analysis was conducted on commonly used GFM controller topologies with different ac and dc side system configurations to reveal the full causes of interactions that can happen in a GFM inverter system. The overall conclusions drawn from the study are mentioned in section 6.1. The key contributions made by the study are given in section 6.2. Recommendations for future work are given in section 6.3.

6.1 Conclusions

A summary of major conclusions are given below.

- The GFM controller's topology, GFM controller parameters, ac network configuration,

dc-side circuitry, and dc-side controller lead to interactions that spread over a wide frequency range. Inter-machine interactions (virtual electromechanical interactions), controller interactions and network interactions were identified during the study.

- A GFM controller with low bandwidth outer power controller that emulates inertial and primary frequency responses of a synchronous machine can lead to virtual electromechanical interactions between GFM inverters with similar outer control layers or synchronous machines. The small virtual inertia time constants and small $\Delta f/\Delta P$ co-efficient values improve the damping of those inter-machine interactions.

- The utilization of decoupled current controller in the GFM controller can lead to high frequency network interactions. However, with the help of a virtual impedance with large X/R ratio, the damping of the network mode can be improved. This concludes the necessity to consider network dynamics and full dynamics of the GFM controller in stability analysis studies of GFM inverter systems.

- Even if an arbitrary selection of GFM controller parameters is granted, the dc-side dynamics dictate the range of values that can be used.

- The fast-acting GFM controller accompanied by the fast-acting dc-side can reduce the stability due to interactions between dc-side and GFM controller, dc-side and LC filter components, and dc-side and governor-turbine system. Therefore, though a generic dc-side representation was considered in the study, it showed the importance of considering dc-side dynamics, especially during the controller design and system studies stages.

This study broadened the interaction analysis of GFM inverter systems by including dynamics of GFM controller, ac-side, and dc-side of the GFM inverter system. The key driving factors behind the critical interactions in the GFM inverter system were revealed using eigenvalue analysis and verified by PSCAD/EMTDC simulation results. Therefore, the extensive information derived from this study can be logically applied to large networks.

6.2 Contributions

The key contributions of the study are as follows.

- Development and validation of small-signal models for the following scenarios to accommodate the step-by-step expansion of the dynamics to be considered in the study. Parallel connected two GFM inverters in the islanded mode: Consider dynamics of the VSM layer and transient virtual impedance (no-loop current controller) and network. GFM inverter in parallel with a synchronous machine: Consider dynamics of the VSM layer, the no-loop and two of the multi-loop current controllers, synchronous machine (including exciter and governor-turbine systems), network, dc-side circuitry, and dc-side controller.

- Identification of root causes for the virtual electromechanical interactions that can be excited by the low-bandwidth layer of the GFM controller (i.e., VSM layer) as high virtual inertia time constant and high $\Delta f/\Delta P$ co-efficient.

- Revealing the reason for the contrary effect from inertia time constant and P-f droop co-efficient of GFM inverter and synchronous machine as the explicit sluggish governor-turbine system in the synchronous machine model.

- Demonstration of the ability of high-bandwidth inner control layers to excite the network modes while having a negligible impact on the virtual electromechanical and governor modes.

- Revealing and verification of the effect of virtual impedance on the network and virtual electromechanical modes.

- Showing the ability of the considered current-limiting methods to limit the fault current well below 2.0 pu in systems consisting of only GFM inverters and a GFM inverter in parallel with a synchronous machine.

- Comparative eigenvalue analysis with and without dc-side dynamics to demonstrate the importance of considering dc-side dynamics in GFM inverter systems during the controller designing and system studies stage.

- Revealing possible interactions between dc-side circuitry and dc-side controller, dc-side and GFM controller and dc-side and network.

These contributions have led to the following publications;

1. T. Thilekha, S. Filizadeh, U. Annakkage, C. Karawita, and D. Muthumuni, "Effect of DC-Side Dynamics on Interactions in Grid-Forming Inverter Systems", *IEEE Trans. Energy Convers.*, to appear.

2. T. Thilekha, S. Filizadeh, U. Annakkage, C. Karawita, and D. Muthumuni, "Grid-Forming Inverter Interaction Studies Using Small-Signal Stability Assessment," in *Proc. CIGRE Canada Conf. Expo*, (Manitoba, Canada), Oct. 2024.

3. T. Thilekha, S. Filizadeh, U. Annakkage, C. Karawita, and D. Muthumuni, "Analysis of interactions among parallel grid forming inverters," *Electric Power Syst. Res.*, vol. 223, p. 109652, Oct. 2023.

4. T. Thilekha, S. Filizadeh, U. Annakkage, D. Muthumuni, and C. Karawita, "Parallel operation of grid-forming inverters with synchronous machines," in *Proc. CIGRE Canada Conf. Expo*, (Calgary, Canada), Oct. 2022.

6.3 Recommendations for Future work

This study has widened the horizon of interaction analysis in GFM inverter systems by including the dynamics of both the dc and ac sides of the GFM inverter and the full dynamics of the GFM controller. The following directions are suggested for future pursuit.

- The three commonly used current-limiting algorithms that were explicitly designed to handle balanced faults were incorporated into the study to analyze their effect on causing interactions. However, the most common types of faults in power system are unbalanced faults. Therefore, the development of linearized models of controllers that can handle unbalanced faults and analysis of their impact on critical interaction is an important research direction.

- The dc-side dynamics were considered through a generic representation. However, different dc-side configurations will provide case-specific information regarding the system stability. For example, widening the study for wind turbines with machine-side converters and rectifiers behind dc transmission lines in HVDC systems can provide more insight into the interactions in such GFM inverter systems.

- Modular multi-level converter (MMC) applications in the HVDC transmission are prominent. MMCs introduce converter dynamics due to sub-module capacitors and arm inductors. Therefore, extending the stability analysis with an MMC-based GFM inverter system would suitably extend the interaction analysis in GFM inverter systems.

- The realization of a synchronous machine by utilizing the electrostatic energy stored in the dc-link capacitor and other energy storage devices on dc-side is another GFM controller realization method that is becoming increasingly attractive. Therefore, interaction analysis with such a GFM controller can be a potential research direction.

Appendix A

An overview of the small-signal stability assessment is given in this section and a detailed description can be found in [19]. Small-signal stability is the power system's ability to maintain synchronism when subjected to small disturbances [19]. A disturbance is small enough when the equations describing the system's resulting response can be linearized for the analysis.

A.1 State-Space Representation

States are the minimum set of linearly independent system variables that along with the system inputs provide a complete description of the system [19]. The behavior of a dynamic system can be represented by a set of first order non-linear differential equations that explains the behavior of the states as shown in (A.1). Here $\mathbf{x}$ and $\mathbf{u}$ represent the matrices corresponding to states and inputs, respectively.

$$\dot{\mathbf{x}} = \mathbf{f}(\mathbf{x}, \mathbf{u}) \tag{A.1}$$

The output variables which can be observed in the system may be expressed in terms of states and input variables as shown in (A.2).

$$\mathbf{y} = \mathbf{g}(\mathbf{x}, \mathbf{u}) \tag{A.2}$$

A.2 System Stability

The stability of a non-linear system is governed by the type and magnitude of the input, and the initial state. The small-signal stability (i.e., the stability under small disturbances) of non-linear systems can be carried out by linearizing the non-linear equations around an equilibrium point.

A.2.1 Linearization

Equations (A.1)-(A.2) can be linearized around an equilibrium point by assuming perturbations are small enough so that second and higher order terms of $\mathbf{\Delta x}$ and $\mathbf{\Delta u}$ can be neglected in the Taylor series expansion. This assumption will result in (A.3)-(A.4).

$$\dot{\mathbf{\Delta x}} = \mathbf{A\Delta x} + \mathbf{B\Delta u} \tag{A.3}$$

$$\dot{\mathbf{\Delta y}} = \mathbf{C\Delta x} + \mathbf{D\Delta u} \tag{A.4}$$

The Laplace transformation of (A.3) results in (A.5).

$$\mathbf{\Delta x}(s) = \frac{\text{adj}(s\mathbf{I} - \mathbf{A})}{\det(\mathbf{I} - \mathbf{A})}(\mathbf{\Delta x}(0) + \mathbf{B\Delta u}(s)) \tag{A.5}$$

The poles of (A.5) are given by the roots of (A.6).

$$\det(s\text{I} - \text{A}) = 0 \tag{A.6}$$

s values which satisfy (A.6) are identified the eigenvalues of matrix $\mathbf{A}$.

A.2.2 Stability analysis

According to Lyapunov's first method, the small signal stability of a non-linear system is given by eigenvalues of $\mathbf{A}$ as follows:

- When the real part of the eigenvalues are negative, the original system is asymptotically stable.
- When at least one eigenvalue has a positive real part, the original system is unstable.
- When the eigenvalues have zero real parts, the first approximation is insufficient to comment about the stability.

A.3 Eigenvectors and Modal Matrices

A.3.1 Right eigenvector

For any n column vector $\boldsymbol{\phi}_i$ which satisfies (A.7), is called the right eigenvector of $\mathbf{A}$ associated with the eigenvalue λ_i. Here $i = 1, 2, ...,n$

$$\mathbf{A}\boldsymbol{\phi_i} = \lambda_i \boldsymbol{\phi_i} \tag{A.7}$$

A.3.2 Left eigenvector

For any n row vector $\boldsymbol{\Psi_i}$ which satisfies (A.8), is called the left eigenvector of $\mathbf{A}$ associated with the eigenvalue λ_i. Here $i = 1, 2, ...,n$

$$\boldsymbol{\Psi_i}\mathbf{A} = \lambda_i \boldsymbol{\Psi_i} \tag{A.8}$$

A.3.3 Modal matrices

To express eigenproperties of $\boldsymbol{A}$, it is convenient to define the following modal matrices.

$$\boldsymbol{\Phi} = [\boldsymbol{\phi_1}, \boldsymbol{\phi_2}, .., \boldsymbol{\phi_n}] \tag{A.9}$$

$$\boldsymbol{\Psi} = [\boldsymbol{\Psi_1}^{\boldsymbol{T}}, \boldsymbol{\Psi_2}^{\boldsymbol{T}}, .., \boldsymbol{\Psi_n}^{\boldsymbol{T}}]^T \tag{A.10}$$

$\mathbf{\Lambda}$ = diagonal matrix, with the eigenvakues $\lambda_1, \lambda_2, ..., \lambda_n$ as diagonal elements

(A.11)

A.4 Free Motion of a Dynamic System

The (A.3) can be represented as (A.12) for the free motion (i.e. with zero input) study.

$$\dot{\mathbf{\Delta x}} = \mathbf{A\Delta x} \tag{A.12}$$

As shown in (A.12), the rate of change of each state variable is a linear combination of all the state variables. This cross-coupling of state variables challenges the discovery of factors which significantly affect the oscillations. To eliminate this cross coupling the following transformation is introduced.

$$\mathbf{\Delta x} = \phi\mathbf{z} \tag{A.13}$$

By substituting (A.13) in (A.12), the following relationship can be obtained.

$$\dot{\mathbf{z}} = \mathbf{\Lambda z} \tag{A.14}$$

Equation (A.14) gives n decoupled first order differential equations as shown in (A.15). Here $i = 1, 2, ...,n$

$$\dot{z_i} = \lambda_i z_i \tag{A.15}$$

The time domain response of each mode is given by (A.16).

$$z_i(t) = z_i(0)e^{\lambda_i t} \tag{A.16}$$

Therefore, it can be concluded that the time dependent characteristics of a mode is dependent on an eigenvalue as follows:

- A real eigenvalue corresponds to a non-oscillatory mode.

- Complex eigenvalue (occurs in complex conjugate pairs) corresponds to an oscillatory mode.

For a complex conjugate pair of eigenvalues;

$$\lambda = \sigma \pm j\omega \tag{A.17}$$

Frequency of oscillation in Hz is given by;

$$f = \omega/2\pi \tag{A.18}$$

The damping ratio is given by;

$$\zeta = -\sigma/\sqrt{\sigma^2 + \omega^2} \tag{A.19}$$

A.5 Mode Shapes and Participation Factor

A.5.1 Mode shape

According to (A.13), the magnitude of the elements of ϕ_i gives the extent of the activities of the n state variables in the i^{th} mode. The angle of the elements of ϕ_i gives phase displacement of the state variables with regard to the mode. If the mode shape of any of the state variables are close by (i.e., around 0° phase displacement) these states are identified to be oscillating together when the i^{th} mode is excited. The states are identified to be oscillating against each other when the phase displacement is around 180°. Out of significantly participating state variables, the state variables that can lead to adverse interactions can be found out by the mode shape analysis.

A.5.2 Participation factor

The participation factor for the i^{th} state variable is calculated as follows;

$$\boldsymbol{P_i} = \begin{bmatrix} \phi_{1i}\Psi_{i1} & \phi_{2i}\Psi_{i2} & . & . & . & \phi_{ni}\Psi_{in} \end{bmatrix}^{\text{T}} \tag{A.20}$$

Here; $\phi_{ki} = k^{\text{th}}$ entry of the right eigenvector ϕ_i $\Psi_{ik} = k^{\text{th}}$ entry of the left eigenvector Ψ_i $p_{ki} = \phi_{ki}\Psi_{ik}$ is the relative participation of the k^{th} state variable in the i^{th} mode. Sum of participation factors associated with any mode ($\sum_{k=1}^{n} p_{ki} = 1$) or with any state ($\sum_{i=1}^{n} p_{ki} = 1$) is equal to 1. Therefore, in this study the participation factors of all the states in a particular mode are divided by the maximum participation factor of that mode to normalize the participation factors.

A.6 Controllability and Observability

Equations (A.3)-(A.4) can be represented using modes as shown in (A.21)-(A.22).

$$\dot{\mathbf{z}} = \boldsymbol{\Lambda}\mathbf{z} + \mathbf{B}^{'}\boldsymbol{\Delta}\mathbf{u} \tag{A.21}$$

$$\boldsymbol{\Delta}\mathbf{y} = \mathbf{C}^{'}\mathbf{z} + \mathbf{D}\boldsymbol{\Delta}\mathbf{u} \tag{A.22}$$

Here, $\mathbf{B}^{'} = \boldsymbol{\phi}^{-\mathbf{1}}\mathbf{B}$ and $\mathbf{C}^{'} = \mathbf{C}\boldsymbol{\phi}$. The i^{th} mode is uncontrollable if the i^{th} row of $\mathbf{B}^{'}$ is equal to zero. The i^{th} mode is unobservable if the i^{th} column of $\mathbf{C}^{'}$ is equal to zero.

Appendix B

Appendix A includes the expanded form of the matrices relevant to the small-signal representation of each sub-component of the GFM inverter.

B.1 Reference frame transformation

The expanded form of relevant matrices in section 2.2.1 is mentioned under this section.

$$A_\delta = 0 \qquad \boldsymbol{A_{\delta \mathbf{gfm_1}}} = \begin{bmatrix} -\omega_\mathrm{b} & \boldsymbol{0}_{1\times 16} \end{bmatrix} \qquad \boldsymbol{A_{\delta \mathbf{gfm_2}}} = \begin{bmatrix} \omega_\mathrm{b} & \boldsymbol{0}_{1\times 16} \end{bmatrix}$$

B.2 Power controller

The expanded form of relevant matrices in section 2.2.2 is mentioned under this section.

$$\boldsymbol{A_\mathbf{P}} = \begin{bmatrix} \frac{-1}{2HD_\mathrm{p}} & \frac{-1}{2H} & 0 & 0 & 0 \\ 0 & \frac{-1}{T_\mathrm{p}} & 0 & 0 & 0 \\ 0 & 0 & \frac{-1}{T_\mathrm{q}} & 0 & 0 \\ 0 & 0 & 0 & \frac{-1}{T_\mathrm{v}} & 0 \\ 0 & 0 & -D_\mathrm{q} & -1 & 0 \end{bmatrix}$$

$$\boldsymbol{A}_{\mathbf{PLCL}} = \begin{bmatrix} 0 & 0 & 0 & 0 & 0 & 0 & 0 & 0 \\ \frac{R_{\mathrm{f}} i_{\mathrm{td0}}}{T_{\mathrm{p}}} & \frac{R_{\mathrm{f}} i_{\mathrm{tq0}}}{T_{\mathrm{p}}} & \frac{i_{\mathrm{td0}}}{T_{\mathrm{p}}} & \frac{i_{\mathrm{tq0}}}{T_{\mathrm{p}}} & \frac{\mathrm{d}}{T_{\mathrm{p}}} & \frac{\mathrm{e}}{T_{\mathrm{p}}} & 0 & 0 \\ \frac{R_{\mathrm{f}} i_{\mathrm{tq0}}}{-T_{\mathrm{q}}} & \frac{-R_{\mathrm{f}} i_{\mathrm{td0}}}{-T_{\mathrm{q}}} & \frac{i_{\mathrm{tq0}}}{-T_{\mathrm{q}}} & \frac{-i_{\mathrm{td0}}}{-T_{\mathrm{q}}} & \frac{\mathrm{f}}{-T_{\mathrm{q}}} & \frac{\mathrm{g}}{-T_{\mathrm{q}}} & 0 & 0 \\ \frac{\mathrm{a} R_{\mathrm{f}}}{\mathrm{c}} & \frac{\mathrm{b} R_{\mathrm{f}}}{\mathrm{c}} & \frac{\mathrm{a}}{\mathrm{c}} & \frac{\mathrm{b}}{\mathrm{c}} & \frac{-\mathrm{a} R_{\mathrm{f}}}{\mathrm{c}} & \frac{-\mathrm{b} R_{\mathrm{f}}}{\mathrm{c}} & 0 & 0 \\ 0 & 0 & 0 & 0 & 0 & 0 & 0 & 0 \end{bmatrix}$$

Here;

$$\mathrm{a} = v_{\mathrm{fd0}} + (i_{\mathrm{cvd0}} - i_{\mathrm{td0}}) R_{\mathrm{f}}, \quad \mathrm{b} = v_{\mathrm{fq0}} + (i_{\mathrm{cvq0}} - i_{\mathrm{tq0}}) R_{\mathrm{f}}, \mathrm{c} = T_{\mathrm{v}} \sqrt{\mathrm{a}^2 + \mathrm{b}^2}$$

$$\mathrm{d} = v_{\mathrm{fd0}} + R_{\mathrm{f}} i_{\mathrm{cvd0}} - 2 R_{\mathrm{f}} i_{\mathrm{td0}}, \quad \mathrm{e} = v_{\mathrm{fq0}} + R_{\mathrm{f}} i_{\mathrm{cvq0}} - 2 R_{\mathrm{f}} i_{\mathrm{tq0}}, \mathrm{f} = -(v_{\mathrm{fq0}} + R_{\mathrm{f}} i_{\mathrm{cvq0}}), \quad \mathrm{g} = v_{\mathrm{fd0}} + R_{\mathrm{f}} i_{\mathrm{cvd0}}$$

$$\boldsymbol{A}_{\mathbf{PN}} = \boldsymbol{A}_{\mathbf{PL}} = \boldsymbol{0}_{5 \times 4}$$

$$\boldsymbol{B}_{\mathbf{P}} = \begin{bmatrix} \frac{1}{2 H D_{\mathrm{p}}} & \frac{1}{2H} & 0 & 0 \\ 0 & 0 & 0 & 0 \\ 0 & 0 & 0 & 0 \\ 0 & 0 & 0 & 0 \\ 0 & 0 & D_{\mathrm{q}} & 1 \end{bmatrix}$$

$$\boldsymbol{C}_{\mathbf{E}} = \begin{bmatrix} 0 & 0 & K_{\mathrm{p}} D_{\mathrm{q}} & K_{\mathrm{p}} & -\frac{1}{T_{\mathrm{i}}} \end{bmatrix} \qquad \boldsymbol{D}_{\mathbf{E}} = \begin{bmatrix} 0 & 0 & -K_{\mathrm{p}} D_{\mathrm{q}} & -K_{\mathrm{p}} \end{bmatrix}$$

B.3 LC filter and transformer

The expanded form of relevant matrices in section 2.2.3 are mentioned under this section.

$$\boldsymbol{A_{\mathbf{LCLd}}} = \omega_{\mathrm{b}} \begin{bmatrix} \frac{-R_{\mathrm{f}}}{L_{\mathrm{f}}} & \omega_{\mathrm{gfm0}} & \frac{-1}{L_{\mathrm{f}}} & 0 & \frac{R_{\mathrm{f}}}{L_{\mathrm{f}}} & 0 & 0 & 0 \\ -\omega_{\mathrm{gfm0}} & \frac{-R_{\mathrm{f}}}{L_{\mathrm{f}}} & 0 & \frac{-1}{L_{\mathrm{f}}} & 0 & \frac{R_{\mathrm{f}}}{L_{\mathrm{f}}} & 0 & 0 \\ \frac{1}{C_{\mathrm{f}}} & 0 & 0 & \omega_{\mathrm{gfm0}} & \frac{-1}{C_{\mathrm{f}}} & 0 & 0 & 0 \\ 0 & \frac{1}{C_{\mathrm{f}}} & -\omega_{\mathrm{gfm0}} & 0 & 0 & \frac{-1}{C_{\mathrm{f}}} & 0 & 0 \\ \frac{R_{\mathrm{f}}}{L_{\mathrm{t}}} & 0 & \frac{1}{L_{\mathrm{t}}} & 0 & \frac{-(\mathrm{R_f+R_t})}{L_{\mathrm{t}}} & \omega_{\mathrm{gfm0}} & 0 & 0 \\ 0 & \frac{R_{\mathrm{f}}}{L_{\mathrm{t}}} & 0 & \frac{1}{L_{\mathrm{t}}} & -\omega_{\mathrm{gfm0}} & \frac{-(\mathrm{R_f+R_t})}{L_{\mathrm{t}}} & 0 & 0 \\ \frac{-R_{\mathrm{f}}}{L_{\mathrm{f}}} & \omega_{\mathrm{gfm0}} & \frac{-1}{L_{\mathrm{f}}} & 0 & \frac{R_{\mathrm{f}}}{L_{\mathrm{f}}} & 0 & \frac{-1}{T_{\mathrm{hp}}\omega_{\mathrm{b}}} & 0 \\ -\omega_{\mathrm{gfm0}} & \frac{-R_{\mathrm{f}}}{L_{\mathrm{f}}} & 0 & \frac{-1}{L_{\mathrm{f}}} & 0 & \frac{R_{\mathrm{f}}}{L_{\mathrm{f}}} & 0 & \frac{-1}{T_{\mathrm{hp}}\omega_{\mathrm{b}}} \end{bmatrix}$$

$$\boldsymbol{B_{\mathbf{LCLd1}}} = \omega_{\mathrm{b}} \begin{bmatrix} i_{\mathrm{cvq0}} & -i_{\mathrm{cvd0}} & v_{\mathrm{fq0}} & -v_{\mathrm{fd0}} & i_{\mathrm{tq0}} & -i_{\mathrm{td0}} & i_{\mathrm{cvq0}} & -i_{\mathrm{cvd0}} \end{bmatrix}^{\mathrm{T}}$$

$$\boldsymbol{B_{\mathbf{LCLd2}}} = \omega_{\mathrm{b}} \begin{bmatrix} \frac{1}{L_{\mathrm{f}}} & 0 & 0 & 0 & 0 & 0 & \frac{1}{L_{\mathrm{f}}} & 0 \\ 0 & \frac{1}{L_{\mathrm{f}}} & 0 & 0 & 0 & 0 & 0 & \frac{1}{L_{\mathrm{f}}} \end{bmatrix}^{\mathrm{T}}$$

$$\boldsymbol{B_{\mathbf{LCLd3}}} = \omega_{\mathrm{b}} \begin{bmatrix} 0 & 0 & 0 & 0 & \frac{-1}{L_{\mathrm{t}}} & 0 & 0 & 0 \\ 0 & 0 & 0 & 0 & 0 & \frac{-1}{L_{\mathrm{t}}} & 0 & 0 \end{bmatrix}^{\mathrm{T}}$$

$$\boldsymbol{A_{\mathbf{vcdqP}}} = \begin{bmatrix} \sin(-30^{^\circ}) \\ \cos(-30^{^\circ}) \end{bmatrix} \boldsymbol{C_{\mathbf{E}}} + L_{\mathrm{vi0}} \begin{bmatrix} i_{\mathrm{cvqhp0}} \\ -i_{\mathrm{cvdhp0}} \end{bmatrix} \begin{bmatrix} 1 & 0 & 0 & 0 & 0 \end{bmatrix}$$

$$\boldsymbol{A_{\mathbf{vcdqLCL}}} = \begin{bmatrix} 0 & 0 & 0 & 0 & 0 & 0 & -R_{\mathrm{vi0}} & \omega_{\mathrm{gfm0}} L_{\mathrm{vi0}} \\ 0 & 0 & 0 & 0 & 0 & 0 & -\omega_{\mathrm{gfm0}} L_{\mathrm{vi0}} & -R_{\mathrm{vi0}} \end{bmatrix}$$

$$\boldsymbol{B_{\mathbf{vcdq}}} = \begin{bmatrix} \sin(-30^{^\circ}) \\ \cos(-30^{^\circ}) \end{bmatrix} \boldsymbol{D_{\mathbf{E}}}$$

$$\boldsymbol{A_{\mathbf{LCLP}}} = \boldsymbol{B_{\mathbf{LCLd1}}} \begin{bmatrix} 1 & 0 & 0 & 0 & 0 \end{bmatrix} + \boldsymbol{B_{\mathbf{LCLd2}}} \boldsymbol{A_{\mathbf{vcdqP}}}$$

$$\boldsymbol{A_{\mathbf{LCL}}} = \boldsymbol{A_{\mathbf{LCLd}}} + \boldsymbol{B_{\mathbf{LCLd2}}} \boldsymbol{A_{\mathbf{vcdqLCL}}} \qquad \boldsymbol{A_{\mathbf{LCLN}}} = \boldsymbol{B_{\mathbf{LCLd3}}} \begin{bmatrix} 1 & 0 & 0 & 0 \\ 0 & 1 & 0 & 0 \end{bmatrix}$$

$$\boldsymbol{A_{\mathbf{LCLL}}} = \boldsymbol{0}_{8\times 4} \qquad \boldsymbol{B_{\mathbf{LCL}}} = \boldsymbol{B_{\mathbf{LCLd2}}} \boldsymbol{B_{\mathbf{vcdq}}}$$

B.4 Network

The expanded form of relevant matrices in section 2.2.4 is shown in this section.

$$\boldsymbol{A_{\mathbf{Nd}}} = \omega_{\mathrm{b}} \begin{bmatrix} 0 & \omega_{\mathrm{gfm0}} & \frac{-1}{C_{\mathrm{pi}}} & 0 \\ -\omega_{\mathrm{gfm0}} & 0 & 0 & \frac{-1}{C_{\mathrm{pi}}} \\ \frac{1}{L_{\mathrm{tx}}} & 0 & \frac{-R_{\mathrm{tx}}}{L_{\mathrm{tx}}} & \omega_{\mathrm{gfm0}} \\ 0 & \frac{1}{L_{\mathrm{tx}}} & -\omega_{\mathrm{gfm0}} & \frac{-R_{\mathrm{tx}}}{L_{\mathrm{tx}}} \end{bmatrix} \quad \boldsymbol{B_{\mathbf{Nd1}}} = \omega_{\mathrm{b}} \begin{bmatrix} v_{\mathrm{piq0}} & -v_{\mathrm{pid0}} & i_{\mathrm{txq0}} & -i_{\mathrm{txd0}} \end{bmatrix}^{\mathrm{T}}$$

$$\boldsymbol{B_{\mathbf{Nd2}}} = \omega_{\mathrm{b}} \begin{bmatrix} \frac{1}{C_{\mathrm{pi}}} & 0 & 0 & 0 \\ 0 & \frac{1}{C_{\mathrm{pi}}} & 0 & 0 \end{bmatrix}^{\mathrm{T}} \qquad \boldsymbol{B_{\mathbf{Nd3}}} = \omega_{\mathrm{b}} \begin{bmatrix} 0 & 0 & \frac{-1}{L_{\mathrm{tx}}} & 0 \\ 0 & 0 & 0 & \frac{-1}{L_{\mathrm{tx}}} \end{bmatrix}^{\mathrm{T}}$$

$$\boldsymbol{B_{\mathbf{Nd4}}} = \begin{bmatrix} -\sin(\delta_0) & \cos(\delta_0) \\ -\cos(\delta_0) & -\sin(\delta_0) \end{bmatrix} \begin{bmatrix} v_{\mathrm{Ld0}} \\ v_{\mathrm{Lq0}} \end{bmatrix} \qquad \boldsymbol{B_{\mathbf{Nd5}}} = \begin{bmatrix} \cos(\delta_0) & \sin(\delta_0) \\ -\sin(\delta_0) & \cos(\delta_0) \end{bmatrix}$$

$$\boldsymbol{A_{\mathbf{N\delta}}} = \boldsymbol{B_{\mathbf{Nd3}}} \boldsymbol{B_{\mathbf{Nd4}}} \qquad \boldsymbol{A_{\mathbf{NP}}} = \boldsymbol{B_{\mathbf{Nd1}}} \begin{bmatrix} 1 & 0 & 0 & 0 & 0 \end{bmatrix}$$

$$\boldsymbol{A_{\mathbf{NLCL}}} = \boldsymbol{B_{\mathbf{Nd2}}} \begin{bmatrix} 0 & 0 & 0 & 0 & 1 & 0 & 0 & 0 \\ 0 & 0 & 0 & 0 & 0 & 1 & 0 & 0 \end{bmatrix} \qquad \boldsymbol{A_{\mathbf{N}}} = \boldsymbol{A_{\mathbf{Nd}}}$$

$$\boldsymbol{A_{\mathbf{NL}}} = \boldsymbol{B_{\mathbf{Nd3}}} \boldsymbol{B_{\mathbf{Nd5}}} \begin{bmatrix} 1 & 0 & 0 & 0 \\ 0 & 1 & 0 & 0 \end{bmatrix} \qquad \boldsymbol{B_{\mathbf{N}}} = \boldsymbol{0}_{4\times 4}$$

B.5 Load

The expanded form of matrices in (2.39) are given below.

$$\boldsymbol{A_{Ld}} = \omega_{\mathrm{b}} \begin{bmatrix} \frac{-1}{C_{\mathrm{L}} R_{\mathrm{L0}}} & \omega_{\mathrm{gfm10}} & \frac{-1}{C_{\mathrm{L}}} & 0 \\ -\omega_{\mathrm{gfm10}} & \frac{-1}{C_{\mathrm{L}} R_{\mathrm{L0}}} & 0 & \frac{-1}{C_{\mathrm{L}}} \\ \frac{1}{L_{\mathrm{L}}} & 0 & 0 & \omega_{\mathrm{gfm10}} \\ 0 & \frac{1}{L_{\mathrm{L}}} & -\omega_{\mathrm{gfm10}} & 0 \end{bmatrix} \qquad \boldsymbol{B_{Ld1}} = \omega_{\mathrm{b}} \begin{bmatrix} v_{\mathrm{Lq0}} & -v_{\mathrm{Ld0}} & i_{\mathrm{Lq0}} & -i_{\mathrm{Ld0}} \end{bmatrix}^{\mathrm{T}}$$

$$\boldsymbol{B_{Ld2}} = \omega_{\mathrm{b}} \begin{bmatrix} \frac{v_{\mathrm{Ld0}}}{C_{\mathrm{L}} R_{\mathrm{L0}}^2} & \frac{v_{\mathrm{Lq0}}}{C_{\mathrm{L}} R_{\mathrm{L0}}^2} & 0 & 0 \end{bmatrix}^{\mathrm{T}} \qquad \boldsymbol{B_{Ld3}} = \omega_{\mathrm{b}} \begin{bmatrix} \frac{1}{C_{\mathrm{L}}} & 0 & 0 & 0 \\ 0 & \frac{1}{C_{\mathrm{L}}} & 0 & 0 \end{bmatrix}^{\mathrm{T}}$$

$$\boldsymbol{B_{Ld4_2}} = \begin{bmatrix} -\sin(\delta_0) & -\cos(\delta_0) \\ \cos(\delta_0) & -\sin(\delta_0) \end{bmatrix} \begin{bmatrix} i_{\mathrm{txd0}} \\ i_{\mathrm{txq0}} \end{bmatrix} \qquad \boldsymbol{B_{Ld5_2}} = \begin{bmatrix} \cos(\delta_0) & -\sin(\delta_0) \\ \sin(\delta_0) & \cos(\delta_0) \end{bmatrix}$$

The expanded form of matrices in (2.40) are given below.

$$\boldsymbol{A_{Load\delta}} = \boldsymbol{B_{Ld3}} \boldsymbol{B_{Ld4_2}}$$

$$\boldsymbol{A_{Loadgfm_1}} = \begin{bmatrix} \boldsymbol{B_{Ld1}} \begin{bmatrix} 1 & 0 & 0 & 0 & 0 \end{bmatrix} & \boldsymbol{0}_{4\times 8} & \boldsymbol{B_{Ld3}} \boldsymbol{B_{Ld5_1}} \begin{bmatrix} 0 & 0 & 1 & 0 \\ 0 & 0 & 0 & 1 \end{bmatrix} \end{bmatrix}$$

$$\boldsymbol{A_{Loadgfm_2}} = \begin{bmatrix} \boldsymbol{0}_{4\times 5} & \boldsymbol{0}_{4\times 8} & \boldsymbol{B_{Ld3}} \boldsymbol{B_{Ld5_2}} \begin{bmatrix} 0 & 0 & 1 & 0 \\ 0 & 0 & 0 & 1 \end{bmatrix} \end{bmatrix}$$

$$\boldsymbol{A_{Load}} = \boldsymbol{A_{Ld}} \qquad \boldsymbol{B_{Load}} = \boldsymbol{B_{Ld2}} \qquad \boldsymbol{\Delta U_{L}} = \Delta R_{\mathrm{L}}$$

Appendix C

The set of differential equations from [19] are used to model the dynamics of the synchronous machine.

$$\mathrm{d}\omega_{\mathrm{sm}}/\mathrm{d}t = (1/2H)(T_{\mathrm{m}} - (\psi_{\mathrm{d}} i_{\mathrm{q}} - \psi_{\mathrm{q}} i_{\mathrm{d}}) - K_{\mathrm{D}}\omega_{\mathrm{sm}}) \tag{C.1}$$

$$\mathrm{d}\psi_{\mathrm{d}}/\mathrm{d}t = \omega_{\mathrm{b}}(e_{\mathrm{d}} + \omega_{\mathrm{sm}}\psi_{\mathrm{q}} + R_{\mathrm{a}} i_{\mathrm{d}}) \tag{C.2}$$

$$\mathrm{d}\psi_{\mathrm{fd}}/\mathrm{d}t = \omega_{\mathrm{b}}(e_{\mathrm{fd}} - R_{\mathrm{fd}} i_{\mathrm{fd}}) \tag{C.3}$$

$$\mathrm{d}\psi_{1\mathrm{d}}/\mathrm{d}t = \omega_{\mathrm{b}}(-R_{1\mathrm{d}} i_{1\mathrm{d}}) \tag{C.4}$$

$$\mathrm{d}\psi_{\mathrm{q}}/\mathrm{d}t = \omega_{\mathrm{b}}(e_{\mathrm{q}} - \omega_{\mathrm{sm}}\psi_{\mathrm{d}} + R_{\mathrm{a}} i_{\mathrm{q}}) \tag{C.5}$$

$$\mathrm{d}\psi_{1\mathrm{q}}/\mathrm{d}t = \omega_{\mathrm{b}}(-R_{1\mathrm{q}} i_{1\mathrm{q}}) \tag{C.6}$$

$$\mathrm{d}\psi_{2\mathrm{q}}/\mathrm{d}t = \omega_{\mathrm{b}}(-R_{2\mathrm{q}} i_{2\mathrm{q}}) \tag{C.7}$$

The first step to modify the above mentioned differential equations is to replace the rotor current components using the rotor's flux components and stator current's dq components.

C.1 Representation of rotor current components

The equivalent circuits for the d and q axis of the synchronous machine which show flux linkage and current relationship of each path are given in Figure C.1.

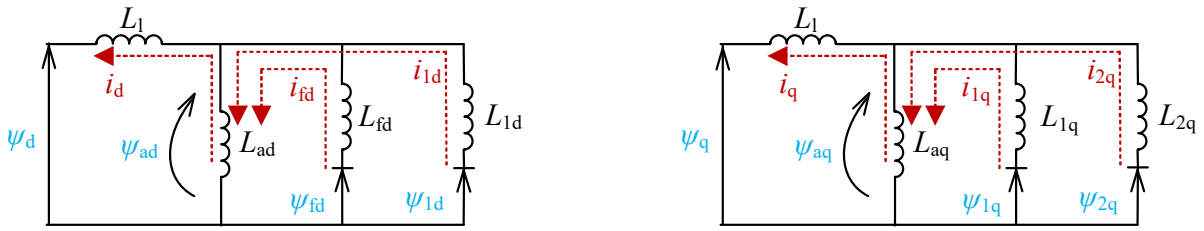

(a) (b)

Fig. C.1: Synchronous machine's equivalent circuit for (a) d-axis and (b) q-axis

From the d-axis equivalent circuit:

$$\psi_{ad} = L_{ad}(-i_d + i_{fd} + i_{1d}) \tag{C.8}$$

$$i_{fd} = (\psi_{fd} - \psi_{ad})/L_{fd} \tag{C.9}$$

$$i_{1d} = (\psi_{1d} - \psi_{ad})/L_{1d} \tag{C.10}$$

By substituting (C.9) and (C.10) in (C.8), .

$$\psi_{ad} = L''_{ad}(-i_d + \psi_{fd}/L_{fd} + \psi_{1d}/L_{1d}) \tag{C.11}$$

Here

$$L''_{ad} = \frac{1}{\frac{1}{L_{ad}} + \frac{1}{L_{fd}} + \frac{1}{L_{1d}}}$$

Similarly for the q-axis

$$i_{1q} = (\psi_{1q} - \psi_{aq})/L_{1q} \tag{C.12}$$

$$i_{2q} = (\psi_{2q} - \psi_{aq})/L_{2q} \tag{C.13}$$

$$\psi_{aq} = L''_{aq}(-i_q + \psi_{1q}/L_{1q} + \psi_{2q}/L_{2q}) \tag{C.14}$$

Here

$$L''_{aq} = \frac{1}{\frac{1}{L_{aq}} + \frac{1}{L_{1q}} + \frac{1}{L_{2q}}}$$

Therefore rotor current components can be represented using rotor flux components and stator current's dq components.

$$i_{\mathrm{fd}} = \psi_{\mathrm{fd}}/L_{\mathrm{fd}} - (L''_{\mathrm{ad}}/L_{\mathrm{fd}})(-i_{\mathrm{d}} + \psi_{\mathrm{fd}}/L_{\mathrm{fd}} + \psi_{1\mathrm{d}}/L_{1\mathrm{d}}) \tag{C.15}$$

$$i_{1\mathrm{d}} = \psi_{1\mathrm{d}}/L_{1\mathrm{d}} - (L''_{\mathrm{ad}}/L_{1\mathrm{d}})(-i_{\mathrm{d}} + \psi_{\mathrm{fd}}/L_{\mathrm{fd}} + \psi_{1\mathrm{d}}/L_{1\mathrm{d}}) \tag{C.16}$$

$$i_{1\mathrm{q}} = \psi_{1\mathrm{q}}/L_{1\mathrm{q}} - (L''_{\mathrm{aq}}/L_{1\mathrm{q}})(-i_{\mathrm{q}} + \psi_{1\mathrm{q}}/L_{1\mathrm{q}} + \psi_{2\mathrm{q}}/L_{2\mathrm{q}}) \tag{C.17}$$

$$i_{2\mathrm{q}} = \psi_{2\mathrm{q}}/L_{2\mathrm{q}} - (L''_{\mathrm{aq}}/L_{2\mathrm{q}})(-i_{\mathrm{q}} + \psi_{1\mathrm{q}}/L_{1\mathrm{q}} + \psi_{2\mathrm{q}}/L_{2\mathrm{q}}) \tag{C.18}$$

According to [19],

$$e_{\mathrm{fd}} = (R_{\mathrm{fd}}/L_{\mathrm{ad}})E_{\mathrm{fd}} \tag{C.19}$$

By substituting (C.15)-(C.19) in (C.3)-(C.7), the following equation set can be obtained to model the dynamics of the rotor flux linkages.

$$\mathrm{d}\psi_{\mathrm{fd}}/\mathrm{d}t = k_1\psi_{\mathrm{fd}} + k_2\psi_{1\mathrm{d}} + k_3 i_{\mathrm{d}} + k_4 E_{\mathrm{fd}} \tag{C.20}$$

$$\mathrm{d}\psi_{1\mathrm{d}}/\mathrm{d}t = k_5\psi_{\mathrm{fd}} + k_6\psi_{1\mathrm{d}} + k_7 i_{\mathrm{d}} \tag{C.21}$$

$$\mathrm{d}\psi_{1\mathrm{q}}/\mathrm{d}t = k_8\psi_{1\mathrm{q}} + k_9\psi_{2\mathrm{q}} + k_{10} i_{\mathrm{q}} \tag{C.22}$$

$$\mathrm{d}\psi_{2\mathrm{q}}/\mathrm{d}t = k_{11}\psi_{1\mathrm{q}} + k_{12}\psi_{2\mathrm{q}} + k_{13} i_{\mathrm{q}} \tag{C.23}$$

Here,

$$k_1 = \frac{\omega_b R_{fd}}{L_{fd}}\left(-1 + \frac{L''_{ad}}{L_{fd}}\right) \qquad k_2 = \frac{\omega_b R_{fd} L''_{ad}}{L_{fd} L_{1d}} \qquad k_3 = \frac{-\omega_b R_{fd} L''_{ad}}{L_{fd}}$$

$$k_4 = \frac{\omega_b R_{fd}}{L_{ad}} \qquad k_5 = \frac{\omega_b R_{1d} L''_{ad}}{L_{fd} L_{1d}} \qquad k_6 = \frac{\omega_b R_{1d}}{L_{1d}}\left(-1 + \frac{L''_{ad}}{L_{1d}}\right)$$

$$k_7 = \frac{-\omega_b R_{1d} L''_{ad}}{L_{1d}} \qquad k_8 = \frac{\omega_b R_{1q}}{L_{1q}}\left(-1 + \frac{L''_{aq}}{L_{1q}}\right) \qquad k_9 = \frac{\omega_b R_{1q} L''_{aq}}{L_{1q} L_{2q}}$$

$$k_{10} = \frac{-\omega_b R_{1q} L''_{aq}}{L_{1q}} \qquad k_{11} = \frac{\omega_b R_{2q} L''_{aq}}{L_{1q} L_{2q}} \qquad k_{12} = \frac{\omega_b R_{2q}}{L_{2q}}\left(-1 + \frac{L''_{aq}}{L_{2q}}\right)$$

$$k_{13} = \frac{-\omega_b R_{2q} L''_{aq}}{L_{2q}}$$

C.2 Representation of stator flux components

This section shows the steps for replacing the dq components of the stator flux linkage with the dq components of the stator current and the rotor flux linkages. From Fig.C.1a:

$$i_d = (\psi_{ad} - \psi_d)/L_l \tag{C.24}$$

$$i_q = (\psi_{aq} - \psi_q)/L_l \tag{C.25}$$

By substituting (C.24) in (C.11), (C.26) can be obtained.

$$\psi_{ad} = L_{ppd}(\psi_d/L_l + \psi_{fd}/L_{fd} + \psi_{1d}/L_{1d}) \tag{C.26}$$

Here

$$L_{ppd} = \frac{1}{\frac{1}{L_l} + \frac{1}{L_{ad}} + \frac{1}{L_{fd}} + \frac{1}{L_{1d}}}$$

Similarly, by substituting (C.25) in (C.14), (C.27) can be obatained.

$$\psi_{aq} = L_{ppq}(\psi_q/L_l + \psi_{1q}/L_{1q} + \psi_{2q}/L_{2q}) \tag{C.27}$$

Here

$$L_{\mathrm{ppq}} = \frac{1}{\frac{1}{L_{\mathrm{l}}} + \frac{1}{L_{\mathrm{aq}}} + \frac{1}{L_{1\mathrm{q}}} + \frac{1}{L_{2\mathrm{q}}}}$$

By substituting (C.26) in (C.24), (C.28) can be obtained.

$$i_{\mathrm{d}} = m_1\psi_{\mathrm{d}} + m_2\psi_{\mathrm{fd}} + m_3\psi_{1\mathrm{d}} \tag{C.28}$$

Here

$$m_1 = -L_{\mathrm{ppd}}/L_{\mathrm{l}}L''_{\mathrm{ad}} \qquad m_2 = L_{\mathrm{ppd}}/L_{\mathrm{l}}L_{\mathrm{fd}} \qquad m_3 = L_{\mathrm{ppd}}/L_{\mathrm{l}}L_{1\mathrm{d}}$$

Similarly, by substituting (C.27) in (C.25), (C.29) can be obtained.

$$i_{\mathrm{q}} = m_4\psi_{\mathrm{q}} + m_5\psi_{1\mathrm{q}} + m_6\psi_{2\mathrm{q}} \tag{C.29}$$

Here

$$m_4 = -L_{\mathrm{ppq}}/L_{\mathrm{l}}L''_{\mathrm{aq}} \qquad m_5 = L_{\mathrm{ppq}}/L_{\mathrm{l}}L_{1\mathrm{q}} \qquad m_6 = L_{\mathrm{ppq}}/L_{\mathrm{l}}L_{2\mathrm{q}}$$

By re-arranging (C.28) and (C.29), (C.30) and (C.31) can be obtained, respectively.

$$\mathrm{d}\psi_{\mathrm{d}}/\mathrm{d}t = (1/m_1)(\mathrm{d}i_{\mathrm{d}}/\mathrm{d}t) + (-m_2/m_1)(\mathrm{d}\psi_{\mathrm{fd}}/\mathrm{d}t) + (-m_3/m_1)(\mathrm{d}\psi_{1\mathrm{d}}/\mathrm{d}t) \tag{C.30}$$

$$\mathrm{d}\psi_{\mathrm{q}}/\mathrm{d}t = (1/m_4)(\mathrm{d}i_{\mathrm{q}}/\mathrm{d}t) + (-m_5/m_4)(\mathrm{d}\psi_{1\mathrm{q}}/\mathrm{d}t) + (-m_6/m_4)(\mathrm{d}\psi_{2\mathrm{q}}/\mathrm{d}t) \tag{C.31}$$

By equating (C.30) and (C.2), (C.32) can be obtained.

$$\mathrm{d}i_\mathrm{d}/\mathrm{d}t = (m_2k_3 + m_3k_7 + m_1\omega_\mathrm{b}R_\mathrm{a})i_\mathrm{d} + (m_2k_1 + m_3k_5)\psi_\mathrm{fd} + (m_2k_2 + m_3k_6)\psi_\mathrm{1d} + ((m_1\omega_\mathrm{b}\omega_\mathrm{sm})/m_4)i_\mathrm{q} + ((-m_1m_5\omega_\mathrm{b}\omega_\mathrm{sm})/m_4)\psi_\mathrm{1q} + ((-m_1m_6\omega_\mathrm{b}\omega_\mathrm{sm})/m_4)\psi_\mathrm{2q} + (m_1\omega_\mathrm{b})e_\mathrm{d} + (m_2k_4)E_\mathrm{fd} \quad \text{(C.32)}$$

Similarly by equating (C.31) and (C.5), (C.33) can be obtained.

$$\mathrm{d}i_\mathrm{q}/\mathrm{d}t = ((-m_4\omega_\mathrm{b}\omega_\mathrm{sm})/m_1)i_\mathrm{d} + ((m_4m_2\omega_\mathrm{b}\omega_\mathrm{sm})/m_1)\psi_\mathrm{fd} + ((m_4m_3\omega_\mathrm{b}\omega_\mathrm{sm})/m_1)\psi_\mathrm{1d} + (m_4\omega_\mathrm{b})e_\mathrm{q} (m_5k_{10} + m_6k_{13} + m_4\omega_\mathrm{b}R_\mathrm{a})i_\mathrm{q} + (m_5k_8 + m_6k_{11})\psi_\mathrm{1q} + (m_5k_9 + m_6k_{12})\psi_\mathrm{2q} \quad \text{(C.33)}$$

e_d and e_q in (C.32) and (C.33), respectively, have to be replaced with the other state variables. For this, the connecting transformer impedance is assumed in series with the stator winding and the detailed derivation is discussed in section C.3.

C.3 Representation of stator terminal voltage components

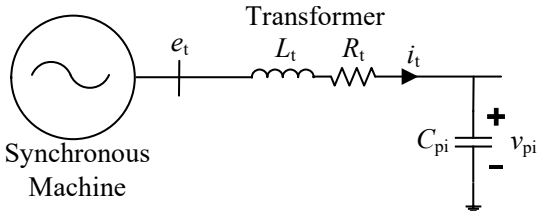

Fig. C.2: Synchronous machine and step-up transformer configuration in the test system

Figure C.2 focuses on the network configuration of the synchronous machine and the step-up transformer in the test system. The dynamic equation which governs the dynamics

of the transformer inductor current is given in (C.34).

$$\mathrm{d}i_\mathrm{t}/\mathrm{d}t = (-R_\mathrm{t}/L_\mathrm{t})i_\mathrm{t} + (-1/L_\mathrm{t})v_\mathrm{pi} + (1/L_\mathrm{t})e_\mathrm{t} \tag{C.34}$$

From (C.34), the dq components of the stator current can be obtained as shown in (C.35)-(C.36).

$$\mathrm{d}i_\mathrm{td}/\mathrm{d}t = (\omega_\mathrm{b}/L_\mathrm{t})(-R_\mathrm{t}i_\mathrm{td} - v_\mathrm{pid} + e_\mathrm{d} + L_\mathrm{t}\omega_\mathrm{sm}i_\mathrm{tq}) \tag{C.35}$$

$$\mathrm{d}i_\mathrm{tq}/\mathrm{d}t = (\omega_\mathrm{b}/L_\mathrm{t})(-R_\mathrm{t}i_\mathrm{tq} - v_\mathrm{piq} + e_\mathrm{q} - L_\mathrm{t}\omega_\mathrm{sm}i_\mathrm{td}) \tag{C.36}$$

By equating (C.32) and (C.35), (C.37) can be obtained.

$$e_\mathrm{d} = b_\mathrm{ed1}i_\mathrm{d} + b_\mathrm{ed2}\psi_\mathrm{fd} + b_\mathrm{ed3}\psi_\mathrm{1d} + b_\mathrm{ed4}i_\mathrm{q} + b_\mathrm{ed5}\psi_\mathrm{1q} + b_\mathrm{ed6}\psi_\mathrm{2q} + +b_\mathrm{ed7}v_\mathrm{pid} + b_\mathrm{ed8}E_\mathrm{fd} \tag{C.37}$$

Here,

$$b_\mathrm{ed1} = \frac{m_2k_3 + m_3k_7 + m_1\omega_\mathrm{b}R_\mathrm{a} + R_\mathrm{t}\omega_\mathrm{b}/L_\mathrm{t}}{\omega_\mathrm{b}(1/L_\mathrm{t} - m_1)} \qquad b_\mathrm{ed2} = \frac{m_2k_1 + m_3k_5}{\omega_\mathrm{b}(1/L_\mathrm{t} - m_1)}$$

$$b_\mathrm{ed3} = \frac{m_2k_2 + m_3k_6}{\omega_\mathrm{b}(1/L_\mathrm{t} - m_1)} \qquad b_\mathrm{ed4} = \frac{\omega_\mathrm{b}\omega_\mathrm{sm}(m_1/m_4 - 1)}{\omega_\mathrm{b}(1/L_\mathrm{t} - m_1)}$$

$$b_\mathrm{ed5} = \frac{\omega_\mathrm{b}\omega_\mathrm{sm}(-m_1m_5/m_4)}{\omega_\mathrm{b}(1/L_\mathrm{t} - m_1)} \qquad b_\mathrm{ed6} = \frac{\omega_\mathrm{b}\omega_\mathrm{sm}(-m_1m_6/m_4)}{\omega_\mathrm{b}(1/L_\mathrm{t} - m_1)}$$

$$b_\mathrm{ed7} = \frac{\omega_\mathrm{b}/L_\mathrm{t}}{\omega_\mathrm{b}(1/L_\mathrm{t} - m_1)} \qquad b_\mathrm{ed8} = \frac{m_2k_4}{\omega_\mathrm{b}(1/L_\mathrm{t} - m_1)}$$

Similarly, by equating (C.33) and (C.36), (C.38) can be obtained.

$$e_\mathrm{q} = b_\mathrm{eq1}i_\mathrm{d} + b_\mathrm{eq2}\psi_\mathrm{fd} + b_\mathrm{eq3}\psi_\mathrm{1d} + b_\mathrm{eq4}i_\mathrm{q} + b_\mathrm{eq5}\psi_\mathrm{1q} + b_\mathrm{eq6}\psi_\mathrm{2q} + +b_\mathrm{eq7}v_\mathrm{pid} + b_\mathrm{eq8}E_\mathrm{fd} \tag{C.38}$$

Here,

$$b_{\text{eq1}} = \frac{\omega_{\text{b}}\omega_{\text{sm}}(1 - m_4/m_1)}{\omega_{\text{b}}(1/L_{\text{t}} - m_4)} \qquad b_{\text{eq2}} = \frac{\omega_{\text{b}}\omega_{\text{sm}}(m_2 m_4/m_1)}{\omega_{\text{b}}(1/L_{\text{t}} - m_4)}$$

$$b_{\text{eq3}} = \frac{\omega_{\text{b}}\omega_{\text{sm}}(m_3 m_4/m_1)}{\omega_{\text{b}}(1/L_{\text{t}} - m_4)} \qquad b_{\text{eq4}} = \frac{m_5 k_{10} + m_6 k_{13} + m_4\omega_{\text{b}} R_{\text{a}} + R_{\text{t}}\omega_{\text{b}}/L_{\text{t}}}{\omega_{\text{b}}(1/L_{\text{t}} - m_4)}$$

$$b_{\text{eq5}} = \frac{m_5 k_8 + m_6 k_{11}}{\omega_{\text{b}}(1/L_{\text{t}} - m_4)} \qquad b_{\text{eq6}} = \frac{m_5 k_9 + m_6 k_{12}}{\omega_{\text{b}}(1/L_{\text{t}} - m_4)}$$

$$b_{\text{eq7}} = \frac{\omega_{\text{b}}/L_{\text{t}}}{\omega_{\text{b}}(1/L_{\text{t}} - m_4)} \qquad b_{\text{eq8}} = 0$$

C.4 Linearization of components in the synchronous machine's reference frame

C.4.1 Reference frame transformation

The expanded form of matrices in section 3.3.1 are given in this section.

$$A_\delta = 0 \qquad \boldsymbol{A_{\delta\text{gfm}}} = \begin{bmatrix} -\omega_{\text{b}} & \boldsymbol{0}_{1\times 16} \end{bmatrix} \qquad \boldsymbol{A_{\delta\text{sm}}} = \begin{bmatrix} \omega_{\text{b}} & \boldsymbol{0}_{1\times 15} \end{bmatrix}$$

C.4.2 Synchronous machine

The expanded form of matrices in section 3.3.2 are given with the intermediate steps of deriving them. The linearization of (3.3)-(3.9) can be firstly represented as (C.39).

$$\boldsymbol{\Delta\dot{X}_{\text{m}}} = \boldsymbol{A_{\text{md}}\Delta X_{\text{m}}} + \boldsymbol{B_{\text{md1}}}\begin{bmatrix}\Delta\psi_{\text{d}}\\ \Delta\psi_{\text{q}}\end{bmatrix} + \boldsymbol{B_{\text{md2}}}\begin{bmatrix}\Delta e_{\text{d}}\\ \Delta e_{\text{q}}\end{bmatrix} + \boldsymbol{B_{\text{md3}}}\begin{bmatrix}\Delta v_{\text{pid}}\\ \Delta v_{\text{piq}}\end{bmatrix} + \boldsymbol{B_{\text{md4}}}\Delta T_{\text{m}} + \boldsymbol{B_{\text{md5}}}\Delta E_{\text{fd}} \quad \text{(C.39)}$$

Here;

$$\boldsymbol{A_{md}} = \begin{bmatrix} \frac{-K_D}{2H} & \frac{\psi_{q0}}{2H} & 0 & 0 & \frac{-\psi_{d0}}{2H} & 0 & 0 \\ i_{q0}\omega_b & \frac{-\omega_b R_t}{L_t} & 0 & 0 & \omega_{sm0}\omega_b & 0 & 0 \\ 0 & k_3 & k_1 & k_2 & 0 & 0 & 0 \\ 0 & k_7 & k_5 & k_6 & 0 & 0 & 0 \\ -i_{d0}\omega_b & -\omega_{sm0}\omega_b & 0 & 0 & \frac{-\omega_b R_t}{L_t} & 0 & 0 \\ 0 & 0 & 0 & 0 & k_{10} & k_8 & k_9 \\ 0 & 0 & 0 & 0 & k_{13} & k_{11} & k_{12} \end{bmatrix}$$

$$\boldsymbol{B_{md1}} = \begin{bmatrix} \frac{-i_{q0}}{2H} & 0 & 0 & 0 & 0 & 0 & 0 \\ \frac{i_{d0}}{2H} & 0 & 0 & 0 & 0 & 0 & 0 \end{bmatrix}^T \quad \boldsymbol{B_{md2}} = \begin{bmatrix} 0 & \frac{\omega_b}{L_t} & 0 & 0 & 0 & 0 & 0 \\ 0 & 0 & 0 & 0 & \frac{\omega_b}{L_t} & 0 & 0 \end{bmatrix}^T$$

$$\boldsymbol{B_{md3}} = \begin{bmatrix} 0 & -\frac{\omega_b}{L_t} & 0 & 0 & 0 & 0 & 0 \\ 0 & 0 & 0 & 0 & -\frac{\omega_b}{L_t} & 0 & 0 \end{bmatrix}^T \quad \boldsymbol{B_{md4}} = \begin{bmatrix} \frac{1}{2H} & 0 & 0 & 0 & 0 & 0 & 0 \end{bmatrix}^T$$

$$\boldsymbol{B_{md5}} = \begin{bmatrix} 0 & 0 & k_4 & 0 & 0 & 0 & 0 \end{bmatrix}^T$$

By rearranging and linearizing (C.28)-(C.29), (C.40) can be obtained.

$$\begin{bmatrix} \Delta\psi_d \\ \Delta\psi_q \end{bmatrix} = \boldsymbol{M_{sidq}}\boldsymbol{\Delta X_m} \tag{C.40}$$

Here

$$\boldsymbol{M_{sidq}} = \begin{bmatrix} 0 & \frac{1}{m_1} & \frac{-m_2}{m_1} & \frac{-m_3}{m_1} & 0 & 0 & 0 \\ 0 & 0 & 0 & 0 & \frac{1}{m_4} & \frac{-m_5}{m_4} & \frac{-m_6}{m_4} \end{bmatrix}$$

By linearizing (C.37) and (C.38), (C.41) can be obtained.

$$\begin{bmatrix} \Delta e_d \\ \Delta e_q \end{bmatrix} = \boldsymbol{M_{e1}}\boldsymbol{\Delta X_m} + \boldsymbol{M_{e2}} \begin{bmatrix} \Delta v_{pid} \\ \Delta v_{piq} \end{bmatrix} + \boldsymbol{M_{e3}}\Delta E_{fd} \tag{C.41}$$

Here

$$\boldsymbol{M_{e1}} = \begin{bmatrix} \frac{b_{ed4}}{\omega_{sm}} i_{q0} + \frac{b_{ed5}}{\omega_{sm}} \psi_{1q0} + \frac{b_{ed6}}{\omega_{sm}} \psi_{2q0} & b_{ed1} & b_{ed2} & b_{ed3} & \frac{b_{ed4}}{\omega_{sm}} \omega_{sm0} & \frac{b_{ed5}}{\omega_{sm}} \omega_{sm0} & \frac{b_{ed6}}{\omega_{sm}} \omega_{sm0} \\ \frac{b_{eq1}}{\omega_{sm}} i_{d0} + \frac{b_{eq2}}{\omega_{sm}} \psi_{fd0} + \frac{b_{eq3}}{\omega_{sm}} \psi_{1d0} & \frac{b_{eq1}}{\omega_{sm}} \omega_{sm0} & \frac{b_{eq2}}{\omega_{sm}} \omega_{sm0} & \frac{b_{eq3}}{\omega_{sm}} \omega_{sm0} & b_{eq4} & b_{eq5} & b_{eq6} \end{bmatrix}$$

$$\boldsymbol{M_{e2}} = \begin{bmatrix} b_{ed7} & 0 \\ 0 & b_{eq7} \end{bmatrix} \qquad \boldsymbol{M_{e3}} = \begin{bmatrix} b_{ed8} \\ b_{eq8} \end{bmatrix}$$

By substituting (C.40) and (C.41) in (C.39), (3.10) can be obtained. The expended form of matrices in (3.10) are given below.

$$\boldsymbol{A_m} = \boldsymbol{A_{md}} + \boldsymbol{B_{md1}} \boldsymbol{M_{sidq}} + \boldsymbol{B_{md2}} \boldsymbol{M_{e1}} \quad \boldsymbol{A_{mGT}} = \boldsymbol{B_{md4}} \begin{bmatrix} 0 & 1 \end{bmatrix}$$

$$\boldsymbol{A_{mE}} = (\boldsymbol{B_{md2}} \boldsymbol{M_{e3}} + \boldsymbol{B_{md5}}) \begin{bmatrix} 0 & 0 & 1 \end{bmatrix} \quad \boldsymbol{A_{mN}} = (\boldsymbol{B_{md2}} \boldsymbol{M_{e2}} + \boldsymbol{B_{md3}}) \begin{bmatrix} 1 & 0 & 0 & 0 \\ 0 & 1 & 0 & 0 \end{bmatrix}$$

$$\boldsymbol{A_{mL}} = \boldsymbol{0}_{7\times4} \qquad \boldsymbol{B_m} = \boldsymbol{0}_{7\times2}$$

C.4.3 Governor and turbine

The expanded form of matrices in section 3.3.3 are given with the intermediate steps of deriving them. The linearization of (3.11)-(3.12) can be firstly represented as (C.42).

$$\boldsymbol{\Delta \dot{X}_{GT}} = \boldsymbol{A_{GTd}} \boldsymbol{\Delta X_{GT}} + \boldsymbol{B_{GTd1}} \Delta\omega_{sm} + \boldsymbol{B_{GTd2}} \Delta P_{smref} \tag{C.42}$$

Here;

$$\boldsymbol{A}_{\mathbf{GTd}} = \begin{bmatrix} -\frac{1}{T_{\mathrm{G}}} & 0 \\ \frac{1}{T_{\mathrm{CH}}} & -\frac{1}{T_{\mathrm{CH}}} \end{bmatrix} \qquad \boldsymbol{B}_{\mathbf{GTd1}} = \begin{bmatrix} -\frac{1}{T_{\mathrm{G}} D_{\mathrm{psm}}} \\ 0 \end{bmatrix} \qquad \boldsymbol{B}_{\mathbf{GTd2}} = \begin{bmatrix} \frac{1}{T_{\mathrm{G}}} \\ 0 \end{bmatrix}$$

(C.42) can be rearranged as shown in (3.13). The expanded form of matrices in (3.13) are given below.

$$\boldsymbol{A}_{\mathbf{GTm}} = \boldsymbol{B}_{\mathbf{GTd1}} \begin{bmatrix} 1 & 0 & 0 & 0 & 0 & 0 & 0 \end{bmatrix} \qquad \boldsymbol{A}_{\mathbf{GT}} = \boldsymbol{A}_{\mathbf{GTd}}$$

$$\boldsymbol{A}_{\mathbf{GTE}} = \boldsymbol{0}_{2\times 3} \qquad \boldsymbol{A}_{\mathbf{GTN}} = \boldsymbol{0}_{2\times 4}$$

$$\boldsymbol{A}_{\mathbf{GTL}} = \boldsymbol{0}_{2\times 4} \qquad \boldsymbol{B}_{\mathbf{GT}} = \boldsymbol{B}_{\mathbf{GTd2}} \begin{bmatrix} 1 & 0 \end{bmatrix}$$

C.4.4 Exciter

The expanded form of matrices in section 3.3.4 are given with the intermediate steps of deriving them. The linearization of (3.14)-(3.16) can be firstly represented as (C.43).

$$\boldsymbol{\Delta \dot{X}}_{\mathbf{E}} = \boldsymbol{A}_{\mathbf{Ed}} \boldsymbol{\Delta X}_{\mathbf{E}} + \boldsymbol{B}_{\mathbf{Ed1}} \boldsymbol{\Delta v}_{\mathbf{smref}} + \boldsymbol{B}_{\mathbf{Ed2}} \begin{bmatrix} \Delta e_{\mathrm{d}} \\ \Delta e_{\mathrm{q}} \end{bmatrix} \tag{C.43}$$

Here

$$\boldsymbol{A}_{\mathbf{Ed}} = \begin{bmatrix} -\frac{1}{T_{\mathrm{r}}} & 0 & 0 \\ -\frac{1}{T_{\mathrm{B}}} & -\frac{1}{T_{\mathrm{B}}} & 0 \\ -\frac{K_{\mathrm{A}} T_{\mathrm{C}}}{T_{\mathrm{A}} T_{\mathrm{B}}} & \frac{K_{\mathrm{A}}}{T_{\mathrm{A}}} \left(1 - \frac{T_{\mathrm{C}}}{T_{\mathrm{B}}}\right) & -\frac{1}{T_{\mathrm{A}}} \end{bmatrix} \qquad \boldsymbol{B}_{\mathbf{Ed1}} = \begin{bmatrix} 0 \\ \frac{1}{T_{\mathrm{B}}} \\ \frac{K_{\mathrm{A}} T_{\mathrm{C}}}{T_{\mathrm{A}} T_{\mathrm{B}}} \end{bmatrix}$$

$$\boldsymbol{B}_{\mathbf{Ed2}} = \begin{bmatrix} \frac{e_{\mathrm{d0}}}{T_{\mathrm{r}} \sqrt{e_{\mathrm{d0}}^2 + e_{\mathrm{q0}}^2}} & \frac{e_{\mathrm{q0}}}{T_{\mathrm{r}} \sqrt{e_{\mathrm{d0}}^2 + e_{\mathrm{q0}}^2}} \\ 0 & 0 \\ 0 & 0 \end{bmatrix}$$

(C.43) can be rearranged as shown in (3.17). The expanded form of matrices in (3.17) are given below.

$$\boldsymbol{A_{Em}} = \boldsymbol{B_{Ed2}} \boldsymbol{M_{e1}} \qquad \boldsymbol{A_{EGT}} = \boldsymbol{0}_{3\times 2}$$

$$\boldsymbol{A_{E}} = \boldsymbol{A_{Ed}} + \boldsymbol{B_{Ed2}} \boldsymbol{M_{e3}} \begin{bmatrix} 0 & 0 & 1 \end{bmatrix} \qquad \boldsymbol{A_{EN}} = \boldsymbol{B_{Ed2}} \boldsymbol{M_{e2}} \begin{bmatrix} 1 & 0 & 0 & 0 \\ 0 & 1 & 0 & 0 \end{bmatrix}$$

$$\boldsymbol{A_{EL}} = \boldsymbol{0}_{3\times 4} \qquad \boldsymbol{B_{E}} = \boldsymbol{B_{Ed1}} \begin{bmatrix} 0 & 1 \end{bmatrix}$$

C.4.5 Network

The expanded form of matrices in (3.19) are given in this section.

$$\boldsymbol{A_{Nm}} = \boldsymbol{B_{Nd1}} \begin{bmatrix} 1 & 0 & 0 & 0 & 0 & 0 & 0 \end{bmatrix} + \boldsymbol{B_{Nd2}} \begin{bmatrix} 0 & 1 & 0 & 0 & 0 & 0 & 0 \\ 0 & 0 & 0 & 0 & 1 & 0 & 0 \end{bmatrix}$$

$$\boldsymbol{A_{NGT}} = \boldsymbol{0}_{4\times 2} \qquad \boldsymbol{A_{NE}} = \boldsymbol{0}_{4\times 3}$$

C.4.6 Load

The expanded form of $\boldsymbol{A_{Loadsm}}$ in (3.21) is given here.

$$\boldsymbol{A_{Loadsm}} = \begin{bmatrix} \boldsymbol{0}_{4\times 7} & \boldsymbol{0}_{4\times 2} & \boldsymbol{0}_{4\times 3} & \boldsymbol{B_{Ld3}} \boldsymbol{B_{Ld5}} \begin{bmatrix} 0 & 0 & 1 & 0 \\ 0 & 0 & 0 & 1 \end{bmatrix} \end{bmatrix}$$

Appendix D

Appendix C includes the expanded form of the matrices relevant to the small-signal model of each sub-component in the GFM inverter with the virtual admittance-based inner current controller (section 4.2.1).

D.1 Power controller

The expanded form of matrices relevant to section 4.2.1 is mentioned in this section. $\boldsymbol{A_{PLCL}}$ in section B.2 will be modified as shown below.

$$\boldsymbol{A_{PCC}} = \boldsymbol{0}_{5\times 2} \qquad \boldsymbol{A_{PLCL}} = \begin{bmatrix} 0 & 0 & 0 & 0 & 0 & 0 \\ \frac{R_f i_{td0}}{T_p} & \frac{R_f i_{tq0}}{T_p} & \frac{i_{td0}}{T_p} & \frac{i_{tq0}}{T_p} & \frac{d}{T_p} & \frac{e}{T_p} \\ \frac{R_f i_{tq0}}{-T_q} & \frac{-R_f i_{td0}}{-T_q} & \frac{i_{tq0}}{-T_q} & \frac{-i_{td0}}{-T_q} & \frac{f}{-T_q} & \frac{g}{-T_q} \\ \frac{aR_f}{c} & \frac{bR_f}{c} & \frac{a}{c} & \frac{b}{c} & \frac{-aR_f}{c} & \frac{-bR_f}{c} \\ 0 & 0 & 0 & 0 & 0 & 0 \end{bmatrix}$$

D.2 Virtual Admittance Block

The expanded forms of matrices relevant to section 4.2.1 are mentioned in this section.

The linearizarion of (4.3)-(4.4) can be firstly represented as in (D.1).

$$\begin{bmatrix} \Delta {i_{\mathrm{cvd}}}^* \\ \Delta {i_{\mathrm{cvq}}}^* \end{bmatrix} = \begin{bmatrix} a_{\mathrm{vi}} & b_{\mathrm{vi}} \\ -b_{\mathrm{vi}} & a_{\mathrm{vi}} \end{bmatrix} \begin{bmatrix} \Delta v_{\mathrm{td}} \\ \Delta v_{\mathrm{tq}} \end{bmatrix} + \begin{bmatrix} -a_{\mathrm{vi}} & -b_{\mathrm{vi}} \\ b_{\mathrm{vi}} & -a_{\mathrm{vi}} \end{bmatrix} \begin{bmatrix} \Delta v_{\mathrm{pccd}} \\ \Delta v_{\mathrm{pccq}} \end{bmatrix} \tag{D.1}$$

Here

$$a_{\mathrm{vi}} = \frac{R_{\mathrm{virt}}}{{R_{\mathrm{virt}}}^2 + {X_{\mathrm{virt}}}^2} \qquad\qquad b_{\mathrm{vi}} = \frac{X_{\mathrm{virt}}}{{R_{\mathrm{virt}}}^2 + {X_{\mathrm{virt}}}^2}$$

For the convenience of representation, the output of the Q-v controller concerning the high voltage side of the connecting transformer is represented as in (D.2).

$$v_{\mathrm{td}} = ({v_{\mathrm{cvq}}}^*)\sin(-30^\circ) \qquad\qquad v_{\mathrm{tq}} = ({v_{\mathrm{cvq}}}^*)\cos(-30^\circ) \tag{D.2}$$

Linearizing (D.2) yields (D.3).

$$\begin{bmatrix} \Delta v_{\mathrm{td}} \\ \Delta v_{\mathrm{tq}} \end{bmatrix} = \begin{bmatrix} \sin(-30^\circ) \\ \cos(-30^\circ) \end{bmatrix} \boldsymbol{C_{\mathbf{E}}} \boldsymbol{\Delta X_{\mathbf{p}}} + \begin{bmatrix} \sin(-30^\circ) \\ \cos(-30^\circ) \end{bmatrix} \boldsymbol{D_{\mathbf{E}}} \boldsymbol{\Delta U} \mathbf{gfm} \tag{D.3}$$

The corresponding matrices for $\boldsymbol{C_{\mathbf{E}}}$ and $\boldsymbol{D_{\mathbf{E}}}$ are given in Appendix B.2. The d and q axis voltage components at the PCC (the terminal of the LC filter) are given by (D.4).

$$v_{\mathrm{pccd}} = v_{\mathrm{fd}} + (i_{\mathrm{cvd}} - i_{\mathrm{td}})R_{\mathrm{f}} \qquad\qquad v_{\mathrm{pccq}} = v_{\mathrm{fq}} + (i_{\mathrm{cvq}} - i_{\mathrm{tq}})R_{\mathrm{f}} \tag{D.4}$$

Linearizing (D.4) yields (D.5).

$$\begin{bmatrix} \Delta v_{\mathrm{pccd}} \\ \Delta v_{\mathrm{pccq}} \end{bmatrix} = \begin{bmatrix} R_{\mathrm{f}} & 0 & 1 & 0 & -R_{\mathrm{f}} & 0 \\ 0 & R_{\mathrm{f}} & 0 & 1 & 0 & -R_{\mathrm{f}} \end{bmatrix} \boldsymbol{\Delta X_{\mathbf{LCL}}} \tag{D.5}$$

By substituting (D.3) and (D.5) in (D.1), (4.5) can be obtained whose expanded forms

of the relevant matrices are given below.

$$\boldsymbol{A_{\mathbf{icvdqrefP}}} = \begin{bmatrix} a_{\mathrm{vi}} & b_{\mathrm{vi}} \\ -b_{\mathrm{vi}} & a_{\mathrm{vi}} \end{bmatrix} \begin{bmatrix} \sin(-30^{^\circ}) \\ \cos(-30^{^\circ}) \end{bmatrix} \boldsymbol{C_{\mathbf{E}}}$$

$$\boldsymbol{A_{\mathbf{icvdqrefLCL}}} = \begin{bmatrix} -a_{\mathrm{vi}} & -b_{\mathrm{vi}} \\ b_{\mathrm{vi}} & -a_{\mathrm{vi}} \end{bmatrix} \begin{bmatrix} R_{\mathrm{f}} & 0 & 1 & 0 & -R_{\mathrm{f}} & 0 \\ 0 & R_{\mathrm{f}} & 0 & 1 & 0 & -R_{\mathrm{f}} \end{bmatrix}$$

$$\boldsymbol{B_{\mathbf{icvdqref}}} = \begin{bmatrix} a_{\mathrm{vi}} & b_{\mathrm{vi}} \\ -b_{\mathrm{vi}} & a_{\mathrm{vi}} \end{bmatrix} \begin{bmatrix} \sin(-30^{^\circ}) \\ \cos(-30^{^\circ}) \end{bmatrix} \boldsymbol{D_{\mathbf{E}}}$$

D.3 Decoupled Current Controller

The expanded form of matrices relevant to section 4.2.1 is mentioned in this section.

$$\boldsymbol{A_{\mathbf{CCP}}} = \boldsymbol{A_{\mathbf{icvdqrefP}}} \qquad \boldsymbol{A_{\mathbf{CC}}} = \boldsymbol{0}_{2\times 2} \qquad \boldsymbol{A_{\mathbf{CCN}}} = \boldsymbol{A_{\mathbf{CCL}}} = \boldsymbol{0}_{2\times 4} \qquad \boldsymbol{B_{\mathbf{CC}}} = \boldsymbol{B_{\mathbf{icvdqref}}}$$

$$\boldsymbol{A_{\mathbf{CCLCL}}} = \boldsymbol{A_{\mathbf{icvdqrefLCL}}} + \begin{bmatrix} -1 & 0 & 0 & 0 & 0 & 0 \\ 0 & -1 & 0 & 0 & 0 & 0 \end{bmatrix}$$

D.4 LC filter and transformer

The expanded form of relevant matrices in section 4.2.1 are mentioned under this section. The output of the decoupled current controller can be represented by (D.6)-(D.7).

$$v_{\mathrm{cvd}} = K_{\mathrm{pi}}({i_{\mathrm{cvd}}}^{*} - i_{\mathrm{cvd}}) + (1/T_{\mathrm{ii}})x_4 + v_{\mathrm{pccd}} - \omega L_{\mathrm{f}} i_{\mathrm{cvq}} \tag{D.6}$$

$$v_{\mathrm{cvq}} = K_{\mathrm{pi}}({i_{\mathrm{cvq}}}^{*} - i_{\mathrm{cvq}}) + (1/T_{\mathrm{ii}})x_5 + v_{\mathrm{pccq}} + \omega L_{\mathrm{f}} i_{\mathrm{cvd}} \tag{D.7}$$

The linearizing of (D.6)-(D.7) results in (D.8).

$$\begin{bmatrix} \Delta \mathrm{v}_{\mathrm{cvd}} \\ \Delta \mathrm{v}_{\mathrm{cvq}} \end{bmatrix} = \boldsymbol{A}_{\mathbf{vcvdqP}} \boldsymbol{\Delta X}_{\mathbf{P}} + \boldsymbol{A}_{\mathbf{vcvdqCC}} \boldsymbol{\Delta X}_{\mathbf{CC}} + \boldsymbol{A}_{\mathbf{vcvdqLCL}} \boldsymbol{\Delta X}_{\mathbf{LCL}} + \boldsymbol{B}_{\mathbf{vcvdq}} \boldsymbol{\Delta U}_{\mathbf{gfm}} \tag{D.8}$$

Here

$$\boldsymbol{A}_{\mathbf{vcvdqP}} = K_{\mathrm{pi}} \boldsymbol{A}_{\mathbf{icvdqrefP}} + L_{\mathrm{f}} \begin{bmatrix} -i_{\mathrm{cvq0}} & i_{\mathrm{cvd0}} \end{bmatrix}^{\mathrm{T}} \begin{bmatrix} 1 & 0 & 0 & 0 & 0 \end{bmatrix}$$

$$\boldsymbol{A}_{\mathbf{vcvdqCC}} = \begin{bmatrix} 1/T_{\mathrm{ii}} & 0 \\ 0 & 1/T_{\mathrm{ii}} \end{bmatrix}$$

$$\boldsymbol{A}_{\mathbf{vcvdqLCL}} = K_{\mathrm{pi}} \boldsymbol{A}_{\mathbf{icvdqrefLCL}} + \begin{bmatrix} R_{\mathrm{f}} & 0 & 1 & 0 & -R_{\mathrm{f}} & 0 \\ 0 & R_{\mathrm{f}} & 0 & 1 & 0 & -R_{\mathrm{f}} \end{bmatrix} + \begin{bmatrix} -K_{\mathrm{pi}} & -\omega_{\mathrm{gfm0}} L_{\mathrm{f}} \\ \omega_{\mathrm{gfm0}} L_{\mathrm{f}} & -K_{\mathrm{pi}} \end{bmatrix} \begin{bmatrix} 1 & 0 & 0 & 0 & 0 & 0 \\ 0 & 1 & 0 & 0 & 0 & 0 \end{bmatrix}$$

$$\boldsymbol{B}_{\mathbf{vcvdq}} = K_{\mathrm{pi}} \boldsymbol{B}_{\mathbf{icvdqref}}$$

Due to the absence of high-frequency current components in the virtual admittance-based inner current controller, the state matrices (i.e., $\boldsymbol{A}_{\mathbf{LCLd}}$, $\boldsymbol{B}_{\mathbf{LCLd1}} - \boldsymbol{B}_{\mathbf{LCLd3}}$) in section B.3 will be modified by removing elements corresponding to $\Delta i_{\mathrm{cvdhp}}$ and $\Delta i_{\mathrm{cvqhp}}$. The expanded

form of matrices in (4.9) are given below.

$$\boldsymbol{A_{\mathbf{LCLP}}} = \boldsymbol{B_{\mathbf{LCLd1}}} \begin{bmatrix} 1 & 0 & 0 & 0 & 0 \end{bmatrix} + \boldsymbol{B_{\mathbf{LCLd2}}} \boldsymbol{A_{\mathbf{vcvdqP}}} \quad \boldsymbol{A_{\mathbf{LCLCC}}} = \boldsymbol{B_{\mathbf{LCLd2}}} \boldsymbol{A_{\mathbf{vcvdqCC}}}$$

$$\boldsymbol{A_{\mathbf{LCL}}} = \boldsymbol{A_{\mathbf{LCLd}}} + \boldsymbol{B_{\mathbf{LCLd2}}} \boldsymbol{A_{\mathbf{vcvdqLCL}}} \qquad \boldsymbol{A_{\mathbf{LCLL}}} = \boldsymbol{0}_{6\times 4}$$

$$\boldsymbol{A_{\mathbf{LCLN}}} = \boldsymbol{B_{\mathbf{LCLd3}}} \begin{bmatrix} 1 & 0 & 0 & 0 \\ 0 & 1 & 0 & 0 \end{bmatrix} \qquad \boldsymbol{B_{\mathbf{LCL}}} = \boldsymbol{B_{\mathbf{LCLd2}}} \boldsymbol{B_{\mathbf{vcvdq}}}$$

D.5 Network

The expanded form of matrices relevant to section 4.2.1 is mentioned in this section.

$$\boldsymbol{A_{\mathbf{NCC}}} = \boldsymbol{0}_{4\times 2} \qquad \boldsymbol{A_{\mathbf{NLCL}}} = \boldsymbol{B_{\mathbf{Nd2}}} \begin{bmatrix} 0 & 0 & 0 & 0 & 1 & 0 \\ 0 & 0 & 0 & 0 & 0 & 1 \end{bmatrix}$$

Appendix E

Appendix D includes the expanded form of the matrices relevant to the small-signal model of each sub-component in the GFM inverter with the cascaded voltage-current controller.

E.1 Decoupled Voltage controller

The expanded form of matrices in Section 4.2.2 is given in this section.

$$\boldsymbol{A_{\mathbf{VCP}}} = \begin{bmatrix} \sin(-30^{^\circ}) & \cos(-30^{^\circ}) \end{bmatrix}^{\mathrm{T}} \boldsymbol{C_{\mathbf{E}}} \qquad \boldsymbol{A_{\mathbf{VC}}} = \boldsymbol{A_{\mathbf{VCCC}}} = \boldsymbol{0}_{2\times 2}$$

$$\boldsymbol{A_{\mathbf{VCLCL}}} = \begin{bmatrix} 0 & 0 & -1 & 0 & 0 & 0 \\ 0 & 0 & 0 & -1 & 0 & 0 \end{bmatrix} \qquad \boldsymbol{A_{\mathbf{VCN}}} = \boldsymbol{A_{\mathbf{VCL}}} = \boldsymbol{0}_{2\times 4}$$

$$\boldsymbol{B_{\mathbf{VCC}}} = \begin{bmatrix} \sin(-30^{^\circ}) & \cos(-30^{^\circ}) \end{bmatrix}^{\mathrm{T}} \boldsymbol{D_{\mathbf{E}}}$$

E.2 Decoupled Current controller

The expanded form of matrices in Section 4.2.2 is given in this section.

$$\boldsymbol{A_{\mathbf{icvdqrefP}}} = K_{\mathrm{pv}} \begin{bmatrix} \sin(-30^{^\circ}) & \cos(-30^{^\circ}) \end{bmatrix}^{\mathrm{T}} \boldsymbol{C_{\mathbf{E}}} + C_{\mathrm{f}} \begin{bmatrix} -v_{\mathrm{fq0}} & v_{\mathrm{fd0}} \end{bmatrix}^{\mathrm{T}} \begin{bmatrix} 1 & 0 & 0 & 0 & 0 \end{bmatrix}$$

$$\boldsymbol{A}_{\mathbf{icvdqrefVC}} = \begin{bmatrix} 1/T_{\mathrm{iv}} & 0 \\ 0 & 1/T_{\mathrm{iv}} \end{bmatrix} \qquad \boldsymbol{A}_{\mathbf{icvdqrefLCL}} = \begin{bmatrix} 0 & 0 & -K_{\mathrm{pv}} & -\omega_0 C_{\mathrm{f}} & 1 & 0 \\ 0 & 0 & \omega_0 C_{\mathrm{f}} & -K_{\mathrm{pv}} & 0 & 1 \end{bmatrix}$$

$$\boldsymbol{B}_{\mathbf{icvdqref}} = K_{\mathrm{pv}} \begin{bmatrix} \sin(-30^{^\circ}) & \cos(-30^{^\circ}) \end{bmatrix}^{\mathrm{T}} \boldsymbol{D}_{\mathbf{E}}$$

$$\boldsymbol{A}_{\mathbf{CCP}} = \boldsymbol{A}_{\mathbf{icvdqrefP}} \qquad \boldsymbol{A}_{\mathbf{CCVC}} = \boldsymbol{A}_{\mathbf{icvdqrefVC}} \qquad \boldsymbol{A}_{\mathbf{CC}} = \boldsymbol{0}_{2\times 2}$$

$$\boldsymbol{A}_{\mathbf{CCLCL}} = \boldsymbol{A}_{\mathbf{icvdqrefLCL}} + \begin{bmatrix} -1 & 0 & 0 & 0 & 0 & 0 \\ 0 & -1 & 0 & 0 & 0 & 0 \end{bmatrix}$$

$$\boldsymbol{A}_{\mathbf{CCN}} = \boldsymbol{A}_{\mathbf{CCL}} = \boldsymbol{0}_{2\times 4} \qquad \boldsymbol{B}_{\mathbf{CC}} = \boldsymbol{B}_{\mathbf{icvdqref}}$$

E.3 *LC* filter and transformer

The expanded form of matrices in Section 4.2.2 is given in this section. The outputs of the decoupled current controller in (D.6)-(D.7) are a set of input for this component. The linearized representation of (D.6)-(D.7) in cascaded voltage-current controller embedded scenario is given in (E.1)

$$\begin{bmatrix} \Delta \mathrm{v}_{\mathrm{cvd}} \\ \Delta \mathrm{v}_{\mathrm{cvq}} \end{bmatrix} = \boldsymbol{A}_{\mathbf{vcvdqP}} \boldsymbol{\Delta X}_{\mathbf{P}} + \boldsymbol{A}_{\mathbf{vcvdqVC}} \boldsymbol{\Delta X}_{\mathbf{VC}} + \boldsymbol{A}_{\mathbf{vcvdqCC}} \boldsymbol{\Delta X}_{\mathbf{CC}} + \boldsymbol{A}_{\mathbf{vcvdqLCL}} \boldsymbol{\Delta X}_{\mathbf{LCL}} + \boldsymbol{B}_{\mathbf{vcvdq}} \boldsymbol{\Delta U}_{\mathbf{gfm}} \quad \text{(E.1)}$$

Here,

$$\boldsymbol{A}_{\mathbf{vcvdqP}} = K_{\mathrm{pi}} \boldsymbol{A}_{\mathbf{icvdqrefP}} + L_{\mathrm{f}} \begin{bmatrix} -i_{\mathrm{cvq0}} & i_{\mathrm{cvd0}} \end{bmatrix}^{\mathrm{T}} \begin{bmatrix} 1 & 0 & 0 & 0 & 0 \end{bmatrix}$$

$$\boldsymbol{A}_{\mathbf{vcvdqVC}} = K_{\mathrm{pi}} \boldsymbol{A}_{\mathbf{icvdqrefVC}}$$

$$\boldsymbol{A_{\mathbf{vcvdqCC}}} = \begin{bmatrix} 1/T_{\mathrm{ii}} & 0 \\ 0 & 1/T_{\mathrm{ii}} \end{bmatrix}$$

$$\boldsymbol{A_{\mathbf{vcvdqLCL}}} = K_{\mathrm{pi}}\boldsymbol{A_{\mathbf{icvdqrefLCL}}} + \begin{bmatrix} R_{\mathrm{f}} - K_{\mathrm{pi}} & -\omega_0 L_{\mathrm{f}} & 1 & 0 & -R_{\mathrm{f}} & 0 \\ \omega_0 L_{\mathrm{f}} & R_{\mathrm{f}} - K_{\mathrm{pi}} & 0 & 1 & 0 & -R_{\mathrm{f}} \end{bmatrix}$$

$$\boldsymbol{B_{\mathbf{vcvdq}}} = K_{\mathrm{pi}}\boldsymbol{B_{\mathbf{icvdqref}}}$$

Due to the absence of high-frequency current components in the virtual admittance-based inner current controller, the state matrices (i.e., $\boldsymbol{A_{\mathbf{LCLd}}}$, $\boldsymbol{B_{\mathbf{LCLd1}}} - \boldsymbol{B_{\mathbf{LCLd3}}}$) in section B.3 will be modified by removing elements corresponding to $\Delta i_{\mathrm{cvdhp}}$ and $\Delta i_{\mathrm{cvqhp}}$.The expanded forms of matrices in (4.23) are given below.

$$\boldsymbol{A_{\mathbf{LCLP}}} = \boldsymbol{B_{\mathbf{LCLd1}}} \begin{bmatrix} 1 & 0 & 0 & 0 & 0 \end{bmatrix} + \boldsymbol{B_{\mathbf{LCLd2}}}\boldsymbol{A_{\mathbf{vcvdqP}}}$$

$$\boldsymbol{A_{\mathbf{LCLVC}}} = \boldsymbol{B_{\mathbf{LCLd2}}}\boldsymbol{A_{\mathbf{vcvdqVC}}} \qquad \boldsymbol{A_{\mathbf{LCLCC}}} = \boldsymbol{B_{\mathbf{LCLd2}}}\boldsymbol{A_{\mathbf{vcvdqCC}}}$$

$$\boldsymbol{A_{\mathbf{LCL}}} = \boldsymbol{A_{\mathbf{LCLd}}} + \boldsymbol{B_{\mathbf{LCLd2}}}\boldsymbol{A_{\mathbf{vcvdqLCL}}} \qquad \boldsymbol{A_{\mathbf{LCLN}}} = \boldsymbol{B_{\mathbf{LCLd3}}} \begin{bmatrix} 1 & 0 & 0 & 0 \\ 0 & 1 & 0 & 0 \end{bmatrix}$$

$$\boldsymbol{A_{\mathbf{LCLL}}} = \boldsymbol{0}_{6\times 4} \qquad \boldsymbol{B_{\mathbf{LCL}}} = \boldsymbol{B_{\mathbf{LCLd2}}}\boldsymbol{B_{\mathbf{vcvdq}}}$$

E.4 Network

The expanded form of matrices relevant to section 4.2.2 is mentioned in this section.

$$\boldsymbol{A_{\mathbf{NVC}}} = \boldsymbol{A_{\mathbf{NCC}}} = \boldsymbol{0}_{4\times 2} \qquad \boldsymbol{A_{\mathbf{NLCL}}} = \boldsymbol{B_{\mathbf{Nd2}}} \begin{bmatrix} 0 & 0 & 0 & 0 & 1 & 0 \\ 0 & 0 & 0 & 0 & 0 & 1 \end{bmatrix}$$

Appendix F

The expanded forms of matrices relevant to Chapter 5 are given here.

F.1 DC-side Circuitry and Controller

The expanded forms of matrices in the section 5.2.1 are mentioned in this section along with the intermediate steps. The modulation index m is calculated from (F.1).

$$m = -K_{\mathrm{p}}(D_{\mathrm{q}}(Q_{\mathrm{ref}} - Q_{\mathrm{f}}) + E_{\mathrm{ref}} - E_{\mathrm{f}}) - x_1/T_{\mathrm{i}} \tag{F.1}$$

The linearized form of (F.1) is given by (F.2), whose expanded forms of matrices are given in Appendix B.2.

$$\Delta m = \boldsymbol{C_{\mathrm{E}}}\boldsymbol{\Delta X_{\mathrm{P}}} + \boldsymbol{D_{\mathrm{E}}}\boldsymbol{\Delta U_{\mathrm{gfm}}} \tag{F.2}$$

The linearization of (5.4) is given by (F.3).

$$\Delta i_{\mathrm{dc}} = \boldsymbol{A_{\mathrm{idcP}}}\boldsymbol{\Delta X_{\mathrm{P}}} + \boldsymbol{A_{\mathrm{idcLCL}}}\boldsymbol{\Delta X_{\mathrm{LCL}}} + \boldsymbol{B_{\mathrm{idc}}}\boldsymbol{\Delta U_{\mathrm{gfm}}} \tag{F.3}$$

Here;

$$\boldsymbol{A_{\mathrm{idcP}}} = (i_{\mathrm{cvd0}}\sin(-30^\circ) + i_{\mathrm{cvq0}}\cos(-30^\circ))\boldsymbol{C_{\mathrm{E}}}$$

$$\boldsymbol{A_{\mathrm{idcLCL}}} = \begin{bmatrix} m_0\sin(-30^\circ) & m_0\cos(-30^\circ) & 0 & 0 & 0 & 0 \end{bmatrix}$$

$$\boldsymbol{B_{idc}} = (i_{cvd0}\sin(-30^\circ) + i_{cvq0}\cos(-30^\circ))\boldsymbol{D_E}$$

Linearization of (5.12) is given by (F.4).

$$\Delta d = \boldsymbol{A_{dDC}}\boldsymbol{\Delta X_{DC}} + \boldsymbol{B_{dDC}}\boldsymbol{\Delta U_{DC}} \tag{F.4}$$

Here;

$$\boldsymbol{A_{dDC}} = \begin{bmatrix} 0 & 0 & -K_{pibat}K_{pvdc} & K_{pibat} & -K_{pibat} & K_{pibat}/T_{ivdc} & 1/T_{iibat} \end{bmatrix}$$

$$\boldsymbol{B_{dDC}} = \begin{bmatrix} K_{pibat}K_{pvdc} \end{bmatrix}$$

The expanded forms of matrices in (5.13) are given below.

$$\boldsymbol{A_{DC}} = \begin{bmatrix} -(\omega_b(1-d_0)/L_{bat})\begin{bmatrix} 0 & 1 & 0 & 0 & 0 & 0 & 0 \end{bmatrix} + (\omega_b v_{dc0}/L_{bat})\boldsymbol{A_{dDC}} \\ (\omega_b(1-d_0)/C_{dc})\begin{bmatrix} 1 & 0 & 0 & 0 & 0 & 0 & 0 \end{bmatrix} - (\omega_b i_{bat0}/C_{dc})\boldsymbol{A_{dDC}} \\ \begin{bmatrix} 0 & 1/T_{vdc} & -1/T_{vdc} & 0 & 0 & 0 & 0 \end{bmatrix} \\ \begin{bmatrix} 0 & 0 & 0 & -1/T_{idc} & 0 & 0 & 0 \end{bmatrix} \\ \begin{bmatrix} 1/T_{ibat} & 0 & 0 & 0 & -1/T_{ibat} & 0 & 0 \end{bmatrix} \\ \begin{bmatrix} 0 & 0 & -1 & 0 & 0 & 0 & 0 \end{bmatrix} \\ \begin{bmatrix} 0 & 0 & -K_{pvdc} & 1 & -1 & 1/T_{ivdc} & 0 \end{bmatrix} \end{bmatrix}$$

$$\boldsymbol{A_{DCP}} = \begin{bmatrix} \boldsymbol{0}_{1\times5} & (-\omega_b/C_{dc})\boldsymbol{A_{idcP}} & \boldsymbol{0}_{1\times5} & \boldsymbol{A_{idcP}}/T_{idc} & \boldsymbol{0}_{1\times5} & \boldsymbol{0}_{1\times5} & \boldsymbol{0}_{1\times5} \end{bmatrix}^T$$

$$\boldsymbol{A_{DCLCL}} = \begin{bmatrix} \boldsymbol{0}_{1\times6} & (-\omega_b/C_{dc})\boldsymbol{A_{idcLCL}} & \boldsymbol{0}_{1\times6} & \boldsymbol{A_{idcLCL}}/T_{idc} & \boldsymbol{0}_{1\times6} & \boldsymbol{0}_{1\times6} & \boldsymbol{0}_{1\times6} \end{bmatrix}^T$$

$$\boldsymbol{A_{DCCC}} = \boldsymbol{0}_{7\times2}$$

$$\boldsymbol{A_{DCN}} = \boldsymbol{A_{DCL}} = \boldsymbol{0}_{7\times4}$$

$$\boldsymbol{B}_{\mathbf{DCgfm}} = \begin{bmatrix} \boldsymbol{0}_{1\times4} & (-\omega_{\mathrm{b}}/C_{\mathrm{dc}})\boldsymbol{B}_{\mathbf{idc}} & \boldsymbol{0}_{1\times4} & \boldsymbol{B}_{\mathbf{idc}}/T_{\mathrm{idc}} & \boldsymbol{0}_{1\times4} & \boldsymbol{0}_{1\times4} & \boldsymbol{0}_{1\times4} \end{bmatrix}^{\mathrm{T}}$$

$$\boldsymbol{B}_{\mathbf{DC}} = \begin{bmatrix} (\omega_{\mathrm{b}} v_{\mathrm{dc0}}/L_{\mathrm{bat}})\boldsymbol{B}_{\mathbf{dDC}} & (-\omega_{\mathrm{b}} i_{\mathrm{bat0}}/C_{\mathrm{dc}})\boldsymbol{B}_{\mathbf{dDC}} & 0 & 0 & 0 & 1 & K_{\mathrm{pvdc}} \end{bmatrix}^{\mathrm{T}}$$

F.2 Virtual Admittance Block

The expanded form of $\boldsymbol{A}_{\mathbf{icvdqrefDC}}$ in (5.15) is given in this section. m is given in (F.1).

$$\boldsymbol{A}_{\mathbf{icvdqrefDC}} = m_0 \begin{bmatrix} a_{\mathrm{vi}} & b_{\mathrm{vi}} \\ -b_{\mathrm{vi}} & a_{\mathrm{vi}} \end{bmatrix} \begin{bmatrix} \sin(-30^\circ) \\ \cos(-30^\circ) \end{bmatrix} \begin{bmatrix} 0 & 1 & 0 & 0 & 0 & 0 & 0 \end{bmatrix}$$

F.3 LC filter and transformer

The expanded forms of $\boldsymbol{A}_{\mathbf{LCLDC}}$ and $\boldsymbol{B}_{\mathbf{LCLDC}}$ in section 5.2.5 are given in this section.

$$\boldsymbol{A}_{\mathbf{LCLDC}} = \boldsymbol{A}_{\mathbf{LCL}} + \boldsymbol{B}_{\mathbf{LCLd2}}\boldsymbol{A}_{\mathbf{vcvdqDC}} \qquad \boldsymbol{B}_{\mathbf{LCLDC}} = \boldsymbol{0}_{6\times1}$$

Bibliography

[1] Energy Development and Power Generation Committee, Electric Machinery Committee, and Power System Relaying and Control Committee, *IEEE Standard for Interconnection and Interoperability of Inverter-Based Resources (IBRs) Interconnecting with Associated Transmission Electric Power Systems*. Institute of Electrical and Electronics Engineers, New York, USA, 2022.

[2] D. B. Rathnayake, M. Akrami, C. Phurailatpam, S. P. Me, S. Hadavi, G. Jayasinghe, S. Zabihi, and B. Bahrani, "Grid forming inverter modeling, control, and applications," *IEEE Access*, vol. 9, pp. 114781–114807, August 2021.

[3] R. Rosso, X. Wang, M. Liserre, X. Lu, and S. Engelken, "Grid-forming converters: Control approaches, grid-synchronization, and future trends—a review," *IEEE Open J. Industry Appl.*, vol. 2, pp. 93–109, April 2021.

[4] P. Unruh, M. Nuschke, P. Strauß, and F. Welck, "Overview on grid-forming inverter control methods," *Energies*, vol. 13, no. 10, p. 2589, May 2020.

[5] J. Rocabert, A. Luna, F. Blaabjerg, and P. Rodríguez, "Control of power converters in ac microgrids," *IEEE Trans. Power Electron.*, vol. 27, no. 11, pp. 4734–4749, Nov. 2012.

[6] J. Guerrero, L. de Vicuna, J. Matas, M. Castilla, and J. Miret, "A wireless controller to enhance dynamic performance of parallel inverters in distributed generation systems," *IEEE Trans. Power Electron.*, vol. 19, no. 5, pp. 1205–1213, Sept. 2004.

[7] B. B. Johnson, S. V. Dhople, A. O. Hamadeh, and P. T. Krein, "Synchronization of parallel single-phase inverters with virtual oscillator control," *IEEE Trans. Power Electron.*, vol. 29, no. 11, pp. 6124–6138, Nov. 2014.

[8] M. van Wesenbeeck, S. de Haan, P. Varela, and K. Visscher, "Grid tied converter with virtual kinetic storage," in *2009 IEEE Bucharest PowerTech*, pp. 1–7, Jun. 28 - Jul. 02 2009.

[9] C. Arghir and F. Dörfler, "The electronic realization of synchronous machines: Model matching, angle tracking, and energy shaping techniques," *IEEE Trans. Power Electron.*, vol. 35, no. 4, pp. 4398–4410, April 2020.

[10] S. D'Arco, J. A. Suul, and O. B. Fosso, "A virtual synchronous machine implementation for distributed control of power converters in smartgrids," *Electric Power Syst. Res.*, vol. 122, pp. 180–197, May 2015.

[11] Z. Shuai, W. Huang, Z. J. Shen, A. Luo, and Z. Tian, "Active power oscillation and suppression techniques between two parallel synchronverters during load fluctuations," *IEEE Trans. Power Electron.*, vol. 35, no. 4, pp. 4127–4142, April 2020.

[12] J. Liu, Y. Miura, H. Bevrani, and T. Ise, "Enhanced virtual synchronous generator control for parallel inverters in microgrids," *IEEE Trans. Smart Grid*, vol. 8, no. 5, pp. 2268–2277, Sept. 2017.

[13] R. Rosso, S. Engelken, and M. Liserre, "Analysis of the behavior of synchronverters operating in parallel by means of component connection method (CCM)," in *2018 IEEE Energy Convers. Congr. Expo. (ECCE)*, (Portland, OR, USA), pp. 2228–2235, Sept. 2018.

[14] R. Rosso, S. Engelken, and M. Liserre, "Robust stability analysis of synchronverters operating in parallel," *IEEE Trans. Power Electron.*, vol. 34, no. 11, pp. 11309–11319, Nov. 2019.

[15] K. Vatta Kkuni, S. Mohan, G. Yang, and W. Xu, "Comparative assessment of typical control realizations of grid forming converters based on their voltage source behaviour," *Energy Rep.*, vol. 9, pp. 6042–6062, Dec. 2023.

[16] N. Pogaku, M. Prodanovic, and T. C. Green, "Modeling, analysis and testing of autonomous operation of an inverter-based microgrid," *IEEE Trans. Power Electron.*, vol. 22, no. 2, pp. 613–625, March 2007.

[17] X. Wang, F. Blaabjerg, and W. Wu, "Modeling and analysis of harmonic stability in an ac power-electronics-based power system," *IEEE Trans. Power Electron.*, vol. 29, no. 12, pp. 6421–6432, Dec.2014.

[18] X. Wang and F. Blaabjerg, "Harmonic stability in power electronic-based power systems: Concept, modeling, and analysis," *IEEE Trans. Smart Grid*, vol. 10, no. 3, pp. 2858–2870, May 2019.

[19] P. Kundur, *Power system Stability and Control*. New York NY: McGraw-Hill, Inc., 1 ed., 1994.

[20] Y. Wang, X. Wang, Z. Chen, and F. Blaabjerg, "Small-Signal Stability Analysis of Inverter-Fed Power Systems Using Component Connection Method," *IEEE Trans. Smart Grid*, vol. 9, no. 5, pp. 5301–5310, Sep. 2018.

[21] H. Wu, X. Ruan, D. Yang, X. Chen, W. Zhao, Z. Lv, and Q.-C. Zhong, "Small-Signal Modeling and Parameters Design for Virtual Synchronous Generators," *IEEE Trans. Ind. Electron.*, vol. 63, no. 7, pp. 4292–4303, July 2016.

[22] A. D. Paquette and D. M. Divan, "Virtual impedance current limiting for inverters in microgrids with synchronous generators," *IEEE Trans. Industry Appl.*, vol. 51, no. 2, pp. 1630–1638, April 2015.

[23] T. Thilekha, S. Filizadeh, U. Annakkage, C. Karawita, and D. Muthumuni, "Analysis of interactions among parallel grid-forming inverters," *Electric Power Syst. Res.*, vol. 223, p. 109652, Oct. 2023.

[24] B. Fan, T. Liu, F. Zhao, H. Wu, and X. Wang, "A review of current-limiting control of grid-forming inverters under symmetrical disturbances," *IEEE Open J. Power Electron.*, vol. 3, pp. 955–969, Dec. 2022.

[25] M. Moon and R. Johnson, "DSP control of ups inverter with over-current limit using droop method," in *30th Annu. IEEE Power Electron. Specialists Conf. Rec.*, vol. 1, pp. 552–557 vol.1, July 1999.

[26] T. Liu, X. Wang, F. Liu, K. Xin, and Y. Liu, "A current limiting method for single-loop voltage-magnitude controlled grid-forming converters during symmetrical faults," *IEEE Trans. Power Electron.*, vol. 37, no. 4, pp. 4751–4763, April 2022.

[27] J. He and Y. W. Li, "Analysis, design, and implementation of virtual impedance for power electronics interfaced distributed generation," *IEEE Trans. Industry Appl.*, vol. 47, no. 6, pp. 2525–2538, Nov.-Dec. 2011.

[28] M. A. Zamani, A. Yazdani, and T. S. Sidhu, "A control strategy for enhanced operation of inverter-based microgrids under transient disturbances and network faults," *IEEE Trans. Power Del.*, vol. 27, no. 4, pp. 1737–1747, Oct. 2012.

[29] L. Huang, H. Xin, Z. Wang, L. Zhang, K. Wu, and J. Hu, "Transient stability analysis and control design of droop-controlled voltage source converters considering current limitation," *IEEE Trans. Smart Grid*, vol. 10, no. 1, pp. 578–591, Jan. 2019.

[30] I. Sadeghkhani, M. E. Hamedani Golshan, J. M. Guerrero, and A. Mehrizi-Sani, "A current limiting strategy to improve fault ride-through of inverter interfaced autonomous microgrids," *IEEE Trans. Smart Grid*, vol. 8, no. 5, pp. 2138–2148, Sept. 2017.

[31] N. Baeckeland, D. Venkatramanan, M. Kleemann, and S. Dhople, "Stationary-frame grid-forming inverter control architectures for unbalanced fault-current limiting," *IEEE Trans. Energy Convers.*, vol. 37, no. 4, pp. 2813–2825, Dec. 2022.

[32] B. Mahamedi, M. Eskandari, J. E. Fletcher, and J. Zhu, "Sequence-based control strategy with current limiting for the fault ride-through of inverter-interfaced distributed generators," *IEEE Trans. Sustain. Energy*, vol. 11, no. 1, pp. 165–174, Jan. 2020.

[33] T. Thilekha, S. Filizadeh, U. Annakkage, D. Muthumuni, and C. Karawita, "Parallel operation of grid-forming inverters with synchronous machines," in *2022 CIGRE Canada Conf. Expo*, (Calgary, Canada), Oct 2022.

[34] P. J. d. S. Neto, T. A. d. S. Barros, J. P. C. Silveira, E. R. Filho, J. C. Vasquez, and J. M. Guerrero, "Power management strategy based on virtual inertia for dc microgrids," *IEEE Trans. Power Electron.*, vol. 35, no. 11, pp. 12472–12485, Nov. 2020.

[35] W. Wu, Y. Chen, A. Luo, L. Zhou, X. Zhou, L. Yang, Y. Dong, and J. M. Guerrero, "A virtual inertia control strategy for dc microgrids analogized with virtual synchronous machines," *IEEE Trans. Ind. Electron.*, vol. 64, no. 7, pp. 6005–6016, July 2017.

[36] K. Shi, H. Ye, W. Song, and G. Zhou, "Virtual inertia control strategy in microgrid based on virtual synchronous generator technology," *IEEE Access*, vol. 6, pp. 27949–27957, May 2018.

[37] D. Chen, Y. Xu, and A. Q. Huang, "Integration of dc microgrids as virtual synchronous machines into the ac grid," *IEEE Trans. Ind. Electron.*, vol. 64, no. 9, pp. 7455–7466, Sept. 2017.

[38] O. A.-L. S. L. G. O. Kalcon, G. P. Adam and K. Uhlen, "Small-signal stability analysis of multi-terminal VSC-based dc transmission systems," *IEEE Trans. Power Syst.*, vol. 27, no. 4, pp. 1818–1830, Nov. 2012.

[39] A. A. A. Radwan and Y. A.-R. I. Mohamed, "Analysis and active suppression of ac- and dc-side instabilities in grid-connected current-source converter-based photovoltaic system," *IEEE Trans Sustain. Energy*, vol. 4, no. 3, pp. 630–642, July 2013.

[40] J. H. Y. Huang, X. Yuan and P. Zhou, "Modeling of vsc connected to weak grid for stability analysis of dc-link voltage control," *IEEE J. Emerg. Sel. Topics in Power Electron.*, vol. 3, no. 4, pp. 1193–1204, Dec. 2015.